STRUCTURAL RELAXATION OF SUPERCOOLED LIQUIDS BASED ON SOFT PARTICLES: AVOIDING THE GLASS TRANSITION AT HIGH CONCENTRATIONS

A Thesis
Presented to
The Academic Faculty

by

John Shelton Hyatt

In Partial Fulfillment
of the Requirements for the Degree
Doctor of Philosophy in the
School of Physics

Georgia Institute of Technology
August 2016

STRUCTURAL RELAXATION OF SUPERCOOLED LIQUIDS BASED ON SOFT PARTICLES: AVOIDING THE GLASS TRANSITION AT HIGH CONCENTRATIONS

Approved by:

Professor Alberto Fernández-Nieves,
Advisor
School of Physics
Georgia Institute of Technology

Professor Phillip N. First
School of Physics
Georgia Institute of Technology

Professor Peter Yunker
School of Physics
Georgia Institute of Technology

Professor Harold Kim
School of Physics
Georgia Institute of Technology

Professor Alexander Alexeev
School of Mechanical Engineering
Georgia Institute of Technology

Date Approved: July 11 2016

To everyone who has been there for me throughout the past eight years...

thank you from the bottom of my heart.

To everyone working on their own degree...keep at it, guys!

And to my grandfather, Dr. Russell D. Shelton, the rocket scientist.

ACKNOWLEDGEMENTS

Like any big project, this thesis wouldn't exist without the contributions of many people.

Alberto, my advisor, and the other members of my committee: Drs. Peter Yunker, Alexander Alexeev, Phillip First, and Harold Kim.

J.J., my mentor, who took me under his wing when I joined the lab.

Jonas, my excellent apprentice. May the student surpass the teacher.

My officemates, Alex and Perry, and the rest of the group: Mikes T. and D., Josefa, Ekapop, Winnie, and everyone else. You guys have been more than just coworkers—you've been good friends when I needed as many as I could get. It's been a pleasure.

Alison Douglas, another good friend and longtime collaborator who got her doctorate a little before me. Chapter IV wouldn't have been possible without her.

Drs. L. Andrew Lyon and Xiaobo Hu for synthesizing my microgels.

Oak Ridge National Laboratory and Drs. Changwoo Do and Chris Stanley, who made the neutron scattering portions of this work possible.

Drs. Andrew Zangwill, Paul Goldbart, and Pablo Laguna of the School of Physics, for helping me over a few rough patches, and the staff of the School of Physics—in particular Kevin Carter and Vicki Speights, who have been very, very helpful over the years.

Financial support from the Georgia Tech School of Physics and IBB seed grant program, a GAANN Award from the U.S. Department of Education, and NSF grant DMR-1609841.

My family, and especially my mom, for being so supportive.

My friends, for helping keep me sane. Wallace Chan, who is working on his own doctorate—add oil, bro! Lauren, Yug, and the rest of the crew. And especially Alissa, who understood a lot, forgave more, and was always there.

Finally, I would like to extend a special thanks to two people who will never read these words. First, Dr. Dennis Schneider, whose calculus course changed my life forever. And, second, Vanthus Vanderboren, who did it the hard way.

TABLE OF CONTENTS

LIST OF TABLES

LIST OF FIGURES

CHAPTER I

INTRODUCTION

Humans and glasses go back a long way. During the Stone Age, prehistoric humans in every part of the world knapped volcanic obsidian glass into tools and weapons or polished it into the earliest mirrors. Man-made silica glass was developed shortly after the beginning of the Bronze Age, possibly as an accidental by-product of early metalworking [1].

In the thousands of years since, glasses have become increasingly ubiquitous. The compound microscope and the refracting telescope have both made enormous contributions to scientific advancement, and both were made possible by glass lenses. Glass windows and the enormous glass curtain walls found on skyscrapers are integral parts of modern architecture, and windshields and display screens are ubiquitous in our daily lives. Rewritable CDs and DVD technology relies on the chalcogenide glass transition [2], metallic glasses are often tougher and more resistant to wear than naturally-occuring, crystalline metals [3, 4], and obsidian glass scalpels, which can be sharpened to an atomically fine edge, are sometimes preferred by surgeons to their metal counterparts [5].

We still lack a fundamental understanding of the physics behind the glass transition, despite thousands of years of practical experience. This is in large part because glass transition is a non-equilibrium phenomenon, and therefore, unlike the related freezing/melting transition, is not a true phase transition and does not depend solely on the state of the system. Rather, the exact properties of a glass depend on the system's history and the constituents of a glass continuously relax to different, lower-energy states in a process known as "aging."

Additionally, there are many types of glass, all of which are characterized by some type of structural disorder together with long-term dynamic stability. In the familiar example of atomic or molecular glasses, the structural disorder occurs in the positions of the molecules, which are random, as in a liquid. However, these random positions are dynamically stable

and do not change in time, as in a crystalline solid. Such glasses are formed when a liquid is supercooled, or cooled below the equilibrium freezing point. In this regime, atomic diffusion slows enormously, viscosity increases by many orders of magnitude, and relaxation times seemingly diverge—all while bypassing the liquid's tendency to crystallize. This is most commonly accomplished by a rapid enough temperature quench [6] or pressure increase [7] that crystallization cannot happen. Alternatively, the disorder can be built in by way of polydispersity—including atoms or molecules of very different sizes—and frustrating the system's attempt to achieve crystalline order [8].

Glasses can also be realized in systems where the sizes of the individual components are on the order of a $10^{-9} - 10^{-6}$ m. These colloidal glasses resemble molecular systems in many ways, but instead of T, the relevant thermodynamic variable controlling the state is volume fraction [9, 10]. Glasses can also be formed from polymer chains [11]. Finally, there exist more exotic glasses such as spin glasses, in which the spatial position of the atoms is crystalline, but their magnetic dipole moment is randomly oriented [12, 13].

Since the properties of a glass are dependent on the history of the system, systems far from equilibrium require absurdly long preparation times, many orders of magnitude too long to be practical for an experimentalist. Recorded history, after all, is less than 6,000 years old —and the modern scientific method is younger still. Glasses may have to navigate their energy landscape for millions of years to reach these states of interest. This limitation has been successfully circumvented in some cases, either by experimenting on naturally-occurring glasses formed millions of years ago [14–16], or by manufacturing glasses via physical vapor deposition that are identical to glasses with very long aging histories [17]. Various competing theories have been developed to explain glass formation, of which mode coupling theory [18, 19] and random first-order transition theory [20, 21] are probably the most popular. However, to date no theory has succeeded in capturing the full range of experimental results. In addition, most glass transition theories are complicated and abstract, making it very diffitult to extract physical meaning from the models even when they do match some of the available experimental observations. Recent research has also suggested a distinction between the glass transition observed in thermal systems and

the jamming transition characteristic of athermal systems, such as sand, marbles, or non-Brownian foams or emulsions [22–24]. A consesus has yet to emerge in the soft matter community about the best way to integrate jamming into glass theory.

Even though the archetypical "glass" systems are atomic, colloidal glassformers have been key to experimental efforts aimed at understanding the glass transition [9, 10, 25–38]. Because atomic systems are so small, they are difficult to image directly and their dynamics can be too fast to resolve. In contrast, colloids have characteristic length and timescales larger by many orders of magnitude than atoms, yet the glassforming behavior of both seems to be governed by the same physics [39–43]. Further, their detailed interactions and material properties can be varied more readily than atomic or molecular systems—for example by varying the particle polydispersity [44], particle stiffness [45], or the internal structure of the particle [46].

Microgels—defined as a crosslinked polymer network, in the colloidal domain, swollen by a solvent—exemplify this versatility. They are compressible and soft, and with the appropriate chemistry can also change their structure and interactions based on temperature [47], pressure [48], charge [49], or salt concentration [50], to name a few possibilities. The details of particle "softness" are determined by the specifics of the synthesis as well. These properties, particularly the broad concept of "softness" are not found in atomic glassforming systems. Colloidal glasses are more than just models for atomic systems—they display their own unique physics.

We study the glass transition in a colloidal microgel system in order to take advantage of some of these unique properties. Specifically, we use *N*-isopropylacrylamide-*co*-poly(ethylene glycol diacrylate)-*co*-acrylic acid (NIPAM/pEG-d/AAc) microgels suspended in water, which were synthesized for us by Dr. Xiaobo Hu from the Lyon group in Georgia Tech's School of Chemistry and Biochemistry. p(NIPAM) has a lower critical solution temperature (LCST) at around 32-34 °C in H_2O; below this temperature it is hydrophilic, while it is hydrophobic at higher temperatures. Generally, a pNIPAM polymer decreases slightly in size as the temperature increases, until the LCST is reached. Above the LCST, the polymer abruptly deswells to its minimum size. The contribution of AAc to the swelling

behavior, meanwhile, is governed by the pH of the suspension. AAc has a pK_a of about 4.4 and ionizes at higher pH, drawing in counterions from the solvent. Thus, these microgels swell at low temperatures and high pH, and deswell at high temperatures and low pH.

We distinguish between the liquid, supercooled liquid, and glassy states of soft NIPAM-pEG-AAc microgels at different degrees of swelling and packing fractions. We identify a regime in which the microgels deswell as their number density is increased, trapping the system just below the onset of rigidity in the glass state. This study combines light scattering and rheological measurements of relaxation times, length scales, and shear moduli. Our understanding of the dense suspensions of interest is informed by light scattering and small-angle neutron scattering (SANS) experiments conducted on dilute systems, where single-particle characteristics can be quantified. The Thesis is arranged as follows:

In Chapter II, we describe the chemistry and synthesis of the microgel system we use and perform the initial characterization at dilute conditions. This Chapter includes a theoretical introduction to 3D dynamic light scattering (3DDLS) and static light scattering (SLS), including a discussion of the hydrodynamic radius and discussions of the form and structure factors. We also describe various experimental considerations and corrections to the raw data. Finally, we discuss the relationship between concentration and generalized volume fraction, ζ, used to describe concentrated suspensions.

In Chapter III, we discuss the single-particle structure of the microgels at low pH, when the AAc monomers are uncharged. In these conditions, we observe an unexpected frustration of the pNIPAM coil-to-globule transition at high temperatures typified by the segregation of mass to the periphery of the particles, as seen in light scattering measurements. This coincides with a markedly increasing length scale associated with heterogeneous polymer distribution, seen as a qualitative shift in the form factor observed with SANS. We interpret these results by noting that (i) the high amount of AAc included in our synthesis breaks up NIPAM chains into segments so short that pNIPAM's characteristic coil-to-globule collapse, which is a cooperative effect requiring a minimum number of monomers per chain, cannot occur, and that (ii) the pEG-d crosslinker is not distributed homogeneously in our microgels; more crosslinker at the core of the particle means that pNIPAM sequences there

are likely to be shorter and therefore less likely to collapse.

In Chapter IV, we explore a qualitatively different mass segregation, this time to the center of the particles, when the AAc is partially (but not completely) ionized. Here the form factor obtained from SANS also undergoes marked changes, indicating a sharply decreasing polymer length scale. Following a theory developed for macrogels, we identify this with the clustering of like charges. The resulting energetic penalty is offset by a corresponding gain of entropy by the counterions in solution. Supporting this argument are SANS measurements on a similar microgel system that we fit according to this theory.

In Chapter V, we move on to the concentrated systems of interest. First, concentrated SLS measurements allow us to obtain the measurable structure factor, $S_{\mathrm{M}}(q)$, for our system at different conditions and ζ. As we discuss in the Chapter, this is a simplification of the true structure factor, which is a tensor for polydisperse systems, into scalar form. We include a discussion of changes in the form factor, $P(q)$, at high ζ, estimated following contrast-matching SANS experiments on similar systems, and correct for this effect in our measurements. Our DLS measurements are made at the first peak of the structure factor, where the relaxation time corresponds to the particles' configurational rearrangements. Differences in the observed correlation functions allow us to separate the liquid and supercooled liquid regimes. In order to extend these measurements to even higher ζ, we turn to oscillatory and steady-state rheology. Our measurements provide a complete picture of the relaxation times of these dense systems over a wide range of ζ, clearly showing that the relaxation time increase is more complex than a simple divergence at finite ζ. We do see an "apparent divergence" that is well-fitted by the empirical Vogel-Fulcher-Tamman equation [51–53] at lower ζ. However, above the glass transition ζ predicted by the VFT fit, we observe a new regime in which relaxation times level off and do not change significantly with increasing ζ, indicating that the system is trapped in a pre-glass state. Flow curves for the system in these conditions are well-described by a model for a pre-glass system in which jamming plays no role [23, 24]. At the same time, while zero-shear viscosity does continue to increase, so does the high-ω elastic modulus of the suspension, causing the relaxation times to increase only slightly.

Physically, this stems from the disconnect between ζ, which is always proportional to concentration, and the real volume fraction ϕ, at high concentrations. Because the particles are compressible, they can deswell when crowded together; because they are deformable, they can fill the spaces that would be left between spherical particles in contact. Further, because the particles are charged, the ionic osmotic pressure that free ions in solution exert on the microgels [54] can lead to deswelling even when the particles are not in contact [55]. This deswelling on the approach to the glass transition is likely responsible for the non-divergence of relaxation times we observe experimentally.

Finally, in Chapter VI, we conclude by summarizing our results and contextualizing this work within the broader narratives of dense microgel systems and colloidal glass and jamming physics.

CHAPTER II

OUR MICROGELS: SYNTHESIS AND INITIAL CHARACTERIZATION

2.1 Introduction

In order to properly understand our observations of microgels in the glassy state, we need to have a clear picture of their physical characteristics. In high concentrations, soft particles tend to deform and compress due to the close presence of their neighbors, and may interpenetrate with their neighbors to a certain extent depending on the details of their internal structure. Such effects have a profound influence on glassy behavior and must be carefully accounted for. The detailed single-particle structure will also play an important role; if polymer and crosslink density are inhomogeneously distributed inside the microgels, the elastic modulus of the polymer network will not be uniform throughout the particle, again affecting the resulting behavior. In this Chapter, we characterize our NIPAM/pEG-d/AAc microgel system in great detail and provide the requisite background theory for understanding the methods used.

2.2 Synthesis and Chemistry

Our NIPAM/pEG-d/AAc microgels have 24 mol% AAc randomly copolymerized with 73 mol% NIPAM, and are crosslinked with 3 mol% poly(ethylene glycol) diacrylate (pEG-d), $CH_2CHCO-(OCH_2CH_2)_n-OCOCHCH_2$, where $n \sim 10$–11 is the number of repeat units. We note that each crosslinker chain has a molecular weight of 587 g/mol and is therefore 3.5–4 nm long [56]. The chemical structure of these components is shown in Fig. 2.1 together with a schematic of the chain structure.

The particles were synthesized for us with the assistance of Dr. Xiaobo Hu from the Lyon group in Georgia Tech's School of Chemistry and Biochemistry. We followed a dispersion polymerization synthesis according to previously published methods [57]. We added 9.08 g (73 mol%) of NIPAm, 1.92 g (3 mol%) of pEG-d (molecular weight ∼587 g/mol), 1.9

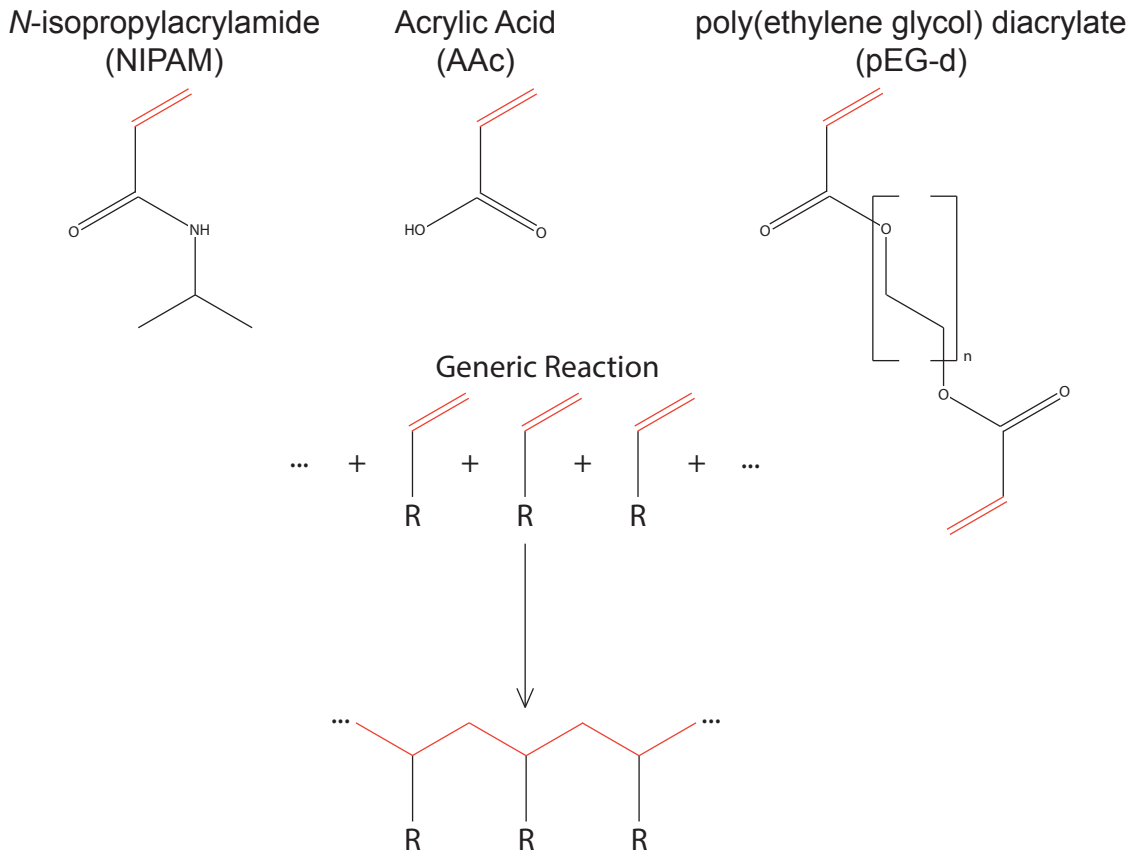

Figure 2.1: A schematic showing the components of the synthesis. The number of repeat units in the pEG-d is $n = 10$–11. The NIPAM and AAc monomers have one C–C double bond, shown in red, and the pEG-d has two, one at each end of the molecule. These double bonds are broken during the polymerization to form the chain backbone, which is shown in simplified form for clarity.

g (24 mol%) of AAc, 0.058 g of sodium dodecyl sulfate (a surfactant), and 0.342 g of ammonium persulfate (the reaction initiator) to 1587 mL DI water at 70 °C. We allowed the reaction to proceed for 8 hrs while stirring at 350 rpm, then cooled the dispersion to room temperature and removed aggregates by filtering the product through glass wool. To remove unreacted monomer, cross-linker, surfactant, and initiator molecules, we dialyzed the suspension against DI water refreshed daily for four weeks using a Speactra/Por dialysis membrane.

The membrane was previously sterilized by boiling and had a molecular weight cutoff of 12,000-14,000 g/mol. We prepare dilute samples by adding small amounts of the stock directly to DI water, and concentrated samples by freeze-drying the stock and resuspending

the resulting powder. We adjusted pH with sodium hydroxide (NaOH) or hydrochloric acid (HCl). When adjusting the pH we were careful to add only just enough acid/base to reach the desired pH, rather than overshooting and trying to re-adjust the pH. In this way we avoid including an excess of salt in the suspension.

Microgels with similar composition have been studied extensively [58–65]. However, with the exception of [63], experimental studies of pNIPAM/AAc microgels have restricted themselves to AAc fractions of less than 10 mol%. In the case of [63], the focus was on the mesh size of the resulting microgels. Further, it is worth noting that the use of pEG-d as a crosslinker is quite unusual, with N,N'-methylenebisacrylamide (BIS) being far more commonly used. pEG-d is hydrophilic, and can be more so than pNIPAM for some T below the LCST [66, 67]. Previous work [65] has been performed on pNIPAM microgels crosslinked with pEG-d, finding an unusual two-step decrease of R_{h} with increasing temperature, which was attributed to the hydrophilicity of pEG-d. However, no AAc was included in that synthesis.

2.3 Viscometry and Calculating Generalized Volume Fraction

The behavior of colloidal particles in suspension depends on whether and how the particles are interacting. For the simplest case of idealized hard spheres, the only interaction is excluded volume. The relevant thermodynamic quantity in this case is the volume fraction, $\phi = Nv^{\mathrm{P}}/V$, where N is the number of particles in the sample, $v^{\mathrm{P}} = (4\pi/3)R^3$ is the volume of one particle with radius R, and V is the total volume of the sample. ϕ can be easily related to concentration or weight fraction via the dynamic viscosity of the suspension, η, for dilute conditions using the Einstein-Batchelor equation [68–71]:

$$\eta/\eta_s = 1 + 2.5\phi + 5.9\phi^2, \tag{2.1}$$

where η_s is the viscosity of the solvent used. The volume fraction is given by $\phi = kc$, where c is a measure of the suspension concentration and k is a constant. In our analysis we use weight percent, $c = [m_{\mathrm{dry}}/(m_{\mathrm{dry}} + m_{\mathrm{solvent}})] \times 100\%$. From Eq. 2.1 and a plot of η/η_{s} vs. c, we obtain k, which can be used to determine ϕ even at high c.

However, for soft particles that can deform, compress, and/or interpenetrate, the particle shape and volume may change. In this case, it is more difficult to determine ϕ at high c. We make use of a generalized volume fraction, defined as $\zeta = Nv_0^{\mathrm{P}}/V$, where $v_0^{\mathrm{P}} = (4\pi/3)R_0^3$ is the volume of one particle in dilute conditions, with R_0 the corresponding radius. Unlike ϕ, which has an upper bound of 1, suspensions with $\zeta > 1$ are possible, since the particles can deform, compress, and/or interpenetrate. For dilute samples, $\zeta = \phi$ and Eq. 2.1 can still be used to determine k, which is then used to determine ζ from c for samples of any concentration.

We emphasize that ζ is proportional to the concentration of the suspension. However, v_0^{P} depends on the swelling state of our particles, which is controlled by temperature and pH. Thus, ζ is as much a function of T and pH as of c.

Suppose we have a suspension of some c, at conditions for which we have already measured k. By changing T and/or pH, we change k and therefore ζ, even though c is fixed. However, because $\zeta \propto R_0^3$, we can determine the new ζ if we know R_0 at both sets of conditions. In Section 2.4, we report the hydrodynamic particle radius, R_{h}, for all T and pH. By taking $R_0 = R_{\mathrm{h}}$, we can determine ζ at any set of conditions, provided we know k at one set of conditions, using the following relationship:

$$\frac{\zeta(T_1, \mathrm{pH}_1)}{\zeta(T_2, \mathrm{pH}_2)} = \frac{k(T_1, \mathrm{pH}_1)}{k(T_2, \mathrm{pH}_2)} = \left[\frac{R_{\mathrm{h}}(T_1, \mathrm{pH}_1)}{R_{\mathrm{h}}(T_2, \mathrm{pH}_2)}\right]^3. \tag{2.2}$$

We perform viscometric measurements on suspensions over a range of concentrations at pH $= 3.99 \pm 0.07$ and 4.54 ± 0.19, $T = 14.1$, 24.4, 30.1, 38.9, and 58.3 °C ($\delta T \leqslant 0.1$ °C for all measurements). We use an Ubbelohde viscometer manufactured by Technical Glass Products, Inc., with a viscometer constant of 0.003121 cSt/s at all temperatures. We ensure uniform temperature throughout the measurement by immersing the viscometer in a heated or cooled water bath whose temperature we measure via thermocouple during the experiment and allowing the temperature of the sample to equilibrate for at least 15 minutes prior to each measurement.

We measure six efflux times for each combination of T and pH, averaging them together to obtain the final value and uncertainty. By multiplying the efflux time by the viscometer

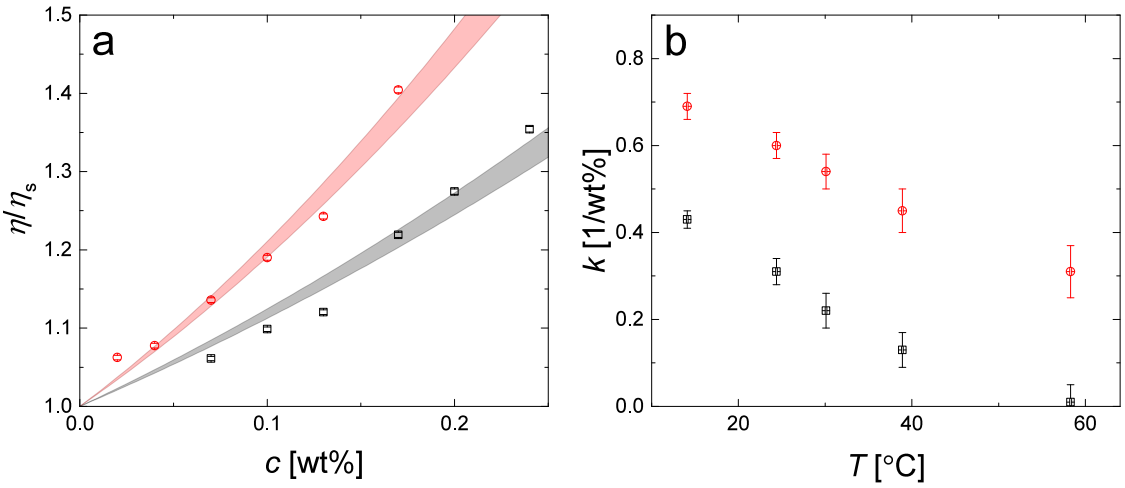

Figure 2.2: Viscometry measurements for our microgel system at selected conditions. (a) Relative viscosity as a function of concentration for two pHs, pH $= 3.99 \pm 0.07$ (black squares) and pH $= 4.54 \pm 0.19$ (red circles). For clarity, only one set of temperature measurements is shown, at $T = 14.1 \pm 0.1$ °C. Fits are to Eq. 2.1, with the width of the curve indicating uncertainty in k. (b) k values obtained from fitting the data to Eq. 2.1 as a function of temperature.

constant, we obtain the kinematic viscosity, ν, of the suspension, which is related to the dynamic viscosity, η, by $\nu = \eta/\rho$, with ρ the suspension density, which we take to be equal to that of water at the measured temperature. We obtain ρ for water as a function of temperature by interpolating the literature values [72] in Mathematica to obtain ρ for arbitrary temperatures. After obtaining the dynamic viscosity of each suspension, we finally calculate the relative viscosity using the empirical Watson-Basu-Sengers equation [73] for the temperature-dependent viscosity of water. We fit the results with Eq. 2.1, as shown in Fig. 2.2.

To confirm that we can accurately calculate ζ for other conditions using Eq. 2.2, we compare k values from Fig. 2.2 with those calculated using Eq. 2.2 and find good agreement using values of $R_\mathrm{h}(T, \mathrm{pH})$ obtained in Section 2.4. For example, the values of k at $T \sim 14$ °C are 0.43 ± 0.02 and 0.69 ± 0.03 for pH ~ 4 and ~ 4.5, respectively, giving $k(T = 14, \mathrm{pH} = 4)/k(T = 14, \mathrm{pH} = 4.5) = 0.6 \pm 0.1$. From Fig. 2.15 we find that at these conditions, $R_\mathrm{h} \approx 460 \pm 20$ nm and 550 ± 20 nm, respectively. From Eq. 2.2, we obtain the same ratio, $k = 0.6 \pm 0.15$. Following the same procedure, for the same pHs at $T = 28.7$ °C, we find the ratios of both k and R_h^3 to be 0.4 ± 0.1. Other conditions display a similar match.

We therefore use Eq. 2.2 to calculate ζ for other values of T and pH. The error using this method is $\lesssim 10\%$, comparable to the error in the viscometry measurements themselves.

2.4 Introduction to 3DDLS

In a typical dynamic light scattering (DLS) experiment, laser light is passed through a dilute suspension of particles. The time-dependent intensity fluctuations of coherent light scattered from the sample, which correspond to Brownian motion of the particles in suspension, contain information about their hydrodynamic size. The theory presented in this section largely applies to DLS experiments on concentrated systems as well, which will be discussed in more detail in Chapter V.

In the discussions presented below, we make several assumptions that are valid for all of our experiments [74]:

Born approximation. We take the total field everywhere in the scattering material as equal to the incident field. This is reasonable when only a small fraction of the incident light is scattered.

No attenuation of incident light by absorption. We assume that the solvent and particles do not absorb light.

Elastic scattering. We assume all scattering events are elastic, meaning that the photon wavelength does not change during a scattering event.

Small phase shift. The phase mismatch between light transmitted through the solvent and through the particle is assumed to be small, i.e. when $2\pi|n_\mathrm{p} - n_\mathrm{s}|R_\mathrm{h}/\lambda_0$ is small, with n_p and n_s the indices of refraction of the polymer and solvent, respectively, and λ_0 the wavelength of the light in vacuum.

Constant field direction. We assume that the field has the same wave vector everywhere in the scattering volume. This means we assume the incident light to have this property, and that refraction of light at the solvent–particle interface is negligible, i.e. that $|n_\mathrm{p} - n_\mathrm{s}|$ is small.

Far field approximation. We assume far-field behavior of the scattered light at the detector. This is true when $w^2/L\lambda_0 \ll 1$, where w is the detector aperture width and L is

the distance between the scattering volume and the detector, which is true for our setup.

The experimentally-measured quantity is intensity I as a function of scattering angle θ, shown schematically in Fig. 2.3, which is related to the scattered electric field strength E by

$$I = \frac{1}{2}\sqrt{\frac{\epsilon_{\mathrm{s}}}{\mu_0}}EE^*, \tag{2.3}$$

where ϵ_s and μ_0 are the solvent permittivity and the permeability, respectively, and only electric field components parallel to the scattering wave vector are considered [74]. The scattering wave vector is defined as $\mathbf{q} = \mathbf{k}_{\mathrm{i}} - \mathbf{k}_{\mathrm{f}}$, with $\mathbf{k}_{\mathrm{i}}$ and $\mathbf{k}_{\mathrm{f}}$ the initial and final wavevectors of the scattered light, respectively, and $q = (4\pi/\lambda)\sin(\theta/2)$, with $\lambda = \lambda_0/n$ the wavelength of the scattered light in the solvent and n the solvent index of refraction. "*" represents complex conjugation.

In the simplest type of DLS experiment, a single beam is passed through the sample and the measured intensity scattered into some angle is autocorrelated with itself. However, this experiment fails for samples with significant multiple scattering, which occurs when photons scatter from multiple particles before reaching the detectors. Because the q-dependence of the first scattering event is lost after subsequent scattering events, multiple scattering adds a random component to an autocorrelation experiment that cannot be corrected for or even estimated from the experimental data.

In a cross-correlation experiment, the influence of multiple scattering is suppressed. There are several types of cross-correlation setups [75]; ours is a 3D cross-correlation apparatus manufactured by LS Instruments.

A simplified schematic of our 3DDLS setup is shown in Fig. 2.3. A laser beam is split into two beams by a beamsplitter and focused into the sample. These two beams cross inside the sample; their overlap region is called the scattering volume. The sample chamber is temperature-controlled and filled with decahydronaphthalene, or decalin, an organic compound that has an index of refraction very close to that of glass, which minimizes refraction effects on the beam. The sample can be rotated by a goniometer either to a specific sample angle for each measurement or at a constant angular velocity during the measurement. Light from the scattering volume is incident into two photodetectors

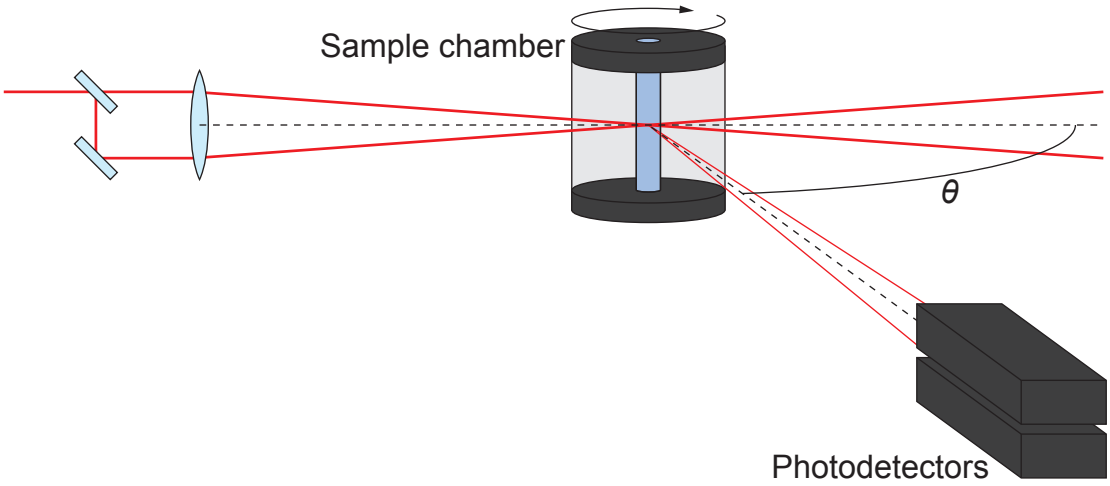

Figure 2.3: A simplified representation of our 3DDLS instrument as described in the text. Not to scale.

positioned in such a way that **q** from one beam into one detector is the same as **q** from the other beam into the other detector. A second goniometer allows the detectors to be rotated around the sample chamber to any scattering angle $15° \leqslant \theta \leqslant 150°$, although to minimize the effects of imperfect alignment we restrict our measurements to $20° \leqslant \theta \leqslant 140°$. The two detectors measure time-dependent intensity fluctuations which are correlated together. Since there are two beams and two photodetectors, there are effectively four experiments being performed. The ensemble-averaged intensity cross-correlation function (ICCF) is thus defined as:

$$\begin{aligned} G_I^{(\mathrm{E})}(q,\tau) =& \langle I_1(q,t) I_2(q,t+\tau)\rangle_{\mathrm{E}} \\ =& \left\langle \left[I_1^1(q,t) + I_1^2(q,t)\right]\left[I_2^1(q,t+\tau) + I_2^2(q,t+\tau)\right]\right\rangle_{\mathrm{E}} \\ =& \langle I_1^1(q,t) I_2^1(q,t+\tau)\rangle_{\mathrm{E}} + \langle I_1^2(q,t) I_2^1(q,t+\tau)\rangle_{\mathrm{E}} \\ &+ \langle I_1^2(q,t) I_2^2(q,t+\tau)\rangle_{\mathrm{E}} + \langle I_1^1(q,t) I_2^2(q,t+\tau)\rangle_{\mathrm{E}}. \end{aligned} \tag{2.4}$$

The brackets $\langle\cdots\rangle_{\mathrm{E}}$ and superscript "$^{(\mathrm{E})}$" represent ensemble averages of the measured quantities. For an ergodic system, defined as one that explores all of phase space over the duration of the experiment, a time average, $\langle\cdots\rangle_{\mathrm{T}}$, is equivalent. 3DDLS of a non-ergodic system is not trivial, and we discuss it in Appendix B. Superscripts within the averages refer to beam number and subscripts to detector number. Each of these terms represents a different scattering experiment: for example, the first term represents the experiment

correlating the fluctuations of beam 1 measured by detector 1 with those of beam 1 by detector 2; the second, beam 2 by detector 1 with beam 1 by detector 2; and so on. Each term has the same average, time-independent intensity (namely, 1/4 of the total). Of these four terms, only the fourth has the same $\mathbf{q}$ for both beams. The other three compare unrelated fluctuations and decorrelate. Further, in an ideal, ensemble-averaged system, the total amount of intensity scattered into detector 1 is equal to the total amount of intensity scattered into detector 2, and the contributions of those intensities from beam 1 are the same as the contributions from beam 2. Thus, Eq. 2.4 can be rewritten as

$$G_I^{(\mathrm{E})}(q,\tau) = \frac{3}{4}\langle I(q)\rangle_{\mathrm{E}}^2 + \langle I_1^1(q,t) I_2^2(q,t+\tau)\rangle_{\mathrm{E}}. \tag{2.5}$$

Here, the total measured intensity (summing contributions from both beams measured in both detectors) has been written $\langle I(q)\rangle_{\mathrm{E}}$. The factor of 3/4 is due to the three decorrelated contributions, while the remaining term is the correlated one. In a real experiment, $\langle I_1^1(q)\rangle_{\mathrm{E}}$, $\langle I_1^2(q)\rangle_{\mathrm{E}}$, $\langle I_2^1(q)\rangle_{\mathrm{E}}$, and $\langle I_2^2(q)\rangle_{\mathrm{E}}$ may not be exactly equal due to imperfections in the instrument's alignment. However, this is accounted for in the intercept as described below.

Intensity is proportional to the square of the electric field; the cross-correlation term in Eq. 2.5 is then a four-point average of electric fields, which when ensemble-averaged are also zero-mean Gaussian variables. Wick's theorem allows such a four-point average to be rewritten as a sum of two-point averages. This allows us to decompose the cross-correlation term into another average intensity term and the dynamic structure factor, equivalent to the ensemble-averaged electric field cross-correlation function $G_E^{(\mathrm{E})}(q,\tau)$ [74]:

$$\begin{aligned}
\langle I_1^1(q,t) I_2^2(q,t+\tau)\rangle_{\mathrm{E}} =& K\langle E_1^1(q,t) E_1^{1*}(q,t) E_2^2(q,t+\tau) E_2^{2*}(q,t+\tau)\rangle_{\mathrm{E}} \\
=& K\left[\langle E_1^1(q,t) E_1^{1*}(q,t)\rangle_{\mathrm{E}}\langle E_2^2(q,t+\tau) E_2^{2*}(q,t+\tau)\rangle_{\mathrm{E}}\right. \\
&+ \langle E_1^1(q,t) E_2^2(q,t+\tau)\rangle_{\mathrm{E}}\langle E_1^{1*}(q,t) E_2^{2*}(q,t+\tau)\rangle_{\mathrm{E}} \\
&+ \left.\langle E_1^1(q,t) E_2^{2*}(q,t+\tau)\rangle_{\mathrm{E}}\langle E_1^{1*}(q,t) E_2^2(q,t+\tau)\rangle_{\mathrm{E}}\right]
\end{aligned} \tag{2.6}$$

Here, we have defined $K = \epsilon_{\mathrm{s}}/4\mu_0$.

The first term is equivalent to $\langle I(q)\rangle_{\mathrm{E}}^2/4$. This is *not* the singly-scattered component as in Eq. 2.10 below, since this term has no cross-correlation and so is just a product of measured ensemble-averaged intensities. The second term is zero for nonzero scattering

vectors; heuristically, this can be understood as due to the fact that the two-point averages are not of complex-conjugated fields. As a result, the averages are of sinusoidal functions over all t, and tend to zero unless $q = 0$. The third term then defines $G_E^{(\mathrm{E})}(q,\tau)$:

$$\left|G_E^{(\mathrm{E})}(q,\tau)\right|^2 = K\langle E_1^1(q,t)E_2^{2*}(q,t+\tau)\rangle_{\mathrm{E}}\langle E_1^{1*}(q,t)E_2^2(q,t+\tau)\rangle_{\mathrm{E}}. \tag{2.7}$$

We then obtain

$$G_I^{(\mathrm{E})}(q,\tau) = \langle I(q)\rangle_{\mathrm{E}}^2 + \left|G_E^{(\mathrm{E})}(q,\tau)\right|^2. \tag{2.8}$$

Normalizing gives

$$g_I^{(\mathrm{E})}(q,\tau) = \frac{G_I^{(\mathrm{E})}(q,\tau)}{\lim_{\tau\to\infty} G_I^{(\mathrm{E})}(q,\tau)} = \frac{G_I^{(\mathrm{E})}(q,\tau)}{\langle I(q)\rangle_{\mathrm{E}}^2} \tag{2.9}$$

and

$$\left|g_E^{(\mathrm{E})}(q,\tau)\right|^2 = \frac{\left|G_E^{(\mathrm{E})}(q,\tau)\right|^2}{\left|G_E^{(\mathrm{E})}(q,0)\right|^2} = \frac{\left|G_E^{(\mathrm{E})}(q,\tau)\right|^2}{K\left|\langle E_1^1(q,t)E_2^{2*}(q,t)\rangle_{\mathrm{E}}\right|^2}. \tag{2.10}$$

For practical purposes, the cross-correlation term in the denominator on the right-hand side of Eq. 2.10 contains only contributions from single-scattered photons [75]. Therefore the total ensemble-averaged single-scattered intensity is given by $K\left|\langle E_1^1(q,t)E_2^{2*}(q,t)\rangle_{\mathrm{E}}\right|^2 = \langle I^{(1)}(q)\rangle_{\mathrm{E}}^2/4$, where again the 4 in the denominator is due to the fact that only 1/4 of the scattered intensity is correlated. We then obtain the normalized Siegert relation, defining the relationship between the intensity and electric field correlation functions:

$$g_I^{(\mathrm{E})}(q,\tau) - 1 = \frac{1}{4}\frac{\langle I^{(1)}(q)\rangle_{\mathrm{E}}^2}{\langle I(q)\rangle_{\mathrm{E}}^2}\left|g_E^{(\mathrm{E})}(q,\tau)\right|^2. \tag{2.11}$$

An empirical prefactor, β_0, accounts for experimental imperfections, such as in the alignment [75]:

$$g_I^{(\mathrm{E})}(q,\tau) - 1 = \beta_0\frac{1}{4}\frac{\langle I^{(1)}(q)\rangle_{\mathrm{E}}^2}{\langle I(q)\rangle_{\mathrm{E}}^2}\left|g_E^{(\mathrm{E})}(q,\tau)\right|^2. \tag{2.12}$$

Thus in a cross-correlation experiment the intercept accounts not only for experimental imperfections, but also multiple scattering contributions that reduce the signal strength, as well as a factor of 1/4 resulting from the four combinations of beams and detectors. The final Siegert relation is then

$$g_I^{(\mathrm{E})}(q,\tau) - 1 = \beta\left|g_E^{(\mathrm{E})}(q,\tau)\right|^2, \tag{2.13}$$

with

$$\beta = \beta_0 \frac{1}{4} \frac{\langle I^{(1)}(q) \rangle_{\mathrm{E}}^2}{\langle I(q) \rangle_{\mathrm{E}}^2}. \tag{2.14}$$

From Eq. 2.14, we can determine the single-scattered intensity contribution to any measurement by comparing with a reference measurement on an exclusively single-scattering system. Such a reference measurement yields an intercept of $\beta^{\mathrm{ref}} = \beta_0/4$, and the single-scattered intensity can be isolated as

$$\langle I^{(1)}(q) \rangle_{\mathrm{E}} = \langle I(q) \rangle_{\mathrm{E}} \sqrt{\frac{\beta}{\beta^{\mathrm{ref}}}}. \tag{2.15}$$

The practical details of a multiple scattering correction will be covered in Section 2.6.6. Note that β_0, and thus β^{ref}, are dependent on scattering angle in a real experiment, and the imperfections in alignment will be more pronounced at lower scattering angles, as discussed in section 2.6.4. β may also include an additional q-dependence related to the individual particle form factor, as we discuss in Section 2.5.

2.4.1 A Diffusive, Monodisperse System

In a monodisperse system of diffusive particles undergoing Brownian motion, the normalized dynamic structure factor can simply be written as [74]

$$\left| g_E^{(\mathrm{E})}(q, \tau) \right| = \exp\left(-\Gamma \tau\right), \tag{2.16}$$

where $\Gamma = Dq^2$ is the relaxation frequency of the particles, with D the diffusion coefficient of one particle in three dimensions. D is related to the particle's hydrodynamic radius R_{h} by the Stokes-Einstein equation [76],

$$R_{\mathrm{h}} = \frac{k_{\mathrm{B}} T}{6\pi\eta_{\mathrm{s}} D}. \tag{2.17}$$

R_{h} is very close to the actual radius of a microgel, since even microgels with quite low crosslinker densities are hydrodynamically opaque [77]. As shown in Fig. 2.4, we fit a simple exponential decay to Eq. 2.16 to obtain Γ as a function of q^2, perform a linear fit to obtain D and the associated uncertainty in our measurement, and finally use Eq. 2.17 to determine R_{h} for our sample.

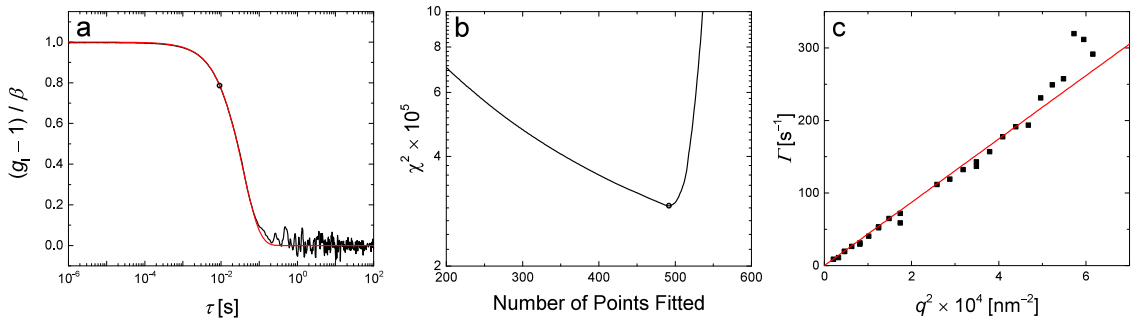

Figure 2.4: Representative results from running our Matlab program. (a) A best fit (red line) of Eq. 2.16 to our experimental data (black line). The black circle shows the end of the fitted portion of the data. (b) A plot of χ^2 vs. the number of points fitted in panel (a). The best fit is the one to the first 493 points, shown as a black circle. (c) A plot of the resulting Γ vs. q^2 (black squares) along with a best fit $\Gamma = Dq^2$, with the slope of the fit (red line) giving the diffusion coefficient D.

To perform the fit, we use a Matlab program designed to exclude common sources of error. The program first disregards any unphysical measurements caused by glitches in the hardware by checking that the first 200 points in each experimental ICCF are positive. The data sets that remain, however, often contain large contributions from noise at high τ. In order to minimize contributions from noise and obtain the best fit, we use the following algorithm:

We fit Eq. 2.16 to the first 200 points only, and obtain χ^2, Pearson's goodness-of-fit parameter [78]. We then repeat the fit for the first 201 points, then 202, and so on, continuing until the ICCF first becomes negative. This is an unavoidable consequence of experimental noise for high τ when the correlation function tends to zero. The fit with the minimum χ^2 value is selected as the best fit. This is repeated for all measurements to obtain an output file with one Γ for each measurement. We have compared this extensively against manual fits to ICCFs for suspensions of particle standards and for experimental samples, and in all cases the program has agreed well, meaning that it can be trusted to produce the correct values of Γ without the tedium of fitting each of hundreds of data points by hand. The output from this program allows us to plot Γ vs. q^2 and thereby obtain D for that sample, as shown in Fig. 2.4.

2.4.2 Polydispersity in a Diffusive System: the Method of Cumulants

For diffusive, polydisperse systems, Eq. 2.16 does not hold. Instead, the dynamic structure factor must be expressed by an integral over the decay rate:

$$\left|g_E^{(\mathrm{E})}(q,\tau)\right| = \int_0^\infty \mathrm{d}\Gamma G(\Gamma)\exp\left(-\Gamma\tau\right), \tag{2.18}$$

where $G(\Gamma)$ is the decay rate distribution normalized such that $\int_0^\infty \mathrm{d}\Gamma G(\Gamma) = 1$.

Our program can be used to estimate the average diffusion coefficient and polydispersity for slightly polydisperse samples using the method of cumulants [79]. In this analysis, the natural logarithm of the dynamic structure factor is written as a Taylor series in τ,

$$\begin{aligned}\log_e\left|g_E^{(\mathrm{E})}(q,\tau)\right| &= \sum_{m=1}^{\infty}\frac{k_m}{m!}(-\tau)^m, \\ &= k_1\tau + \frac{k_2}{2}\tau^2 + \cdots,\end{aligned} \tag{2.19}$$

usually truncated to second order. The coefficients in the expansion are called cumulant coefficients; they generally depend on the details of the decay rate distribution. For short times, the behavior is that of monodisperse suspensions, with $\log_e\left|g_E^{(\mathrm{E})}(q,\tau)\right|$ linear in τ, but with a slope that is equal to the mean decay rate [74], $\bar{\Gamma} = \int_0^\infty \mathrm{d}\Gamma G(\Gamma)\Gamma$. Hence, as defined in Eq. 2.19, $k_1 = \bar{\Gamma}$.

For larger τ, the second cumulant can be used to meaningfully describe the polydispersity when $G(\Gamma)$ is sharply peaked. In this case, we write

$$\begin{aligned}\exp(-\Gamma\tau) &= \exp(-\bar{\Gamma}\tau)\exp\left[-(\Gamma-\bar{\Gamma})\tau\right] \\ &= \exp(-\bar{\Gamma}\tau)\left[1-(\Gamma-\bar{\Gamma})\tau + \frac{(\Gamma-\bar{\Gamma})^2}{2}\tau^2 + \cdots\right],\end{aligned} \tag{2.20}$$

in which we have Taylor expanded the second exponential on the right hand side around $\Gamma = \bar{\Gamma}$. By again truncating to second order, Eq. 2.18 becomes

$$\begin{aligned}\log_e\left|g_E^{(\mathrm{E})}(q,\tau)\right| &= \exp(-\bar{\Gamma}\tau)\times\int_0^\infty \mathrm{d}\Gamma G(\Gamma)\left[1-(\Gamma-\bar{\Gamma})\tau + \frac{(\Gamma-\bar{\Gamma})^2}{2}\tau^2\right] \\ &= \exp(-\bar{\Gamma}\tau)\left(1+\frac{k_2}{2}\tau^2\right),\end{aligned} \tag{2.21}$$

where $k_2 = \int_0^\infty \mathrm{d}\Gamma G(\Gamma)(\Gamma-\bar{\Gamma})^2$ is the variance of the distribution. Taking the natural logarithm, expanding $\log_e(1+k_2\tau^2/2)$ around $\tau = 0$, and keeping terms up to second order

recovers Eq. 2.19. The relative polydispersity of the suspension then follows from the first and second cumulants as $\sqrt{k_2/k_1^2}$.

For very polydisperse systems, or systems in which the distribution is not monomodal, the method of cumulants fails. In such situations, the problem of determining the size distribution is an ill-posed one. Obtaining the distribution from the correlation function in this case requires sophisticated inversion algorithms [80].

2.5 Introduction to SLS

The setup for a static light scattering (SLS) experiment is identical to that of a DLS experiment, and the two types of experiments can usually be performed simultaneously. Laser light is passed through a suspension of particles and the scattered light is collected as described in Section 2.4. However, rather than correlating the time-dependent intensity fluctuations, we look for information about the sample's structure in the time-*in*dependent, ensemble-averaged intensity.

The ensemble-averaged intensity scattered by an m-component system of spherically symmetric particles is given by [81]

$$\langle I^{(1)}(q)\rangle_{\mathrm{E}} \propto \sum_{i,j=1}^{m} \sqrt{n_i n_j} B_i(q) B_j(q) \left[\delta_{ij} + \hat{h}_{ij}(q)\right], \tag{2.22}$$

where the "$^{(1)}$" denotes that only single-scattered intensity is considered. We neglect a constant prefactor $I_0 V_{\mathrm{s}} \mathbf{k}_{\mathrm{i}}^4 / L^2 (4\pi)^2$, where I_0 is the incident intensity and V_{s} is the scattering volume, which is dependent only on the instrument geometry. Here, $B_i(q)$ is the scattering amplitude and n_i the number density of component i, δ_{ij} is the Kronecker delta, and $\hat{h}_{ij}(q) = \sqrt{n_i n_j}\mathcal{F}\left\{h_{ij}(r)\right\}(q)$ is the number-density-weighted Fourier transform of $h_{ij}(r) = g_{ij}(r) - 1$, with $g_{ij}(r)$ the radial distribution function as a function of the distance between the centers of species i and j.

Eq. 2.22 can be rewritten as

$$\langle I^{(1)}(q)\rangle_{\mathrm{E}} \propto \sum_{i,j=1}^{m} \sqrt{n_i n_j} B_i(q) B_j(q) S_{ij}(q), \tag{2.23}$$

where $S_{ij}(q)$ are the components of the structure factor tensor $\mathbb{S}(q)$, which quantifies the inter-particle scattering contributions [82–88]. $\mathbb{S}(q)$ is symmetric, and because of the factor

of $\sqrt{n_i n_j} B_i(q) B_j(q)$ in Eq. 2.23, the importance of the ijth component is weighted by the number density and scattering amplitudes of particle species i and j.

In the dilute case, $\mathbb{S}(q)$ reduces to the identity matrix and Eq. 2.23 to

$$\langle I^{(1)}(q) \rangle_{\mathrm{E}} \propto \sum_{i=1}^{m} n_i B_i^2(q), \tag{2.24}$$

which contains only intra-particle scattering contributions. This term defines the form factor,

$$\langle I^{(1)}(q) \rangle_{\mathrm{E}} \propto P(q) = \frac{\sum_{i=1}^{m} n_i B_i^2(q)}{\sum_{i=1}^{m} n_i B_i^2(0)}. \tag{2.25}$$

In the monodisperse case, $m = 1$, $\mathbb{S}(q)$ has only one term, and Eq. 2.23 reduces to

$$\langle I^{(1)}(q) \rangle_{\mathrm{E}} \propto P(q) S(q). \tag{2.26}$$

In this case, the structure factor can be extracted directly from the data by dividing the $I^{(1)}(q)$ by $P(q)$, *provided that the form factor $P(q)$ is unchanged from the dilute case.* This condition is often assumed, but is not generally valid [89].

In practice, the structure factor tensor cannot be experimentally disentangled from the scattering amplitudes. This leads to what is called the "measurable" structure factor [90–93], $S_{\mathrm{M}}(q)$, defined as

$$S_{\mathrm{M}}(q) = \frac{\sum_{i,j=1}^{m} \sqrt{n_i n_j} B_i(q) B_j(q) S_{ij}(q)}{\sum_{i=1}^{m} n_i B_i^2(q)}, \tag{2.27}$$

leading to

$$\langle I^{(1)}(q) \rangle_{\mathrm{E}} \propto P(q) S_{\mathrm{M}}(q) \tag{2.28}$$

Combined with the fact that the dependence of $P(q)$ on concentration is unkown, this makes the interpretation of scattering data at high concentrations more difficult. For example, while the structure factor of monodisperse [94–101] and polydisperse [83–85, 102, 103] hard spheres can both be solved for analytically, the polydisperse case is considerably more complicated. Polydispersity has been taken into account for a variety of non-hard-sphere models as well [87, 88, 90, 91, 104–106]. Such models have been used to evaluate the measurable structure factor of concentrated emulsions [93].

In the following subsections we discuss the scattering amplitudes and form factors, as well as the single-particle radial density functions, of three important models for colloidal microgels relevant to our work: homogeneous sphere, core-shell, and star polymer.

The total form factor of a polydisperse system is given by Eq. 2.25. For a monodisperse system there is only one term. The scattering amplitude of component i in a system with m components is defined by the Fourier transform of the particles' scattering amplitude density, which is effectively proportional to their mass density,

$$B(q) = \mathcal{F}\left\{\rho(r)\right\}. \tag{2.29}$$

We assume that the particles' scattering contrast and density are proportional, $\rho(r) \propto (n_\mathrm{p} - n_\mathrm{s})/n_\mathrm{s}$. This is reasonable because n_s is a constant, and the values of $\mathrm{d}n/\mathrm{d}c$ in water of pNIPAM [107], poly(acrylic acid) [108], and pEG-d [109] are known and are constant with respect to c.

Regardless of the details of the particle structure, all form factors have the same behavior if qR, the product of q and the particle size, is small enough [110]. This can be seen most simply by considering Eq. 2.25 with $m = 1$ together with Eqs. 2.29 and A.3 and Taylor expanding around $qR = 0$, keeping only terms up to second order. The first-order term vanishes, leaving

$$\begin{aligned}
\lim_{qR\to 0} P(q) &= 1 - \left[\frac{\int_0^\infty r^4 \mathrm{d}r\rho(r)}{\int_0^\infty r^2 \mathrm{d}r\rho(r)}\right]\left(-\frac{q^2}{3}\right) + \cdots, \\
&= 1 - \frac{(qR_\mathrm{g})^2}{3}, \\
&\approx \exp\left[-\frac{(qR_\mathrm{g})^2}{3}\right],
\end{aligned} \tag{2.30}$$

where R_g, the radius of gyration, is defined as the square root of the term in square brackets on the first line, and represents a measure of the distribution of mass inside each particle. We emphasize again that this definition assumes equivalence between optical density and mass density, as discussed above. The region in which this approximation is valid, typically taken to be $qR_\mathrm{g} \lesssim 2.5$ [74], is called the Guinier regime.

Generally, we write the polydisperse form factor as an integral over the monodisperse

form factor multiplied by some distribution, such as a Gaussian:

$$P(q) = \frac{1}{\sqrt{2\pi}\sigma_{\mathrm{p}}\langle R\rangle} \int \mathrm{d}R_i P_i(q, R_i) \times \exp\left[-\frac{1}{2}\left(\frac{R_i - \langle R\rangle}{\sigma_{\mathrm{p}}\langle R\rangle}\right)^2\right]. \tag{2.31}$$

Here $\langle R\rangle$ and σ_{p} are the mean particle radius and the width of the Gaussian, respectively.

At small enough length scales, we can no longer take the mass density to be essentially smooth. We must consider the molecular structure of our particles, which in our case are crosslinked polymer networks. In this regime, the correlations between polymer segments on the same chain dominate the scattering behavior. The pair correlation function of this component is written as [111]

$$G(r) \sim \left(\frac{r}{\ell}\right)^{D_{\mathrm{f}}} r^{-3} \exp(-r/\xi), \tag{2.32}$$

where ℓ is the segment length of the polymer, D_{f} is the fractal dimension of the network, and ξ is the local blob size of the polymer. The exponential term acts as a cut-off, since this component dominates only for $r < \xi$. Fourier transformation then yields the network term of the particle form factor:

$$P^{\mathrm{net}}(q) \propto \frac{\Gamma(\mu)}{q\xi} \frac{\sin\left[\mu \arctan(q\xi)\right]}{\left[1 + (q\xi)^2\right]^{\mu/2}}, \tag{2.33}$$

where Γ is the gamma function and $\mu = D_{\mathrm{f}} - 1$. This term has three special cases, namely $\mu = 0$, $\mu = 1$, and $\mu = 2$, corresponding to the cases of $D_{\mathrm{f}} = 1$, 2, and 3, respectively:

$$P^{\mathrm{net}}(q) \propto \frac{\arctan(q\xi)}{q\xi} \qquad \mu \to 0, \tag{2.34a}$$

$$P^{\mathrm{net}}(q) \propto \frac{1}{1 + (q\xi)^2} \qquad \mu = 1, \tag{2.34b}$$

$$P^{\mathrm{net}}(q) \propto \frac{1}{\left[1 + (q\xi)^2\right]^2} \qquad \mu = 2. \tag{2.34c}$$

Eqs. 2.34b and c are the Lorentzian [112, p. 82-85] and Debye-Bueche [113, 114] network terms, respectively. Fig. 2.5 compares the three cases.

In principle, there might be more than one blob size ξ and more than one dimensional term μ even within a single particle. For example, if the core is denser than the periphery, the polymer segments in the core might be more stretched (lower μ) and correlated on smaller length scales (smaller ξ). The star polymer model of Daoud and Cotton [115] has ξ

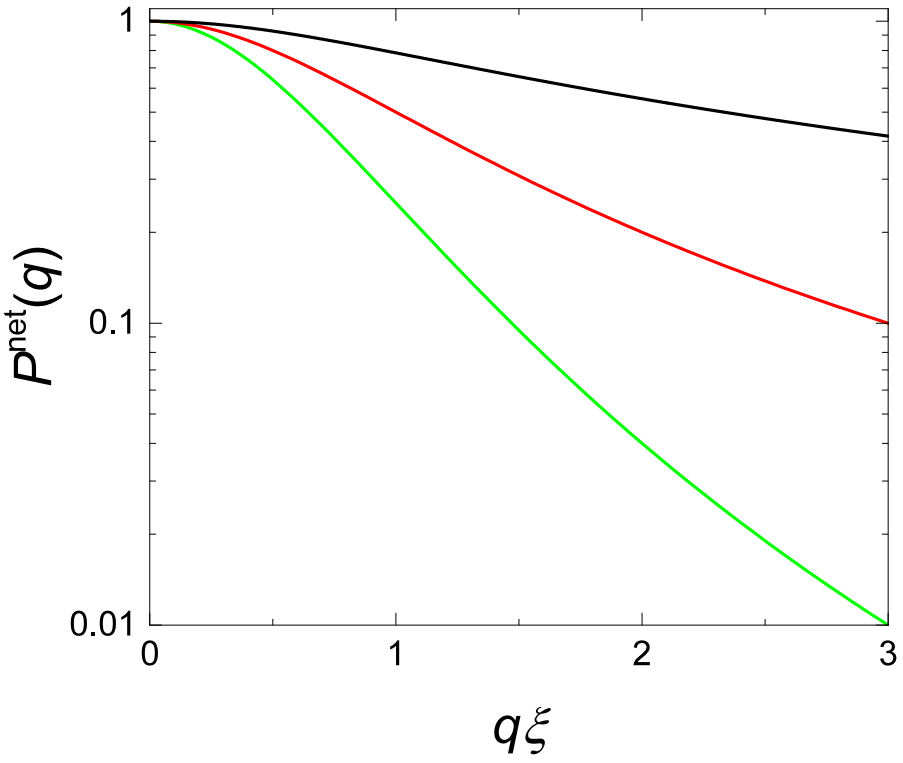

Figure 2.5: Form factor network terms from Eq. 2.33 showing $P^{\text{net}}(q)$ as a function of $q\xi$. The black, red, and green lines show the $\mu = 0$, $\mu = 1$ (Lorentzian), and $\mu = 2$ (Debye-Bueche) cases, respectively.

decrease linearly with r as the core is approached, because less volume is available to each arm. However, we find that allowing multiple values of ξ and μ overfits our data, so we take the fitted values to be "average" ξ and μ.

Adding the polydisperse form factor and the network term together, and including a constant term I_0 to account for background scattering, gives the final form factor we use to describe our microgels:

$$P(q) = I_1 \frac{1}{\sqrt{2\pi}\sigma_{\text{p}}\langle R\rangle} \int \mathrm{d}R_i P_i(q, R_i) \times \exp\left[-\frac{1}{2}\left(\frac{R_i - \langle R\rangle}{\sigma_{\text{p}}\langle R\rangle}\right)^2\right] + I_2 \frac{\Gamma(\mu)}{q\xi} \frac{\sin\left[\mu \arctan(q\xi)\right]}{[1 + (q\xi)^2]^{\mu/2}} + I_0. \tag{2.35}$$

$P(q = 0) = 1$ by definition. Because the first term dominates at low q, we effectively meet this requirement by setting $I_1 = 1$. Three model $P_i(q)$ are given in the following sections, with $R_i = R_{\text{c},i}$ the core radius (for the core-shell model) and $R_i = R_{\text{g},i}$ the radius of gyration (for the star polymer model). Fig. 2.6 compares these three models.

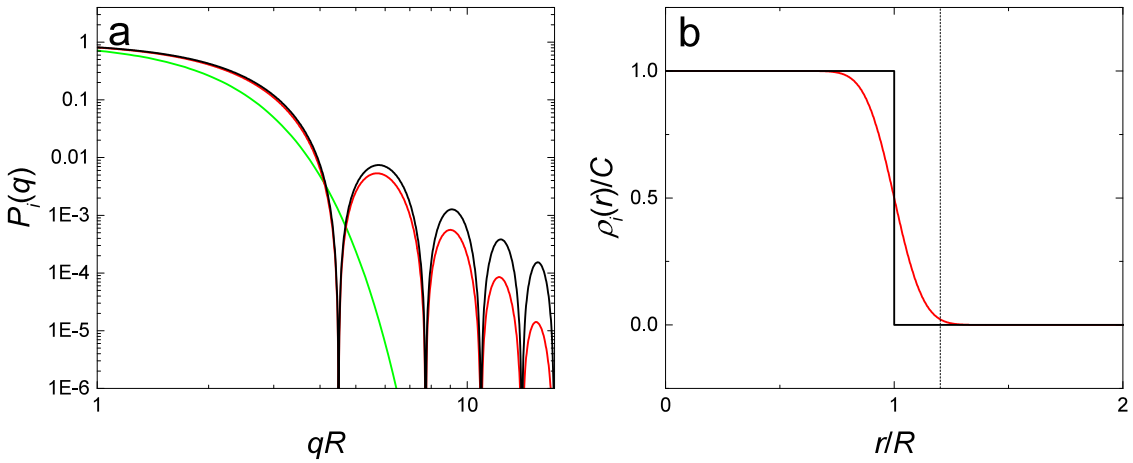

Figure 2.6: (a) Form factor models described in the text. The black line shows the homogeneous sphere model from Eq. 2.40, $P_i^{\mathrm{HS}}(q)$ vs. qR_i. The red line shows the core-shell model from Eq. 2.44, $P_i^{\mathrm{CS}}(q)$ vs. $qR_{\mathrm{c},i}$ with $\sigma_{\mathrm{surf}}/R_{\mathrm{c},i} = 0.1$. The green line shows the Guinier decay from Eqs. 2.30 and 2.46, $P_i^{\mathrm{star}}(q)$ vs. $qR_{\mathrm{g},i}$. (b) Density profiles $\rho(r)$ for the models under consideration. The black line shows the homogeneous sphere model from Eq. 2.36, $\rho_i^{\mathrm{HS}}(r)$ vs. r/R_i. The red line shows the core-shell model from Eq. 2.45, $\rho_i^{\mathrm{CS}}(r)$ vs. $r/R_{\mathrm{c},i}$ with $\sigma_{\mathrm{surf}}/R_{\mathrm{c},i} = 0.1$. The vertical dashed line shows the total radius of the particle, taken to be $R_{\mathrm{SLS,i}} = R_{\mathrm{c},i} + 2\sigma_{\mathrm{surf}}$.

2.5.1 Form Factor Models: Homogeneous Sphere

This is the simplest case, with radial density given by

$$\rho^{\mathrm{HS}}(r) = \begin{cases} C & r < R_i \\ 0 & r > R_i \end{cases}. \tag{2.36}$$

with R_i the sphere radius of the particles and C a constant with units of density. Applying Eqs. 2.29 and A.2 gives

$$B_i^{\mathrm{HS}}(q) = C\sqrt{\frac{2}{\pi}}\int_0^\infty r^2 \mathrm{d}r \frac{\sin qr}{qr} \times \begin{cases} 1 & r < R_i \\ 0 & r > R_i \end{cases}. \tag{2.37}$$

Evaluating the integral gives the particle scattering amplitude:

$$B_i^{\mathrm{HS}}(q) = C\sqrt{\frac{2}{\pi}}\frac{\sin qR_i - qR_i \cos qR_i}{q^3}. \tag{2.38}$$

Evaluating Eq. 2.38 at $q = 0$ gives

$$B_i^{\mathrm{HS}}(0) = C\sqrt{\frac{2}{\pi}}\frac{R_i^3}{3}. \tag{2.39}$$

Following Eq. 2.25, the components of the polydisperse homogeneous sphere form factor are then

$$P_i^{\mathrm{HS}}(q) = \left[3\frac{\sin qR_i - qR_i\cos qR_i}{(qR_i)^3}\right]^2. \tag{2.40}$$

2.5.2 Form Factor Models: Core-Shell

An extension of the homogeneous sphere model is the core-shell model where the radial density function is represented as the convolution of a box function (i.e. hard sphere) with a Gaussian in order to represent a "fuzzy" particle boundary:

$$\begin{aligned}
\rho_i^{\mathrm{CS}}(r) &= (\rho_{1,i} * \rho_2)(r) \\
\rho_{1,i}(r) &= \begin{cases} C & r < R_{\mathrm{c},i} \\ 0 & r > R_{\mathrm{c},i} \end{cases} \\
\rho_2(r) &= \exp\left[-\frac{1}{2}\left(\frac{r}{\sigma_{\mathrm{surf}}}\right)^2\right]
\end{aligned} \tag{2.41}$$

Evaluating the convolution to obtain the explicit radial density function is not trivial as convolutions in spherical coordinates must be done carefully [116]. However, the convolution theorem (Eqs. A.5 and A.6) allows $B_i(q)$, which is the Fourier transform of $\rho_i^{\mathrm{CS}}(r)$ into q-space, to be evaluated as the product of the Fourier transforms of $\rho_{1,i}(r)$ and $\rho_{2,i}(r)$:

$$B_i^{\mathrm{CS}}(q) = \frac{C}{2\pi^2}\left(\frac{\sin qR_{\mathrm{c},i} - qR_{\mathrm{c},i}\cos qR_{\mathrm{c},i}}{q^3}\right)\exp\left[-\frac{1}{2}\left(q\sigma_{\mathrm{surf}}\right)^2\right] \tag{2.42}$$

and

$$B_i^{\mathrm{CS}}(0) = \frac{C}{6\pi^2}R_{\mathrm{c},i}^3. \tag{2.43}$$

Then [117]

$$P_i^{\mathrm{CS}}(q) = \left[3\frac{\sin qR_{\mathrm{c},i} - qR_{\mathrm{c},i}\cos qR_{\mathrm{c},i}}{(qR_{\mathrm{c},i})^3}\right]^2 \exp\left[-\left(q\sigma_{\mathrm{surf}}\right)^2\right]. \tag{2.44}$$

It is worth noting that the spherical convolution can be performed analytically and the core-shell radial density function written explicitly:

$$\begin{aligned}
\rho_i^{\mathrm{CS}}(r) = \frac{C}{2}\times\Bigg\{&\frac{2}{\pi}\exp\left[-\frac{1}{2}\left(\frac{r+R_{\mathrm{c},i}}{\sigma_{\mathrm{surf}}}\right)^2\right]\frac{\sigma_{\mathrm{surf}}}{r} + \\
&\left[\mathrm{Erf}\left(\frac{r+R_{\mathrm{c},i}}{\sqrt{2}\sigma_{\mathrm{surf}}}\right) - \mathrm{Erf}\left(\frac{r-R_{\mathrm{c},i}}{\sqrt{2}\sigma_{\mathrm{surf}}}\right)\right]\Bigg\}.
\end{aligned} \tag{2.45}$$

2.5.3 Form Factor Models: Star Polymer

A star polymer is a particle with long polymer chains extending outward from a small core at the center. Unlike the previous cases where the model scattering amplitudes were derived via Eq. 2.29 from a model single-particle radial density function, the model form factor is calculated directly using scaling laws [111]. This is largely because there are no clearly-defined boundaries to the particle, as in the homogeneous sphere case, or distinct regions within the particle, as in the core-shell case. The Guinier decay described in Eq. 2.30 is the dominant effect, giving

$$P_i^{\text{star}}(q) = \exp\left[-\frac{(qR_{g,i})^2}{3}\right]. \tag{2.46}$$

2.6 Light Scattering: Experimental Considerations

In an ideal world, instrument alignment would be perfect and detectors would be completely efficient. In the real world, of course, this is hardly true, and any real experiment must be corrected for any systematic errors introduced by the experimental setup. In this section we discuss several possible sources of error that must be avoided as well as corrections we use in light scattering experiments. Subsection 2.6.1 describes a combination of sample convection and laser interference fringes that is unique to 3DDLS measurements made at high temperature, and must be avoided to obtain meaningful measurements. Subsection 2.6.2 describes corrections due to nonlinear detector response at high count rates. Subsection 2.6.3 describes a correction due to the incident intensity of the laser. Subsection 2.6.4 desribes an intensity correction that must be made due to the nonzero width of the beams. Subsections 2.6.5 and 2.6.6 describe corrections to SLS data for alignment imperfections in the scattering setup and multiple scattering, both of which are applied in one Matlab program. The program also accounts for temperature-dependent variation in the correction factors used, due to thermal expansion or contraction of the apparatus and the associated alignment changes, as discussed in the relevant sections. Finally, Subsection 2.6.7 discusses possible issues when adjusting the pH of ionic microgel suspensions such as the ones used in this study.

2.6.1 3DDLS at High Temperatures: Convection and Interference Fringes

In our 3DDLS experiment, two lasers are crossed in the sample. Although it is not necessary from the perspective of performing a cross-correlation experiment, an interference fringe is formed by the crossed beams as a side effect of the setup. This fringe has been exploited in other methods of particle size determination, such as laser Doppler electrophoresis [118], but in 3DDLS it is actually a liability.

Two beams with wavelength λ, crossed at an angle α, form an interference pattern with fringe spacing $d = \lambda/\sin(\alpha)$. In our DLS setup, $\lambda = \lambda_0/n$, where n is the index of refraction of the sample and λ_0 is the wavelength of the lasers in vacuum. For water, $n = 1.33$, and for our setup, $\alpha \sim 3.44$ °and $\lambda_0 = 632.8$ nm. We therefore estimate that the fringe spacing due to the crossed beams in our setup should be on the order of 10 microns within an aqueous sample; estimating the beam width as about 1 mm, there should be $\gtrsim 100$ fringes vertically across the scattering volume.

If the particles being measured are randomly diffusing, there should be no effect from these fringes on the measured correlation functions. However, at high bath temperatures (above 40–45 °C) there is a substantial temperature gradient, about 1–3 °C, across the height of the cuvette, which is enough to cause convection in the sample if the cuvette is completely filled. Specifically, convection occurs in a liquid if the Rayleigh number, defined as

$$\mathrm{Ra} = \frac{g\beta}{\nu\alpha}\Delta T L^3, \tag{2.47}$$

is above a critical value $\mathrm{Ra_c}$ that depends on the exact geometry and confinement of the liquid, in our case water. Here $g = 9.81$ m/s^2 is the acceleration due to gravity, $\beta(T)$ is the (temperature-dependent) thermal expansion coefficient of the fluid [119], $\nu(T)$ the kinematic viscosity [72, 73], $\alpha(T)$ the thermal diffusivity [120], ΔT the temperature difference between the top and bottom surfaces of the fluid, and L the characteristic length scale of the fluid container, in our case the sample cuvette. Fig. 2.7 shows a schematic of our setup, including the relevant quantities in Eq. 2.47. Taking $T = 45$ °C, $\Delta T = 1$ °C, and a $L \sim 10$ mm, we estimate $\mathrm{Ra} \sim 10^3 - 10^4$. We have no way of predicting the critical Rayleigh number for our

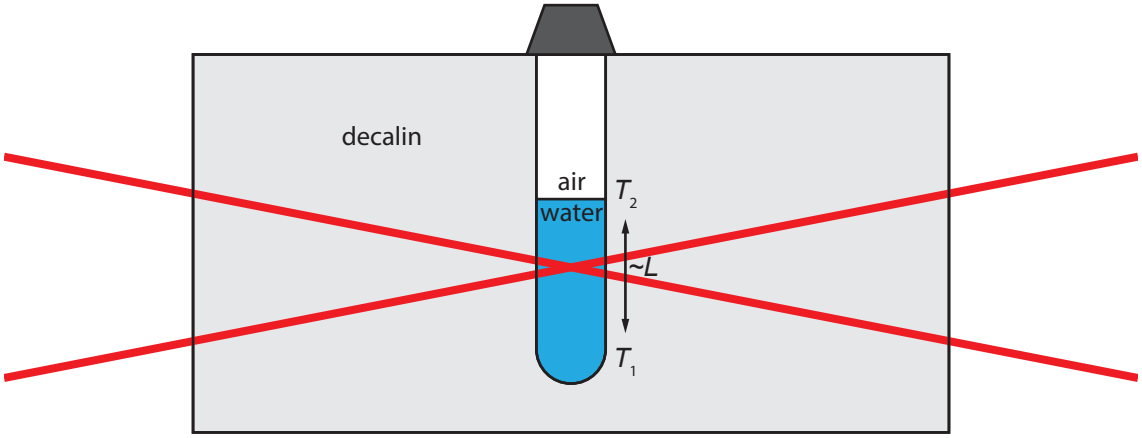

Figure 2.7: A schematic showing the sample cuvette submerged in the temperature bath. Not to scale. The cuvette is partially filled with the sample (blue), predominantly water, with air (white) above. Decalin (gray) surrounds the cuvette. Because of inhomogeneous heating in the decalin bath, a temperature difference $\Delta T = T_2 - T_1$ exists between the top and bottom of the sample.

cuvettes, but $\mathrm{Ra_c} \sim 10^3$ is a rough estimate [121]. It is therefore reasonable to expect that convection will begin in our cuvettes around the higher end of our measured temperature range. We note that L and ΔT are related in our case, since the temperature difference between the liquid surface and the cuvette base is smaller for a less-filled cuvette.

By passing the lasers through a heated cuvette of dusty water, we can observe the convection visually. At these temperatures, we observe dust particles moving through the sample at speeds on the order of a few mm/s. It is not possible to quantify the speed precisely, but we estimate it as 5 mm/s or less. Since the speed due to convection is independent of particle size, the microgels in our experimental system will be moving with the same velocity in addition to their diffusive motion. For particles in a certain size range, the periodicity with which they are driven across the fringe will be comparable to their diffusive timescale.

For intermediate-size particles with diffusive timescale $R_\mathrm{h}^2/D \approx 0.3$ s, we observe such an effect in measurements made at high T. Correlation functions and their corresponding relaxation frequencies are shown in Fig. 2.8 for microgels at intermediate pH, thus partially

swollen. Note the oscillatory component that appears in the correlation functions at higher temperatures in panel a, corresponding to a breakdown in the reliability of the measurements as seen in panel b. There, we see that not only is the trend of increasing Γ (decreasing particle size) with increasing temperature lost, but a given measurement is not reproducible.

The peaks of this oscillation are uniformly spaced about 0.003 s apart, depending slightly on the temperature; the velocity obtained by multiplying the fringe spacing by the frequency is about 3 mm/s, in agreement with what we observe for dust particles in the bath at these temperatures. Further, these effects do not show up in an autocorrelation experiment on the same system, confirming that it is the beam crossing that is responsible. For larger or smaller particles, the characteristic diffusion time is either significantly higher or lower than the characteristic time for the particles to move through the fringes, decoupling the two effects and allowing us to determine the diffusion coefficient normally.

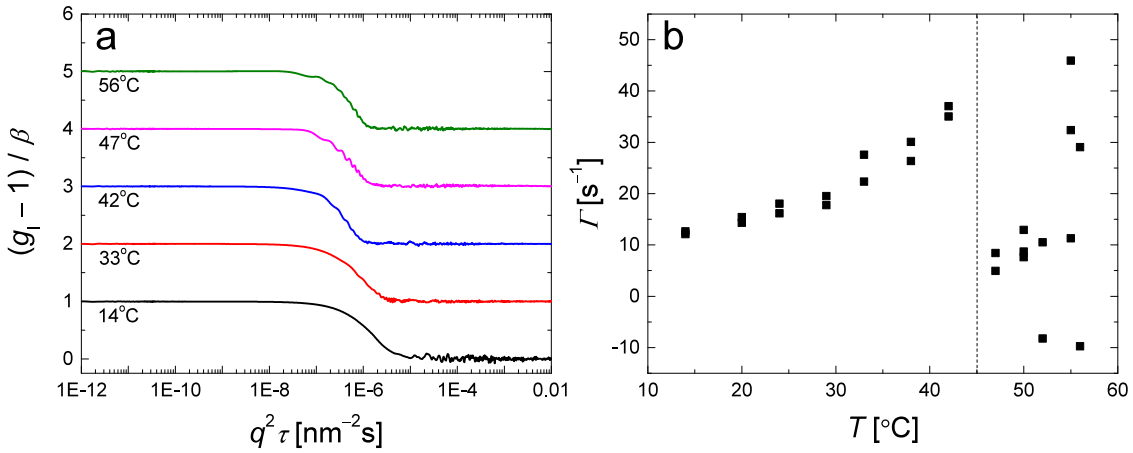

Figure 2.8: (a) Correlation functions measured for a particle of $R \sim 500$ nm as a function of $q^2\tau$ for various temperatures. They have been offset vertically for clarity. (b) Relaxation frequencies obtained from such correlation functions as a function of temperature. For $T \lesssim 43$ °C, the correlation functions appear normal and Γ increases with temperature, as expected. For $T \gtrsim 43$ °C, oscillations appear in the correlation functions and the apparent Γ undergoes an abrupt change to random, noisy values.

For SLS measurements, the 3DDLS measurements are necessary for most conditions to remove multiple scattering from the observed intensity, as discussed in Subsection 2.6.6. However, we perform autocorrelation experiments separately to obtain values of R_h at conditions where convection occurred and where its timescale overlapped with the diffusive

timescale of the particles. Convection can also be avoided by using a very small sample volume, such that the height of the sample is small enough that the temperature difference from top to bottom is small enough for convection not to occur. In these cases we use a sample volume of 0.5 mL, which is the minimum possible due to the curved bottom of the cuvettes. The lasers must not pass through the curved region en route to the scattering volume in order to maintain the necessary alignment; similarly, they must avoid the meniscus at the top of the sample. 0.5 mL of sample is enough that the lower laser just barely enters above the curved area, and the upper laser just barely enters below the meniscus.

2.6.2 Nonlinearity of the Detectors

Our SLS measurements must be corrected for nonlinear effects of the detectors. All photodetectors have a characteristic recovery or "dead" time, τ_{dead}. After detecting a photon, the detector is insensitive to additional photons for an amount of time equal to τ_{dead}, and any photons received before the detector has recovered are ignored. If I_0, the scattered intensity incident onto the detector, is small enough, then the frequency with which photons strike the detector will be less than $1/\tau_{\text{dead}}$, and, on average, photons will not strike the detector during its interval of blindness. If, however, I_0 is high enough, a significant number of photons will strike the detector during the recovery period, which has two effects—worsening statistics, and wrong intensity profiles. For some detectors, called "paralyzable" detectors, the dead time is reset if a photon strikes the detector before it recovers—thus, if I_0 is high enough, the detector registers nothing. Our detectors are non-paralyzable, meaning that their recovery time is unaffected by the number of incident photons. For a non-paralyzable detector, the measured count rate CR is given by [122]:

$$CR = \frac{CR_0}{1 + CR_0\tau_{\text{dead}}}, \tag{2.48}$$

where CR_0 is the count rate that would be measured by an ideal detector with $\tau_{\text{dead}} = 0$. If we know τ_{dead}, we can correct for this effect to obtain CR_0 from CR. Eq. 2.48 can be rewritten to show the limitation of this correction:

$$CR_0 = CR\frac{1/\tau_{\text{dead}}}{1/\tau_{\text{dead}} - CR}. \tag{2.49}$$

Since $\frac{1/\tau_{\text{dead}}}{1/\tau_{\text{dead}}-CR} < 1$, a nonzero dead time always acts to decrease the measured count rate. However, CR need not be less than $1/\tau_{\text{dead}}$, as the intensity of the laser can be turned up arbitrarily high. If $CR > 1/\tau_{\text{dead}}$, no correction can be made: since the detector is completely saturated, it is unable to tell the difference between any count rates higher than $1/\tau_{\text{dead}}$. Maintaining $CR < 1/\tau_{\text{dead}}$, Eq. 2.48 can be Taylor expanded around $\tau_{\text{dead}} = 0$:

$$CR = CR_0 - CR_0^2\tau_{\text{dead}} + ... \tag{2.50}$$

Considering that $CR_0 \propto I_0$, Eq. 2.50 is equivalent to

$$CR = \kappa I_0 - \kappa^2 I_0^2 \tau_{\text{dead}} + ..., \tag{2.51}$$

with κ an angle-dependent constant of proportionality between CR_0 and I_0. An ideal detector would have only the linear term.

We record the measured angular intensity profile of a dilute, singly-scattering, suspension of colloidal polystyrene beads in water ($R = 100$ nm), repeating the measurement for many different I_0. Holding I_0 constant and measuring with angle gives the intensity profiles shown in Fig. 2.11a. The intensity not only scales vertically with I_0, but shows nonlinearity artifacts at low q, where the scattered intensity is highest. For a given angle, CR is proportional to I_0 for low enough I_0. However, for high enough I_0 that nonlinear effects become important, this is no longer true, as shown in Fig. 2.9.

Since there are two detectors (A and B), two corrections are necessary—the detectors' alignment is not identical and so the measured count rates, CR_{A} and CR_{B}, for the two detectors are different for a given angle and I_0. We use the freely-available Imtek Interpolation package for Mathematica to fit a spline surface to the data, following Eq. 2.51. These fits are shown in Fig. 2.9. The non-ideal nature of the detectors can be seen from the fact that the fitting surfaces are not linear in I_0 for a constant angle.

To obtain the best correction, we compare fits to constant-angle slices of the interpolation surface with linear, quadratic, cubic, quintic, and tenth-order polynomials in I_0. The linear term for polynomial fits of order higher than 2 is not a smooth function of angle, as shown in Fig. 2.10, so we truncate Eq. 2.51 to second order, allowing us to obtain τ_{dead} for each

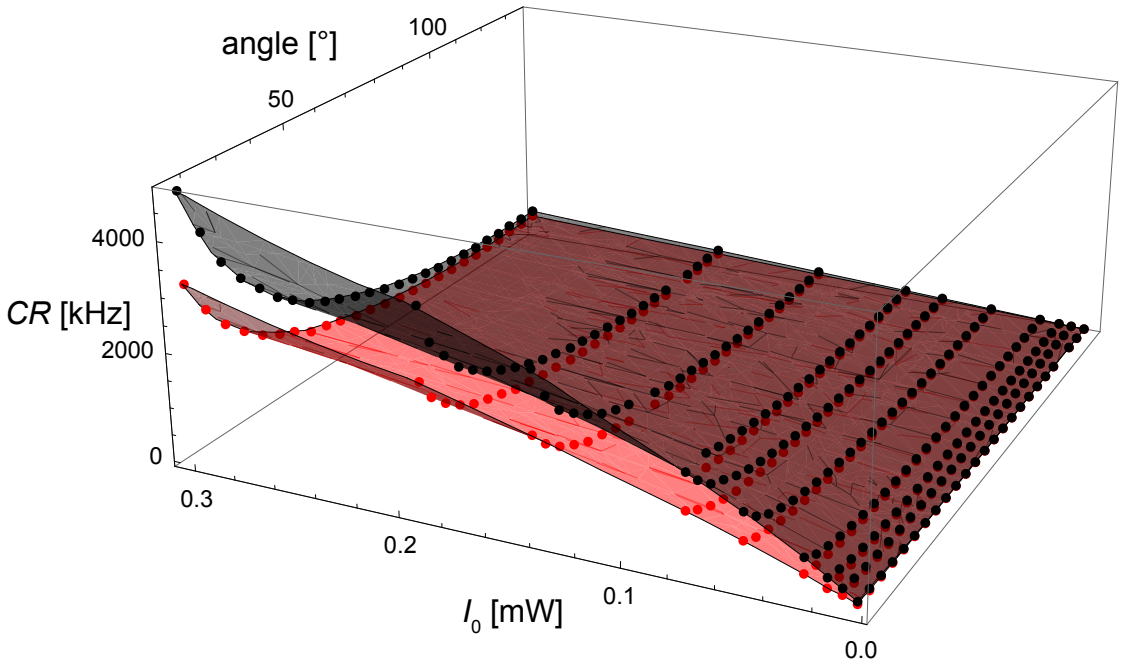

Figure 2.9: The points represent the measured count rates as a function of angle for different incident intensities, and the surfaces are spline fits. Black is for detector A and red is for detector B. The mean error of the fitting is $< 1\%$.

detector. Further, since I_0 is known, and at low I_0 the linear term dominates, this allows us to determine κ as well. We obtain $\tau_{\text{dead,A}} = 5.05 \times 10^{-8}$ s and $\tau_{\text{dead,B}} = 6.17 \times 10^{-8}$ s, close to but above the manufacturer's stated t_{dead} of 3.2×10^{-8}. Using these values, we are able to recover the actual intensity, as shown in Fig. 2.11a, b, and e. In panel a, we show the measured intensity without correcting the nonlinear effects, which are visible at low scattering angles where the scattered intensity is highest. For low I_0, $CR = CR_0$. As I_0 increases, more and more of the scattered photons strike the detector within one dead time of the previous photon and are not detected, causing a significant decrease in measured intensity. Panel b shows the same data after correction. Note that the highest I_0 cannot be corrected for completely; this is because the second-order correction in Eq. 2.51 is no longer sufficient to account for all nonlinear effects at this point. As shown in Fig. 2.10 however, accounting for these higher-order contributions cannot be done reliably. As a practical matter, we find that restricting I_0 such that $CR_0 < 2.5 \times 10^3$ kHz allows us to fully correct for the nonlinear effect. Panel e shows an example correction: black $\times$'s are

uncorrected and red +'s are corrected data, together with the theoretically expected $P(q)$. The figure makes it clear that neglecting the nonlinearity correction makes proper fitting of SLS data impossible.

The DLS correlation function, and in particular its intercept, is affected by nonlinearities as well. A dead-time-affected autocorrelation function with $g_{\mathrm{E}} \to 1$ is written as [123]

$$g_{\mathrm{I}} = \frac{1+\beta}{1+2\epsilon\beta}\left(\frac{1+2\epsilon\beta}{(1+\epsilon\beta)^2}\right)^{-(1+\beta)/\beta} = 1+\beta^*, \tag{2.52}$$

where $\epsilon = CR_0\tau_{\mathrm{dead}}$, β^* is the observed intercept, and β is the value that the intercept would have if it were unaffected by detector nonlinearity. Since β^* is a measured quantity and we know ϵ, β can be obtained from Eq. 2.52. This equation was derived for an autocorrelation measurement, and is not rigorously correct for a cross-correlation measurement, for which the equivalent correction has not been derived. However, we find that this correction does recover the low-I_0 value of β from high-I_0 measurements, as shown in Fig. 2.11c and d. For our cross-correlation measurements, therefore, we use Eq. 2.52 with the geometric mean of the two measured dead times in ϵ.

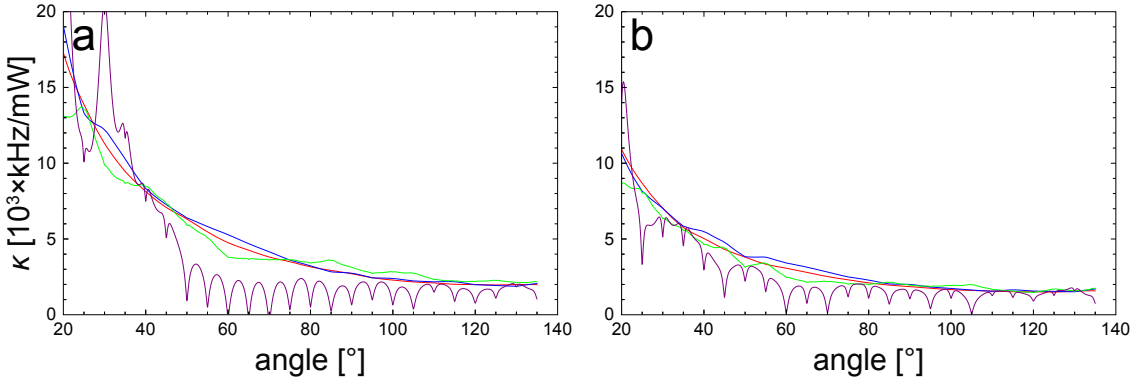

Figure 2.10: Coefficients for detectors (a) A and (b) B. The terms linear in I_0 for fits to the interpolation surface with Eq. 2.51: a quadratic fit (red), cubic fit (blue), quintic fit (green), and 10th-order fit (purple), as functions of angle. The 10th-order fit in particular contains artifacts from the spacing of the data. Actual data points are every 5°.

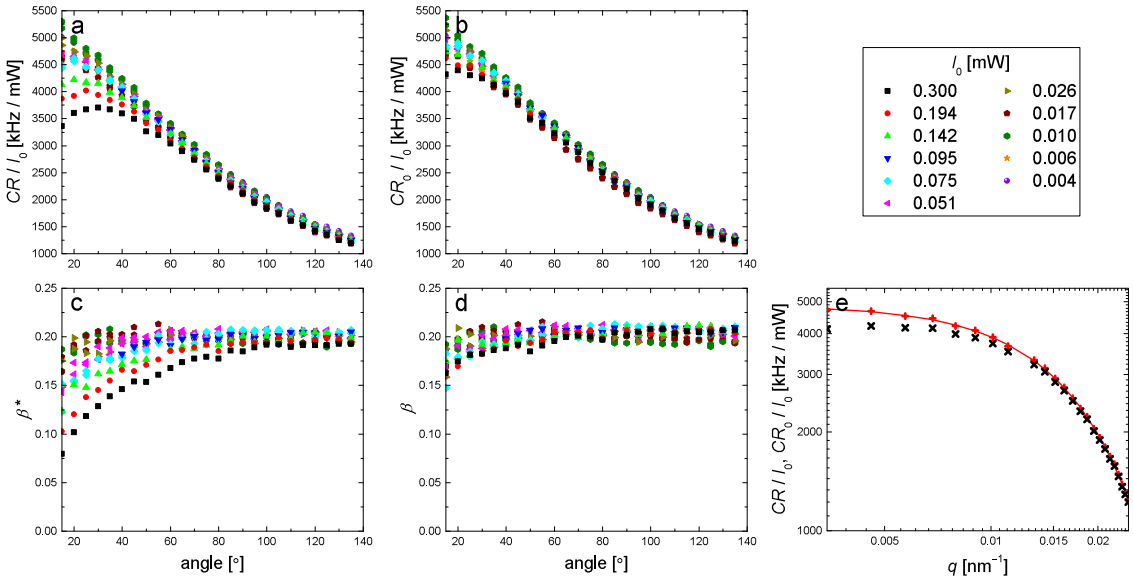

Figure 2.11: (a) Uncorrected and (b) corrected intensity profiles measured for a variety of initial intensities. Note that at exceptionally high incident intensities, the correction procedure cannot fully recover the true incident intensity. (c) Uncorrected and (d) corrected intercepts for the same measurements. (The lowest-incident-intensity measurements are not included in the intercept graphs because the measured intercepts were exceptionally low; this was due to the extremely low incident intensity, which effectively reduced the signal-to-noise ratio, and was not due to nonlinear effects of the detectors.) (e) An example correction. The measured intensity data (black squares) and corrected data (red circles) are shown along with the theoretically expected fit (red line, Eq. 2.40) for scattering from a sample of polystyrene spheres of radius 100 nm.

2.6.3 Baseline Intensity Corrections

The intensity scattered by the sample is proportional to the incident beam intensity, I_0. For many samples, $I(q)$ can decay by factors of 10^3 or more for an increase in q of only O(10%). An SLS measurement of such a sample over the entire q range requires that I_0 be periodically increased. In order to correct for the resulting change to the scattered intensity, after applying the previous corrections, we divide $I(q)$ by I_0 to obtain the number of scattered photons per incident photon for a given q value.

2.6.4 Angular Dependence of the Projection of the Scattering Volume

The detector alignment and a series of pinholes ensure that only light from the desired scattering volume, the region of overlap between the beams, is scattered into the detectors. Because of the finite thickness of the lasers, this region of overlap has a nonzero volume, shown in Fig. 2.12. The intensity scattered at lower angles is higher than at higher angles,

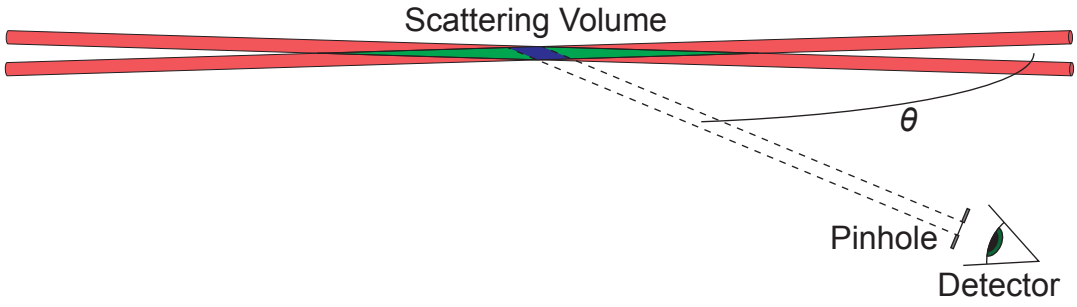

Figure 2.12: A schematic showing the angular dependence of the observed portion of the scattering volume. The crossed beams are shown in red; the green region represents the total scattering volume; and the blue region, the region observed by the detectors.

independent of the scattering of the sample, because the thickness of the scattering volume observed by the detector is higher at low θ. The dependence goes approximately as $1/\sin(\theta)$ [124]. To correct for this, we multiply the observed intensity by $\sin(\theta)$, where θ is the scattering angle.

2.6.5 Alignment Corrections

Scattered intensity should not change as a function of scattering angle for an isotropic scatterer. However, experimentally, we find that there is a small dependence, due to alignment imperfections, that will also cause systematic errors in the measured intensity for an anisotropic scatterer. We correct the measured intensity as follows:

$$I_{\text{corrected}}(\theta) = \frac{\langle I_{\text{ref}} \rangle_\theta}{I_{\text{ref}}(\theta)} I_{\text{measured}}(\theta). \tag{2.53}$$

Here, $I_{\text{ref}}(\theta)$ is the intensity scattered by an isotropic scatterer as a function of scattering angle, and $\langle I_{\text{ref}} \rangle_\theta$ is its angular average. Generally, the correction factor is within 5% or so of 1; considering that intensity is usually plotted as a logarithm, the effect of this correction is comparatively quite small.

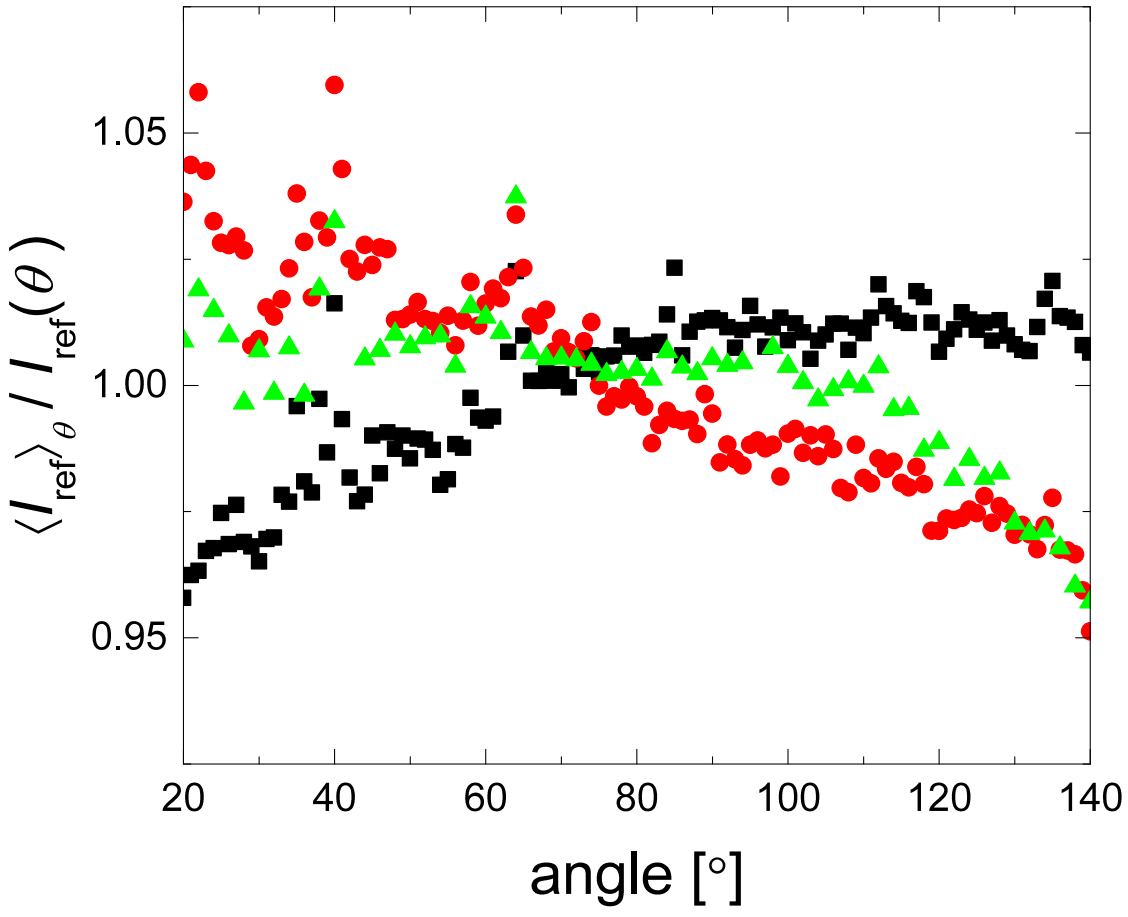

Figure 2.13: Alignment correction factors measured for $T = 13.6 \pm 0.11$ °C (black squares), $T = 31.0 \pm 0.24$ °C (red circles), and $T = 59.8 \pm 0.5$ °C (green triangles).

Due to the thermal expansion of its glass and metal components, the alignment imperfections of the instrument change with temperature, sometimes rather significantly. This is a separate temperature effect from the convection discussed in Subsection 2.6.1. In order to compensate for this, we measure alignment factors at 13.6, 31.0, and 59.8 °C, shown in Fig. 2.13. We linearly interpolate for temperatures in between any two of the reference temperatures. For measurements made outside of these windows we fix the correction factor to the near extremum.

2.6.6 Multiple Scattering

We correct for multiple scattering using Eq. 2.15 and a reference intercept measured from a polystyrene standard. Experimentally, we find temperature dependence in β^{ref} obtained from these measurements. Because the reference suspension itself is not temperature-sensitive, this must be due to changes in the alignment caused by thermal expansion, as discussed also at the end of Subsection 2.6.5. In order to compensate for this, we measure angle-dependent intercepts for six separate temperatures, shown in Fig. 2.14a. We linearly interpolate to estimate the intercept in between any two of the reference temperatures. For measurements made outside of these windows we fix the correction factor to the near extremum.

Multiple scattering is usually assumed to occur only in concentrated samples, but this is not necessarily true. Multiple scattering can significantly contribute to measurments even in dilute samples that are transparent to the eye. If the q-range of the experiment includes form factor minima, like those shown in Fig. 2.6, very little single-scattered light will be scattered into the angles corresponding to those minima. Multiple scattering which is negligible at other q will dominate the measured intensity at those angles, artificially "filling" them in, and must be corrected for. Fig. 2.14b shows an example of this. The red points, corresponding to the right-hand y-axis, show the angular dependence of β, with minima corresponding to those of $P(q)$. When β is relatively large, the factor β/β^{ref} is close to 1 and there is little contribution from multiple scattering. This is reflected in the close match between the true $P(q)$, shown by filled squares, and the normalized measured

intensity, shown by open squares, in these regions. However, near the minima of $P(q)$ and β, the correction is significant because a larger fraction of the measured photons are multiply-scattered. The main effect due to the correction is therefore a deepening of the minima.

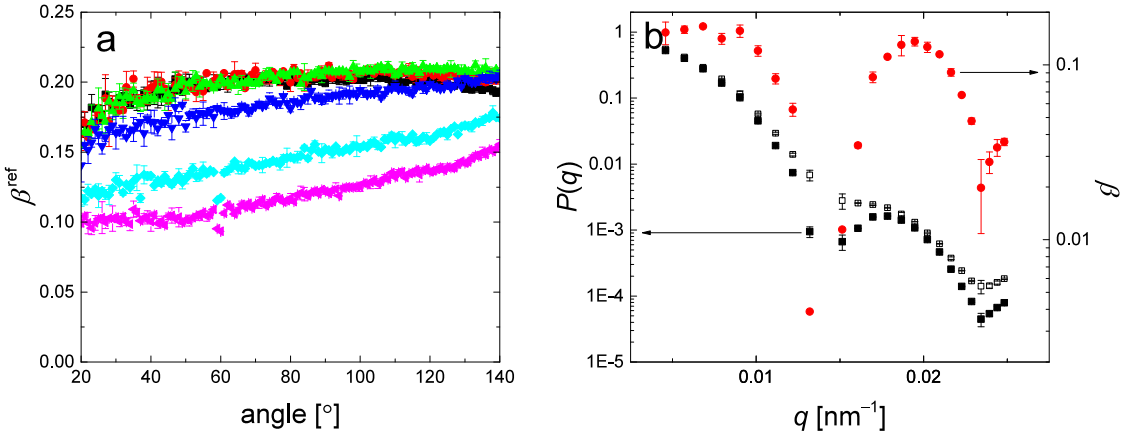

Figure 2.14: (a) Reference intercepts measured at $T = 13.8$ °C (black squares), $T = 19.7$ °C (red circles), $T = 28.8$ °C (green upward triangles), $T = 39.9$ °C (blue downward triangles), $T = 49.9$ °C (cyan diamonds), and $T = 60.7$ °C (magenta leftward triangles). Error bars are taken to be the standard deviation of a set of multiple measurements at each scattering angle. (b) The multiple-scattered intensity contribution for a dilute sample. The measured intercept, shown in red, clearly follows the minima of the form factor, shown in black. Hollow black squares represent the raw form factor, uncorrected for multiple scattering; filled squares, the form factor after correction.

2.6.7 pH Adjustment

For pH-dependent samples, it is important to account for anything that could inadvertently change the pH. Initially in our experiments, we inexplicably found that low-pH solutions would increase significantly in pH after several hours in a glass cuvette. Eventually we found that this was due to the type of glass used; as several other researchers had discovered, flint glass cuvettes are contaminated with alkali residues leftover from the manufacturing process [125]. We switched to borosilicate glass cuvettes, and have since found that the pH of suspensions stored in these cuvettes has not measurably changed over several years.

We also account for the influence of ions, introduced by pH adjustment, on the swelling behavior of the particles in suspension. We adjust pH upward with NaOH, and downward with HCl. Adding equal amounts of NaOH and HCl to the sample has the same end result

as adding salt water. The presence of electrolytic ions in the solvent tends to screen charges from the ionized AAc groups in the polymer at higher pH, and thus must be accounted for.

This effect occurs when the salt concentration in the system increases to the order of the charge concentration in the microgels [50, 126]. At low pH, the AAc groups in our microgels are neutral, and there should be no salt effects, although we are careful nevertheless to only add as much HCl as needed to reach the desired pH. In the case when the AAc groups are partially or completely ionized, we can estimate the charge density inside the microgels and compare it to the added salt concentration.

We can estimate the number density of AAc groups in charged microgels via two methods: (i) using the mass–volume relationship established from viscometry in Section 2.3, and (ii) the estimated size of a completely deswollen microgel. Both of these methods make use of measurements of the hydrodynamic radius, R_h, from light scattering in Section 2.7.

(i) Using the k values obtained from viscometry (Section 2.3) and the hydrodynamic radius R_h from dynamic light scattering (Section 2.7) we estimate k for our microgels at the desired conditions. From the definition of volume fraction, $\phi = kc = Nv^\mathrm{1P}/V$; we consider a single microgel by setting $V = v^\mathrm{1P}$ and $N = 1$, giving $1/k = c$. Rearranging the concentration to solve for the mass of polymer in a single microgel gives $m_\mathrm{p} = m_\mathrm{solvent}/(100\% \times k - 1)$. Approximating the density of the microgel as that of the solvent, in our case water, gives that the polymer mass per volume of the swollen particle follows $m_\mathrm{p} = \rho_\mathrm{water} v^\mathrm{P}/(100\% \times k - 1)$. The synthesis includes 73 mol% NIPAM, 24 mol% AAc, and 3 mol% pEG-d, and the molar masses of these monomers are 113 g/mol, 72 g/mol, and 587 g/mol, respectively. With $m_\mathrm{p} = n_\mathrm{NIPAM} m_\mathrm{NIPAM} + n_\mathrm{AAc} m_\mathrm{AAc} + n_\mathrm{pEG\text{-}d} m_\mathrm{pEG\text{-}d}$, where n_i is the number of moles and m_i the molar mass of component i, we can obtain an expression for the total number of moles of AAc per particle in terms of R_h and k: $n_\mathrm{AAc} = 4.2 \times 10^{-21} R_\mathrm{h}^3/(100\% \times k - 1)$, with R_h the hydrodynamic radius in nm and k in inverse wt%. Because we have several measured values for k and R_h, obtained at different T and pH as discussed in Sections 2.3 and 2.7, we can compare the results obtained to be sure we have an accurate value for n_AAc. Averaging these results obtained from different conditions and taking the standard

deviation as the error, we find that $n_{\mathrm{AAc}} = (8.61 \pm 0.22) \times 10^{-17}$ moles per particle; equivalently, there are $N_{\mathrm{AAc}} = (5.18 \pm 0.13) \times 10^{7}$ AAc monomers per particle.

(ii) First, we estimate the number of monomers in one microgel. The amount of bound water in a deswollen pNIPAM microgel is about 0.39 ± 0.01 g of water per 1 g of polymer [127]. From Fig. 2.15, we estimate that $R_{\mathrm{h}} = 145 \pm 10$ nm for pH 3 and $T = 60$ °C, when the AAc is uncharged and the particle should be approximately as deswollen as a pNIPAM microgel. Given that the density of dry pNIPAM is 1.1 g/cm^3 [128], and using this as the approximate density of dry pAAc and pEG-d, we can estimate the radius of a dry (completely deswollen, often referred to as "collapsed") microgel as $R_{\mathrm{dry}} = 129 \pm 9$ nm. We divide the volume of the dry microgel by the approximate volume of one monomer, $v_{\mathrm{monomer}} \approx 0.016$ nm^3, estimated by cubing the linear dimension of one monomer in a chain, ~ 0.25 nm. (Because NIPAM, AAc, and pEG-d all contribute two carbon-carbon bonds to the backbone of the polymer chain, the volume contributed by each one should be similar.) This gives approximately $(5.7 \pm 1.2) \times 10^{8}$ monomers in one microgel. 24% of these, or $(1.4 \pm 0.3) \times 10^{8}$, are AAc monomers.

Both methods give values that are comparable, given that the comparison is based on values obtained by two independent means, each with a corresponding experimental error. We take the number of AAc to be the average of these two values, giving $N_{\mathrm{AAc}} = (1.1 \pm 0.6) \times 10^{8}$.

In the extreme case, where all of these AAc momoners are charged, this corresponds to a molarity of about 0.038 M of charge. Considering that adding an equivalent molarity of sodium would require adding enough NaOH to go from pH 1 to 12, and that salt effects will be weaker for systems that are not fully charged, it is highly unlikely that any pH adjustments we make will cause salt concentration effects in our particle swelling behavior. Nevertheless, we were careful in our pH adjustments to only add the minimum of NaOH or HCl necessary, and not overshoot and have to readjust.

2.7 Experimental Characterization of Our Microgels

First, we measure the hydrodynamic radius of our microgels as discussed in Section 2.4. Because they swell and deswell as a function of both temperature and pH, we perform measurements (i) at several fixed temperatures for many different pHs and (ii) at several fixed pHs over many different temperatures. In the former case, we choose $T = 14$ °C, $T = 29$ °C, and $T = 58$ °C, which are far below, slightly below, and far above the LCST, respectively. In the latter case, we choose pH 3.1, pH 5.0, pH 5.7, and pH 6.5. At pH 3.1, the AAc inside the microgel is neutral; at pH 5.0 and 5.7, it is partially ionized; and at pH 6.5 and higher, it is completely ionized. Our results are shown in Fig. 2.15.

We see that, as expected, R_h is larger at lower temperatures, due to the fact that the pNIPAM segments in the polymer are uncoiled, tending to swell the microgels. Similarly, at higher pH, the ionized AAc draws in counterions from the solvent, also leading to a larger R_h, and a plateau is reached for $pH \gtrsim 6.5$. However, there is clearly some competition between these two mechanisms: for example, the typical deswelling behavior of pNIPAM with increasing T is visible only for the lowest-pH sample, as shown with the black squares in Fig. 2.15b. We do note that the deswelling is more gradual than observed in pure pNIPAM polymer, perhaps due to the presence of hydrophilic pEG-d crosslinker. Additionally, at around pH 5, there is no clear change in R_h as a function of T. R_h clearly continues to increase as pH is raised, and at higher pH the low- and high-T curves once again separate. This could mean that the microgels' internal structure, but not overall hydrodynamic size, change as a function of T at pH 5, or that the swelling due to partial ionization is able to counteract the LCST-driven deswelling at that pH.

We perform SLS experiments simultaneously with the above dynamic measurements, using the intercept acquired from the 3DDLS experiments to remove the multiple-scattered contribution to intensity as discussed in Section 2.5. This gives us a picture of the way $P(q)$ evolves as a function of changing T and pH. These results are shown in Fig. 2.16.

At pH 3.1, Fig. 2.16a, when the microgels are neutral, the experimental form factors are well-fitted by the core-shell model, Eqs. 2.35 and 2.44, which is typical for pNIPAM microgels in the absence of AAc [117]. At the lowest temperatures, where the microgels

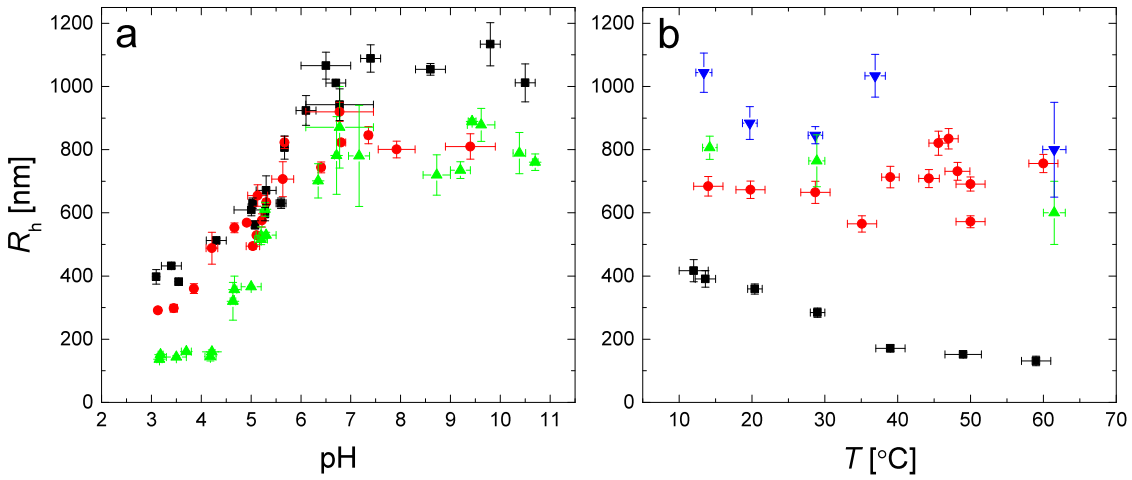

Figure 2.15: (a) R_h as a function of pH for $T = 14 \pm 1$ °C (black squares), $T = 29 \pm 1$ °C (red circles), and $T = 58 \pm 3$ °C (green triangles). (b) R_h as a function of T for pH = 3.1 (black squares), pH = 5.0 (red circles), pH = 5.7 (green upward triangles), and pH = 6.5 (blue downward triangles).

are most swollen for that pH, a second minimum in $P(q)$ is visible. In order to properly fit this second minimum with Eq. 2.35, the network term must have $\mu = 2$, i.e. Debye-Bueche scaling, because for lower values of μ the decay of the network term is too slow and washes the minimum out; without the inclusion of the network term, the model places the minimum a factor of about 5 too low. The fuzzy shell described by σ_surf in the model decreases markedly at higher temperatures, leading to a sharper increase in $P(q)$ after the first minimum. In that case, $P(q)$ appears to approach that of a homogeneous sphere, described by Eq. 2.40, although as we will show in Chapter III, this does not hold true at smaller length scales.

At pH 5.0, Fig. 2.16b, the microgels are partially ionized. Here the model that best fits the data depends on the temperature: at lower temperatures, $T \lesssim 44.3$ °C, the core-shell model fits best, while at higher temperatures it fails and we use the star polymer model, Eqs. 2.35 and 2.46, instead. The fact that the high-q experimental data rises vertically with temperature indicates that the network term's contribution to $P(q)$ is increasingly important at higher T.

Finally, at pHs 5.7 and particularly 6.5, Fig. 2.16c and d, respectively, we approach an apparently temperature-independent state. Here, the core-shell model fails completely, and

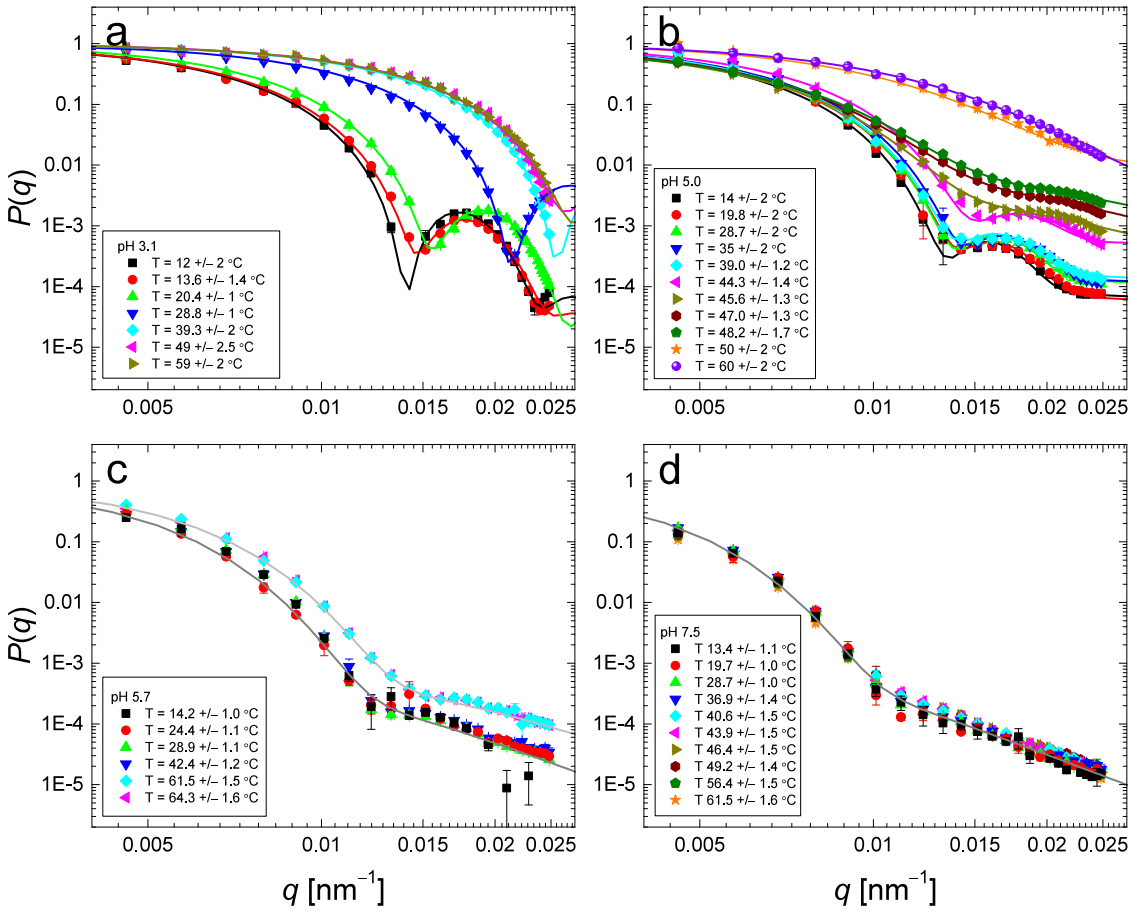

Figure 2.16: Experimental $P(q)$ for different T and pH. (a) pH 3.1: lines are fits to the core-shell model, Eqs. 2.35 and 2.44. The network term must follow the Debye-Bueche law ($\mu = 2$) in order to correctly fit the second minimum which is visible at low temperatures. (b) pH 5.0: lines are fits to the core-shell model for $T \leqslant 44.3$ °C, and to the star polymer model, Eqs. 2.35 and 2.46, for higher temperatures. (c) pH 5.7: the data are separated into two slightly different regions based on temperature. Lines are fits to the star polymer model, with all the measurements for each temperature region being averaged and fitted together. (d) The data overlap within the mesaurement uncertainty, and are all fitted by a single application of the star polymer model.

we replace it by the star polymer model. We note that the microgels cannot be true star polymers, simply because of the large amount of crosslinker included, but they apparently share a similar mass distribution, as evinced by the excellent match between data and model shown in the figure. The apparent independence of $P(q)$ from T is at first glance somewhat surprising, given that in Fig. 2.15 we see a slight decrease of $R_{\rm h}$ at higher temperatures even at high pH. This is likely due to the presence of a few dangling chains at the periphery at low T which contribute to drag, and therefore to a larger $R_{\rm h}$, but scatter so little that they are invisible to SLS. However, at high T, the chains may contract due to pNIPAM's deswelling, slightly decreasing $R_{\rm h}$: because they are not on the interior of the microgel, they are not swollen by the AAc contribution at high pH.

Aside from fitting the full range of experimental data, we also fit the Guinier regime to obtain $R_{\rm g}$. In order to do this, we begin by fitting the first three points of the experimental $P(q)$ to Eq. 2.30 to obtain a value for $R_{\rm g}$. We then multiply this $R_{\rm g}$ by the q value of the highest-q point used in the fit. If the result is $qR_{\rm g} \leqslant 2.5$, we repeat the process for the first four points, then five, and so on, until we have the fit that includes the most allowed points. We take the value of $R_{\rm g}$ from that particular fit. Plots of $R_{\rm g}$ vs. T for pHs 3.1, 5.0, 5.7, and 6.5 are shown in Fig. 2.17.

While for pHs 3.1, 5.7, and 6.5, the temperature-dependence is consistent with that of $R_{\rm h}$ in Fig. 2.15, at pH 5.0 we see a markedly different behavior. Unlike $R_{\rm h}$, $R_{\rm g}$ shows a clear decrease at higher temperatures, although the transition occurs at higher T than at pH 3.1. This is consistent, however, with Fig. 2.16b, in which we see an evolution of $P(q)$ with increasing T. Note that as discussed in the derivation of Eq. 2.30, obtaining $R_{\rm g}$ is independent of the details of $P(q)$, and thus is not caused by differences in the model used. We will discuss this contradiction in more detail in Chapter IV.

Finally, we plot the fitting parameters used with the core-shell model to obtain the lines shown in Figs. 2.16a and b. Polydispersity values obtained from the fits are listed in Table 2.1. Fits to the star polymer model are determined by the same $R_{\rm g}$ obtained from the Guinier fit. Figs. 2.18a and b show the core-shell fitting parameters $\langle R_{\rm c}\rangle$, $2\sigma_{\rm surf}$, and the total particle size, $R_{\rm SLS} = \langle R_{\rm c}\rangle + 2\sigma_{\rm surf}$, for pH 3.1 and 5.0, respectively. For comparison

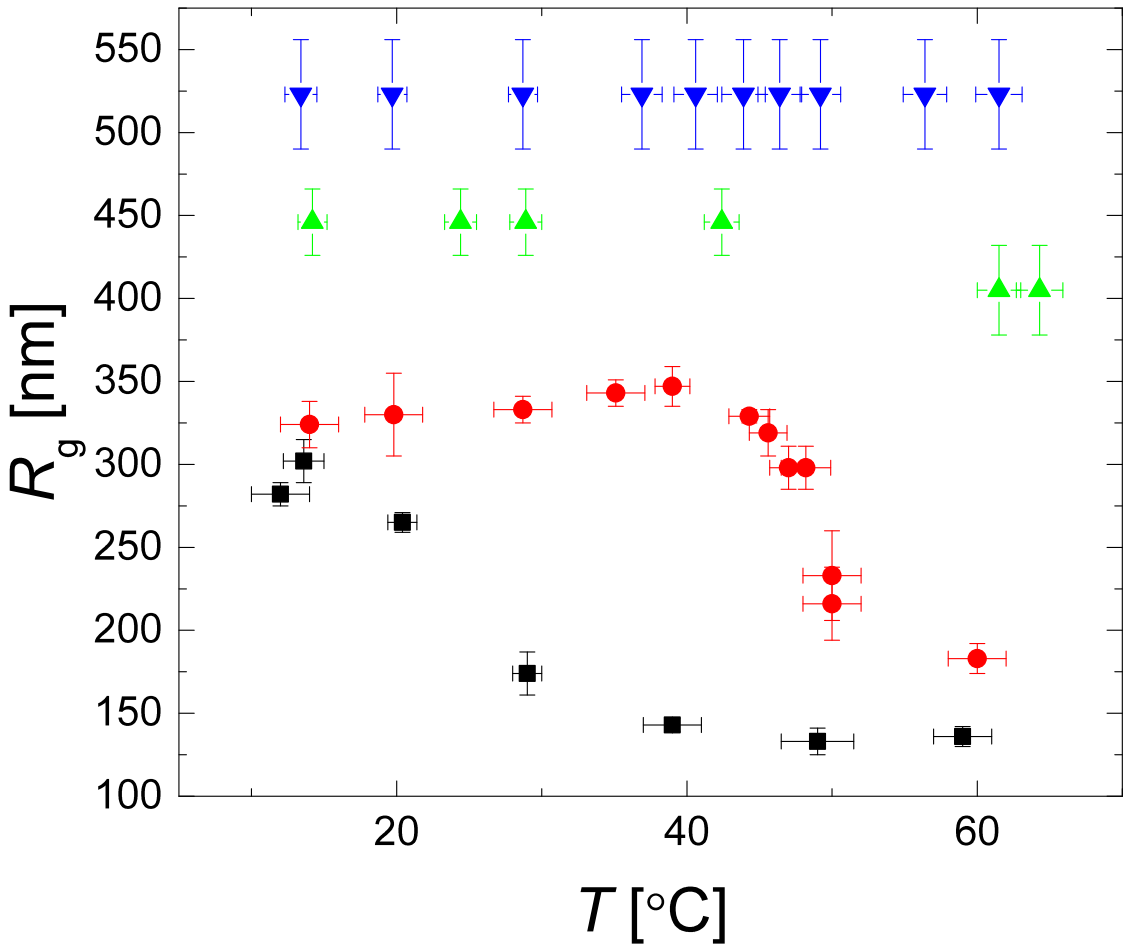

Figure 2.17: R_g as a function of T for pH = 3.1 (black squares), pH = 5.0 (red circles), pH = 5.7 (green upward triangles), and pH = 6.5 (blue downward triangles).

purposes, we include parameters from core-shell fits made at the high-T region of the pH 5.0 sample, $T \geqslant 44.3$ °C, even though that model does not adequately fit the data there. As a result, while the parameters for the pH 3.1 sample show the expected behavior (deswelling and a near-total disappearance of the fuzzy shell), the pH 5.0 sample's high-T points are more difficult to interpret. R_{SLS}, decreases smoothly, but the fitted core size and shell thickness do not, although we emphasize that this is likely due more to a failure of the model than anything else.

2.8 Conclusions

The chemistry of our microgels is new in two ways —first, they contain pEG-d as a crosslinker, which is unusual and provides a possible hydrophilic contribution to swelling;

Table 2.1: σ_{p} obtained from fits to $P(q)$ for samples measured at various T and pH. For pH 3.1 and pH 5, $T \leqslant 44.3$ °C, fits are performed with the core-shell model, Eqs. 2.35 and 2.44. For other conditions, the star-polymer-like model, Eqs. 2.35 and 2.46, are used instead.

pH	T [°C]	σ_{p}
3.1	12 ± 2	1.5 ± 1.4
	13.6 ± 1.4	4.8 ± 1.0
	20 ± 1	4.7 ± 0.3
	29 ± 1	1.5 ± 1.4
	39 ± 2	2.5 ± 2.4
	49 ± 3	0.75 ± 0.65
	59 ± 2	0.76 ± 0.66
5.0	14 ± 2	6.5 ± 1.5
	20 ± 2	7.3 ± 0.8
	29 ± 2	6.3 ± 1.0
	35 ± 2	7.0 ± 1.0
	39.0 ± 1.2	7.4 ± 1.0
	44.3 ± 1.4	8.9 ± 1.0
	45.6 ± 1.3	6.5 ± 6.4
	47 ± 1	7.5 ± 7.4
	48.2 ± 1.7	13 ± 6
	50 ± 2	23 ± 5
	60 ± 2	23 ± 1
5.7	all	5 ± 5
6.5	all	5 ± 5

and second, the amount of AAc included in these particles is much higher than in any previous study. We have characterized their dilute properties in great detail to ensure that we properly understand our observations at higher concentrations. We outlined the microgel synthesis, highlighting differences from commonly-encountered microgels in the literature. We then performed viscometry on the particles in order to determine a relationship between their mass and occupied volume under different conditions, and verified our results for different T and pH. We introduced both dynamic and static light scattering of colloidal particles with detailed theoretical derivations and an exhaustive catalog of experimental considerations that must be corrected for to obtain meaningful data, and obtained the hydrodynamic radius, R_{h}, and the radius of gyration, R_{g}. We also developed models used to describe the scattering form factor, $P(q)$, and discussed the complementary length scales

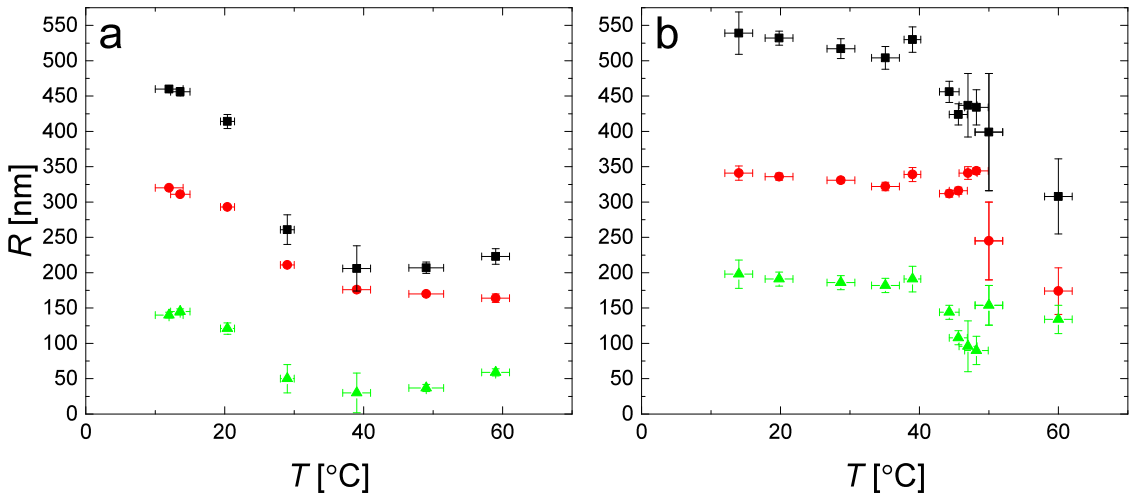

Figure 2.18: Core-shell fitting parameters for the particles at pH (a) 3 and (b) 5: total particle radius $R_{\mathrm{SLS}} = \langle R_{\mathrm{c}} \rangle + 2\sigma_{\mathrm{surf}}$ (black squares), average core radius $\langle R_{\mathrm{c}} \rangle$ (red circles), and the fuzzy shell thickness $2\sigma_{\mathrm{surf}}$ (green triangles).

that enter into those models as fitting parameters. We used these measurements to obtain information from dilute experiments that will be used to interpret the data at higher concentrations in Chapter V. In the two Chapters before that, however, we will look more carefully at the particles in dilute suspension, finding evidence of unexpected new behavior in both the neutral and ionized states.

CHAPTER III

NIPAM COLLAPSE FRUSTRATION AND UNEXPECTED INTERNAL MASS DISTRIBUTIONS

3.1 Introduction

In Chapter II, we performed a careful characterization of our particles at dilute conditions at different T and pH. Using 3DDLS, we obtained the hydrodynamic radius, $R_{\rm h}$ from an analysis of the particles' diffusion kinetics. We also fitted our SLS data to detailed model functions, allowing us to describe the internal structure of the particles. The most general result identified from the SLS is $R_{\rm g}$, the radius of gyration, defined as the root mean square distance of a particle's components from its center of mass.

By comparing $R_{\rm h}$, which gives the overall particle size, with $R_{\rm g}$, we can estimate the internal mass distribution of our particles. The ratio $R_{\rm g}/R_{\rm h}$ depends on this distribution: for a sphere of radius $R_{\rm h}$ with all the mass concentrated in a point at the center, $R_{\rm g}/R_{\rm h} = 0$. If all the mass is concentrated in a thin shell at the particle surface, $R_{\rm g}/R_{\rm h} = 1$. For a homogeneous sphere, $R_{\rm g}/R_{\rm h} = \sqrt{3/5} \approx 0.77$; for core-shell particles, values of $R_{\rm g}/R_{\rm h} \lesssim 0.6$ are usual for microgels of this cross-link density [129].

In Fig. 3.1 we show $R_{\rm g}/R_{\rm h}$ values for different T and pH. The pH 5.7 and 6.5 values are approximately constant with temperature, as expected from the lack of temperature dependence we observed in their DLS and SLS results. However, the low and intermediate pH results show unexpected behavior: at pH 3.1, $R_{\rm g}/R_{\rm h}$ increases to the upper limit of 1 above pNIPAM's LCST, while at pH 5 we observe a decrease to about 0.2, much lower than the $0.5 - 0.6$ that represents the lower bound usually observed for microgels. In this Chapter we will focus on pH 3.1, returning to the pH 5.0 case in Chapter IV.

3.2 An Introduction to SANS

The high values of $R_{\rm g}/R_{\rm h}$ imply that mass is migrating to the particle surface at higher T for the particles at pH 3.1. However, the full form factor available to our SLS experiments

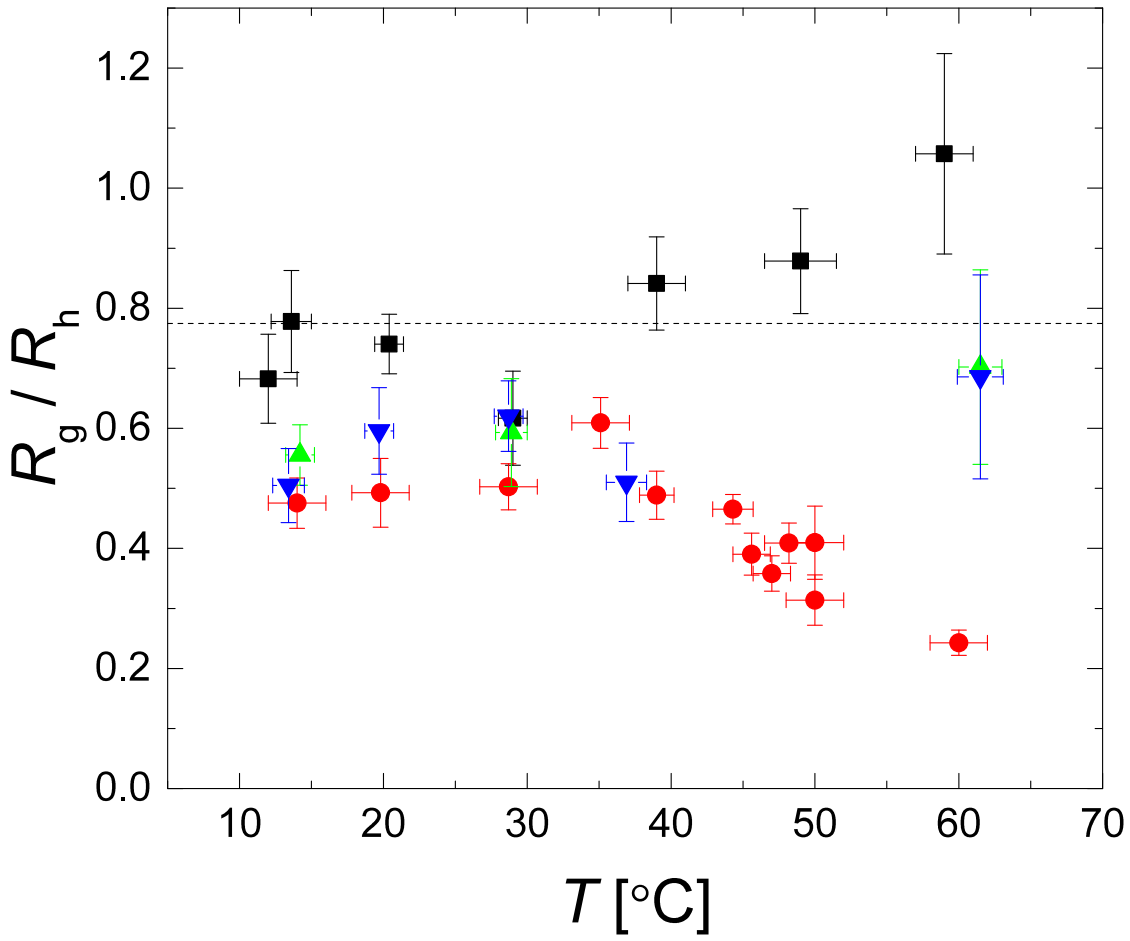

Figure 3.1: Values of R_g/R_h as a function of T for four different pHs: 3.1 (black squares), 5.0 (red circles), 5.7 (green upward triangles) and 6.5 (blue downward triangles). The dashed line is the homogeneous sphere value. Note that above pNIPAM's LCST of $T \approx 32$ °C the pH 3.1 value increases to $\approx 0.9 - 1$, while the pH 5.0 value decreases markedly to around ≈ 0.2. The pH 5.7 and 6.5 values are unchanged from their low-T values of $\approx 0.6 - 0.7$.

cannot provide a more detailed view of the particles' internal structure: as shown in Fig. 2.16a, at high T, only the initial decay of $P(q)$ is visible.

$q = (4\pi/\lambda)\sin(\theta/2)$ is inversely proportional to the length scale being probed. In order to access higher ranges of q, and thus smaller length scales inside the particle, we turn to small-angle neutron scattering (SANS). Conceptually, SANS is very similar to SLS, with the principal difference being that the accessible q range is given by a neutron's de Broglie wavelength, $\lambda = h/p$, with h Planck's constant and p the neutron's momentum. From a practical standpoint, the infrastructure required to build and operate a neutron scattering facility is enormously more complex and expensive than even a high-end light scattering

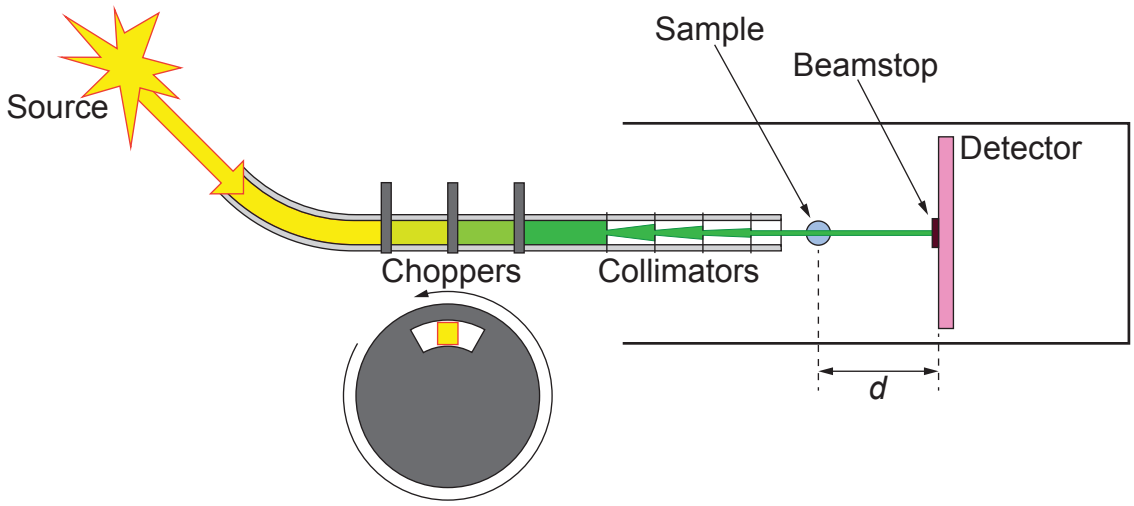

Figure 3.2: A simplified representation of the EQ-SANS instrument at Oak Ridge as described in the text. Not to scale.

device, and SANS experiments are therefore carried out at national labs. The neutron scattering experiments described in this Thesis were carried out at Oak Ridge National Laboratory's Spallation Neutron Source using the EQ-SANS instrument [130].

A rough schematic of this SANS setup is shown in Fig. 3.2. First, neutrons emitted from the spallation source are guided through a bend in the neutron optics so there is no direct line of sight between the source and the detector. Three velocity selectors, or "choppers," allow only neutrons with a narrowly-defined velocity distribution to pass. Each chopper is a metal drum with a slot cut into it in the path of the neutron beam, as shown in the figure. Because the neutrons' de Broglie wavelength is inversely proportional to momentum and therefore velocity, this results in an almost monochromatic beam with a wavelength distribution width on the order of 1

The detector is a 1×1 m bilayer bank of ^{3}He tubes. Before analysis, the data is processed by correcting for a number of systematic errors: gravity; the dark current; the empty beam; sample cell and solvent background; detector efficiency; and q smearing [130]. These corrections are described below.

Gravity. Neutrons with larger λ have a correspondingly slower velocity and therefore a longer time of flight after passing through the sample before they hit the detector. Gravity has a small systematic effect on the scattered neutrons, particularly if the wavelength is

selected to be large. This acts to vertically displace the entire scattering profile downward by a small amount, which is corrected simply by adjusting the measured intensity profile upward. The necessary adjustment is determined from a measurement of the beam center in the absence of a sample.

Dark current. The dark current is the intensity measured at the detector when the beam is cut off, and represents one source of background noise in a measurement. Its contribution to the measured intensity is small and can be subtracted from the data before analysis.

Empty beam. When the transmitted beam hits the beamstop, some neutrons are scattered into the detector and affect the measured intensity. This contribution can be measured in the absence of a sample and subtracted from the data.

Sample cell and solvent background. In addition to the particles of interest, the sample cell and any solvent may provide some background scattering that contributes to the noise level. In order to minimize this, deuterated solvents are generally used. Further, this background can be measured by scattering from the solvent in an identical cell in the absence of sample particles, and is then subtracted from the actual measurements.

Detector efficiency. The detector efficiency is not completely uniform. Variations in efficiency across the detector are estimated from the measurement of an isotropically scattering sample such as water.

q smearing. Imperfect q resolution can be caused by a variety of effects, including spread in the wavelength, unavoidable imperfections in the collimation optics, and the finite pixel resolution of the detector itself [131].

- Wavelength spread occurs because the neutrons in a SANS experiment are allowed through the choppers with a finite-width distribution in velocity and therefore λ. Recall that $q = (4\pi/\lambda)\sin(\theta/2)$. For a truly monochromatic beam, only θ, defined by the detector distance d and the radial distance of a detection event from the center of the beam, would change q. Because of the finite λ distribution, there is a small uncertainty in the exact q of each detection event.

- Collimation smearing is caused by the finite (nonzero) size of the pinholes used to

collimate the beam, which means that the neutrons in the beam are not all parallel, and thus even neutrons with a single λ can scatter into a small range of q.

- The pixel size of the detector is $\sim 5.5 \times 4.3$ mm [130] (the vertical and horizontal resolutions are different due to the alignment of the detector tubes), which limits the resolution even absent contributions from the other two factors.

All sources of resolution error can be accounted for by convoluting the model function used to fit the data with a resolution function dependent on the exact geometry used to make the measurement [131], or by taking the smearing as an uncertainty in each q-value and weighting the fit accordingly. This approximate uncertainty is $(\delta q/q)^2 = (\delta\lambda/\lambda)^2 + \cot^2\theta(\delta\theta)^2$ [130], where the first term is due to wavelength spread and the second term is a combination of collimation smearing and finite pixel resolution contributions. Either method of resolving the resolution constriction is limited when fine details are expected over a q range comparable to the resulting uncertainty (e.g. sharp minima in the form factor of a monodisperse hard sphere suspension). However, because we are interested primarily in the final decay in that range, this shortcoming will not be problematic.

The number of neutrons scattered into a solid angle element of the detector $\Delta\Omega$ in time Δt for a given q is given by [132]

$$I(q) = \Phi_0 \Delta\Omega \Delta t \frac{T_{\text{sample}}}{T_{\text{empty}}} a D_{\text{sample}} \epsilon(\lambda) \frac{\mathrm{d}\Sigma_V}{\mathrm{d}\Omega}(q), \tag{3.1}$$

where Φ_0 is the incident neutron flux (neutrons per unit area and unit time), T_{sample} and T_{empty} are the transmissions of the sample and empty cell, respectively, a is the illuminated sample area, D_{sample} is the sample thickness, $\epsilon(\lambda)$ is the efficiency of the detector at neutron wavelength λ, and $\mathrm{d}\Sigma_V/\mathrm{d}\Omega(q)$ is the differential scattering cross section per unit volume. T_{sample} is measured via a small pinhole and detector in the beamstop, and T_{empty} from a similar measurement of the empty beam. The other factors are calculated from the measurement geometry except for $\mathrm{d}\Sigma_V/\mathrm{d}\Omega(q)$, which is dependent on the sample, and has the same definition as Eq. 2.23.

For isotropic samples such as ours, the neutron scattering data is azimuthally averaged over the entire detector area, as shown in Fig. 3.3, to get the best possible statistics. This

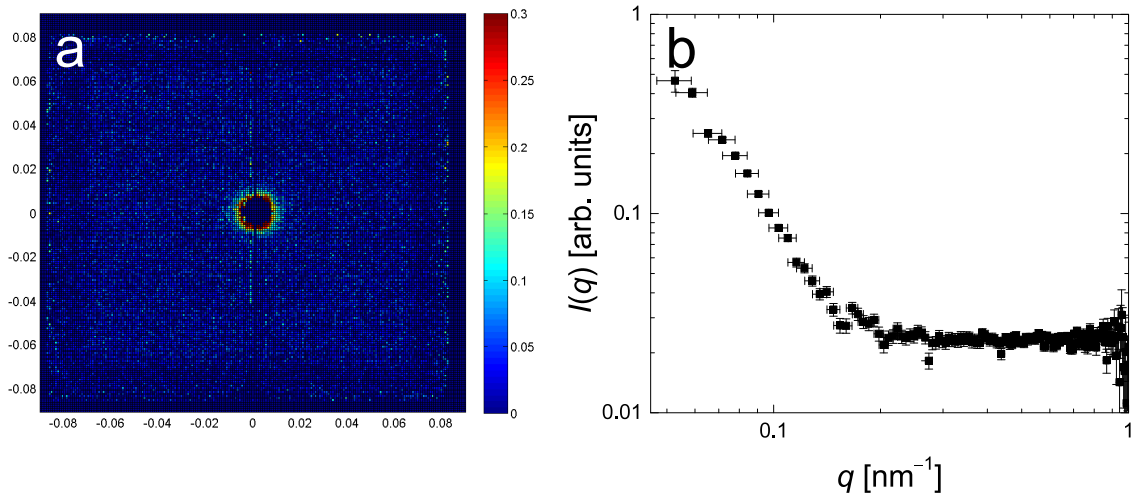

Figure 3.3: An example of radial averaging of our SANS data. (a) The intensities measured by each pixel in the SANS detector, showing intensity increasing from blue to red. We observe a strong initial decay beginning immediately past the central beamstop (the black circle) and a comparatively faint background far from the center. (b) The same data after being processed as described in the text, converted to units of q, and azimuthally averaged.

allows us to directly compare a 1-dimensional data set from the SANS experiment to our SLS data.

In order to minimize the incoherent background due to ^{1}H atoms in the solvent, we prepared our samples for SANS in D_2O and decreased the pH with DCl instead of HCl. Because the ^{2}H atoms in a heavy water mixture have a different thermodynamic activity than ^{1}H atoms, a pH mesurement made on a sample in heavy water will not accurately reflect the actual pH [133, 134]. Accordingly, we adjust our deuterated samples' pH according to the following formula [135]:

$$\mathrm{pD} = 0.42 + 0.93\mathrm{pH}_{\mathrm{meas}}. \tag{3.2}$$

Here, pD is the desired pH, and $\mathrm{pH}_{\mathrm{meas}}$ is the pH measured in the deuterated sample using a pH electrode calibrated for use in light water. For example, to make a deuterated sample at the same conditions as a pH 3 sample in light water, we adjust the pH of the deuterated sample until the pH meter reads 2.77, since $3 = 0.42 + 0.93 \times 2.77$. We compare SLS measurements of the SANS samples that are prepared without ^{2}H but are otherwise identical, and see an identical intensity profile, confirming that we really are examining the same conditions in each case.

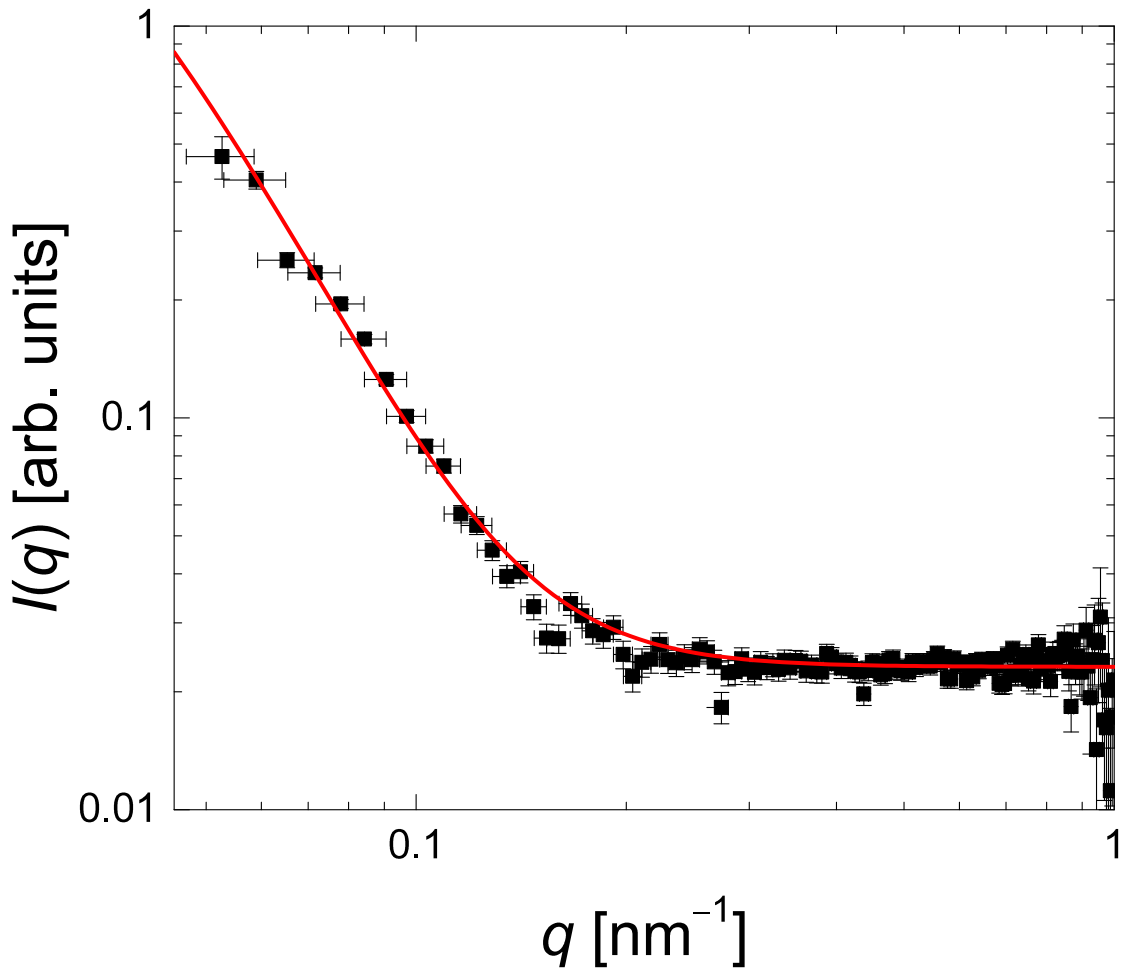

Figure 3.4: SANS data for the pH 3.1 sample at $T = 59$ °C. The red line is the best fit to the second and third terms of Eq. 2.35.

3.3 Fitting the Form Factors at Smaller Length Scales

Fitting the SANS data involves two steps. Just as with the SLS data, which was fitted independently of any SANS measurements, we first fit the SANS data independently of the corresponding SLS measurements as well. Because of the high q range, we use only the second and third terms in Eq. 2.35 to fit the SANS data. This gives us initial values for ξ and μ. An example of this fit is shown in Fig. 3.4.

Once both the SLS and SANS data have been fitted separately, we next confirm that Eq. 2.35 can indeed describe all of our scattering data simultaneously. Because the q ranges of the SLS and SANS experiments do not overlap, we cannot know the absolute scaling between each of the two data sets. In order to perform the simultaneous fit, we make use

of a fitting algorithm where the relative scaling of the two data sets is included as a free parameter. This algorithm is implemented in Mathematica.

We import the experimental data from the SLS and SANS experiments. We also define a large number of model functions, taken from fits to the SLS data to Eqs. 2.35, 2.45, and 2.46, each with a slightly different set of fit parameters. We vary the parameters independently over the range $(x - \Delta x, x + \Delta x)$, where x is a given fitting parameter and Δx is the uncertainty in that parameter from the appropriate fit. x is varied in steps of δx.

For example, if we fit using the core-shell form factor described in Eq. 2.45, our form factor would have $\sigma_{\rm p}$, $\langle R_{\rm c} \rangle$, and $\sigma_{\rm surf}$ (from the SLS fit), and μ and ξ (from the SANS fit) as our x parameters.

The model functions are then generated to span the possible values of $\langle R_{\rm c} \rangle$, $\sigma_{\rm p}$, and $\sigma_{\rm surf}$. I_1 is normalized so that $P(q = 0) = 1$; I_2 and I_0 are always low enough that they do not affect this normalization. The relative values of I_2 and I_0 are fixed from the fits to the SANS data, but their absolute values have not been determined yet.

We fit each of the model functions (each one having its own values of the x parameters) to the SLS and SANS data, starting with an increment of $\delta x \sim 0.1 \Delta x$. We further allow the absolute scaling of the SANS data to vary as an additional fitting parameter. An example of such a fit is shown in Fig. 3.5a. We tabulate the quality-of-fit parameter χ^2 for each fit, and select the values of the x parameters that give the smallest χ^2. We repeat this process iteratively for smaller and smaller increments δx, as shown in Fig. 3.5c–e, until the fit has been optimized, giving us the final fit, shown in Fig. 3.5b. Fig. 3.6 shows final fits for all conditions.

We find that the intriguing behavior of the system at low pH and high T, hinted at by the unusual increase of $R_{\rm g}/R_{\rm h}$, extends to the high-q region probed by SANS as well. Specifically, we find that the high-q data at high T cannot be fitted by $\mu < 2$, as shown in Fig. 3.7b and c. The SANS data for the low-T case, shown in Fig. 3.7a, can be fitted by $1 \leqslant \mu \leqslant 2$. However, the SLS data can only be described at high q by a fit with $\mu = 2$. In Fig. 3.6a we show the SLS data for this sample together with the best fit to the first term in Eq. 2.35. Note that the second minimum in the data is not accurately reproduced

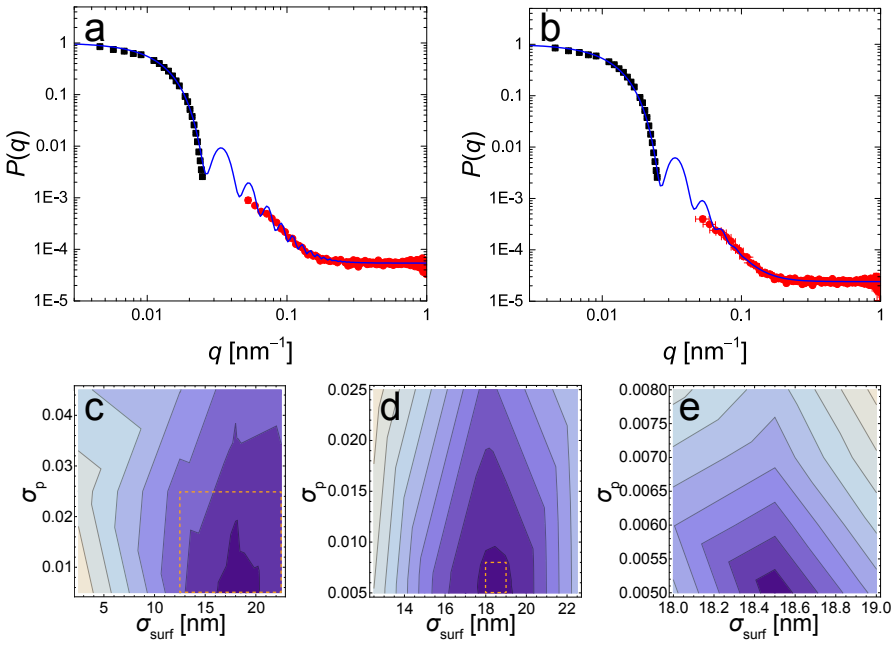

Figure 3.5: The algorithm used to find the best fit to the experimental data for the system at pH 3 and $T = 50$ °C. (a) Experimental SLS and SANS form factor data (black squares and red circles, respectively), together with the fit to Eqs. 2.35 and 2.45. The first term in Eq. 2.35 uses values of σ_p, $\langle R_c \rangle$, and σ_{surf} determined from fits to the SLS data alone, and the second term uses the values of μ and ξ determined from fits to the SANS data alone. The ratio I_0/I_2 is also fixed from the SANS fit, but the absolute value of I_0 (and therefore, by extension, I_2) is left as a free parameter. (b) The best fit, with all fitting parameters ($\langle R_c \rangle$, σ_p, σ_{surf}, and I_0) all chosen to minimize χ^2. (c-e) Contour plots of the χ^2 values of each fit, for a particular $\langle R_c \rangle$, as a function of σ_p and σ_{surf}. The dashed orange boxes show the areas of each succeeding plot as the test parameters are refined. Darker areas on the plot correspond to lower values of χ^2.

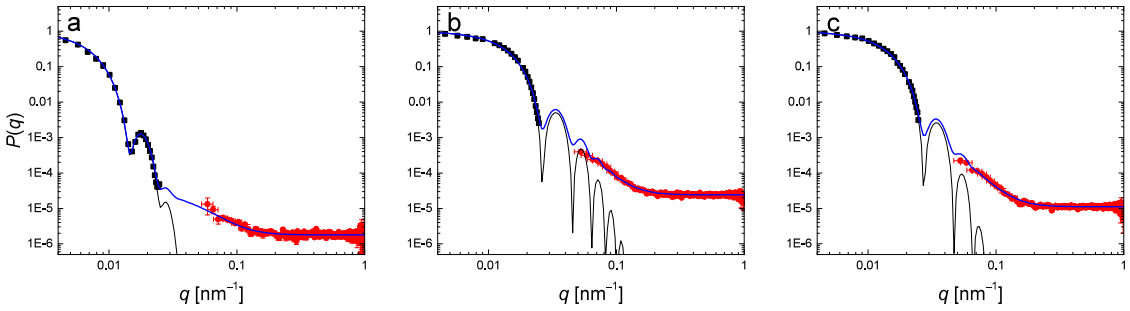

Figure 3.6: The final fits of Eq. 2.35 to both the SLS (black squares) and SANS data (red circles) for samples at pH 3 and (a) $T = 14$ °C, (b) $T = 50$ °C, and (c) $T = 59$ °C. The uncertainty in the black points is too small to appear on the graph. The thick blue lines are fits to Eq. 2.35, and the thin black lines are fits to just the first term of Eq. 2.35. Note that for the $T = 14$ °C sample, the second minimum in the SLS data cannot be fitted by only the first term; the second term with $\mu = 2$ is necessary.

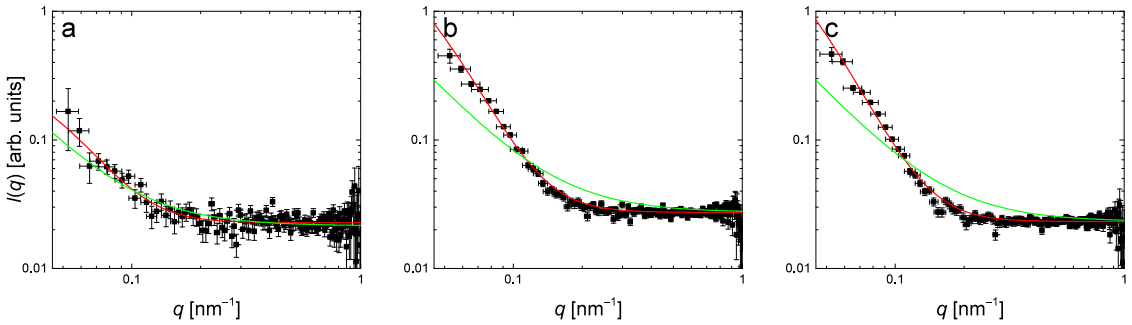

Figure 3.7: SANS data for the pH 3.1 sample at (a) $T = 14$ °C, (b) $T = 50$ °C, and (c) $T = 59$ °C. The green and red lines are the best fits to the second term of Eq. 2.35 with $\mu = 1$ and $\mu = 2$, respectively.

by the fit: the q-value of the minimum is the same in both cases, but their values on the y-axis are separated by half an order of magnitude. We find that this minimum can be reproduced by a $\mu = 2$ term with the same ξ as obtained from the SANS fit at the same conditions. However, a $\mu = 1$ term fails to reproduce the minimum no matter what value of ξ is chosen, because its shallower decay completely washes out the minimum. As additional confirmation, the asymptotic behavior of the first term in Eq. 2.35 with Eq. 2.44 with finite shell thickness is close to q^{-6} due to the influence of the Gaussian convolution, and not to the q^{-4} decay observed for Porod scattering for a sharp interface [136, 137]. As a result, the observed SANS decay, which goes as q^{-4} for high q and $\mu = 2$, cannot be explained as a remnant of the Porod limit.

This is unusual: $\mu = 1$ corresponds to the Lorentzian model for a polymer network with average mesh size ξ [112, p. 82-85], which we expected for these microgels. $\mu = 2$ describes the Debye-Bueche model for for an inhomogeneous scattering medium with a length scale ξ [113, 114], indicating that the polymer inside these microgels is contracting into discrete clumps rather than undergoing an affine deswelling above pNIPAM's LCST. We explore this phenomenon in the next section.

3.4 Frustration of pNIPAM Collapse

The best fit parameter values from our model function are shown in Table 3.1.

ξ increases by 50% above pNIPAM's LCST, coinciding with the increase in R_g/R_h, as shown in Fig. 3.8. Both increases are new and unusual behaviors very different from what

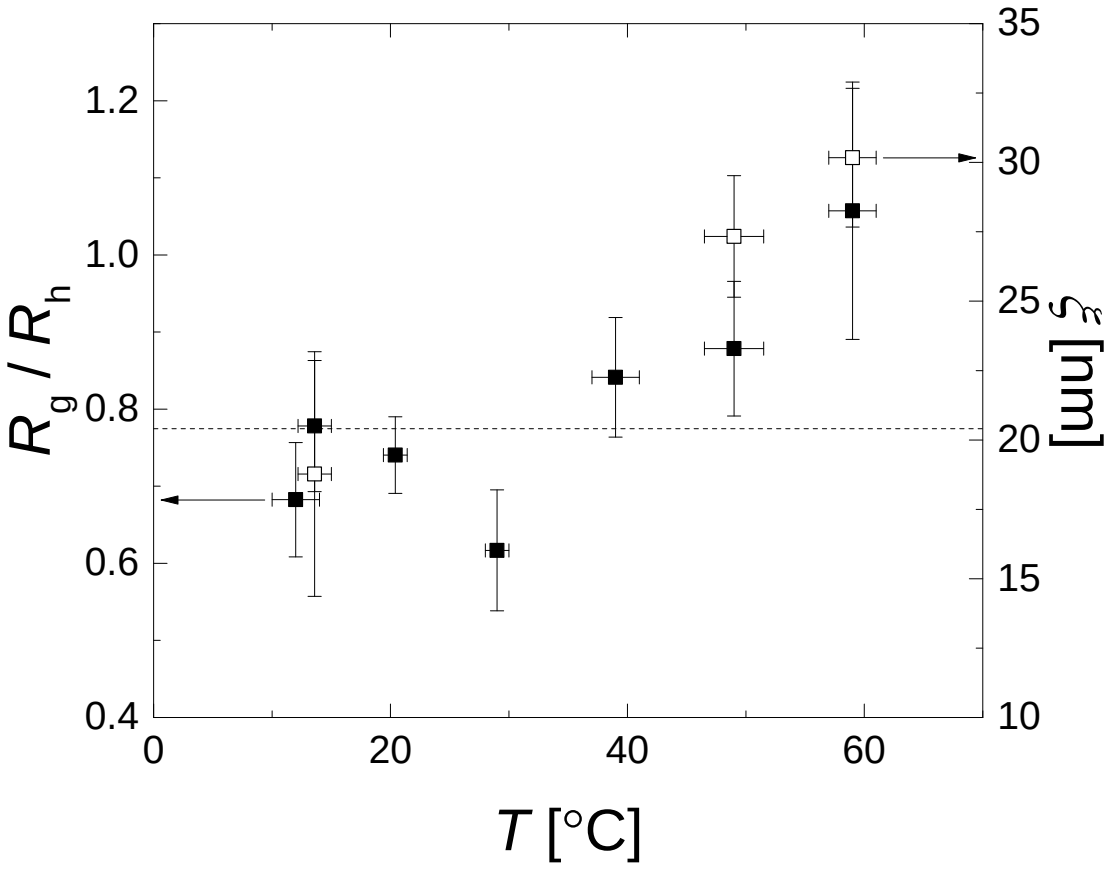

Figure 3.8: R_g/R_h (filled squares), obtained from dilute SLS and DLS measurments, and ξ (open squares), obtained from SANS measurements, of crosslinked microgels at pH 3.1 for various temperatures. R_g/R_h follows the left y-axis, and ξ the right y-axis. The value of R_g/R_h for homogeneous spheres, $\sqrt{3/5} \sim 0.775$, is shown as a dashed line for comparison.

Table 3.1: Parameters measured for the particles as a function of temperature. In all cases, $\mu = 2$. The uncertainty in $\langle R_c \rangle$ and $2\sigma_{\text{surf}}$ where a corresponding SANS measurement was made is smaller because the need to also fit the SANS data constrained their values. The polydispersity in the samples measured without SANS essentially represents an upper bound, as satisfactory fits could be made to the SLS data alone even with zero polydispersity.

T [°C]	$\langle R_c \rangle$ [nm]	$2\sigma_s$ [nm]	σ_p	ξ [nm]
12 ± 2	317 ± 1	136 ± 4	0.015 ± 0.014	
13.6 ± 1.4	306 ± 2	146 ± 4	0.048 ± 0.01	19 ± 4
20.4 ± 1	290 ± 2	121 ± 8	0.047 ± 0.003	
29 ± 1	210 ± 1	50 ± 20	0.015 ± 0.014	
39 ± 2	176 ± 4	30 ± 30	0.025 ± 0.024	
49 ± 2.5	170 ± 3	37 ± 5	0.075 ± 0.007	27.3 ± 2.2
59 ± 2	164 ± 6	59 ± 5	0.076 ± 0.007	30.2 ± 2.5

is commonly observed for pNIPAM microgels crosslinked with BIS instead of pEG-d and synthesized with much less AAc than the 24 mol% included in this synthesis. As a result, our starting hypothesis was that the presence of pEG-d as a crosslinker, the excess of AAc, or both, result in the observed high-temperature behavior. Previous work with pNIPAM microgels without AAc and crosslinked with 2 mol% pEG-d, with $n \sim 13$ repeat units per chain (close to the 10-11 repeat units per chain in our particles), also reported unusual, but different, behavior compared to what we observe [65]. In addition to the LCST transition deswelling around 32 °C, they observed a prior deswelling transition at 17.3 °C. This was attributed to the hydrophilicity of pEG-d, which does not change with temperature; the idea was that depending on the temperature, the hydrophilic competition between pEG-d and pNIPAM would be dominated by one or the other. Importantly, however, for those particles, R_g/R_h was always smaller than or comparable to the homogeneous sphere value of $\sqrt{3/5}$. In addition, the form factor of these particles was successfully fitted with a star polymer model using $\mu \sim 0.1$ at low T, $\mu \sim 0.7$ near the LCST, and $\mu \sim 1$ at high T. The internal structure of the particles at high T was thus well described by a Lorentzian, in contrast to our results. Similar microgels crosslinked with BIS have also been successfully described with a Lorentzian [138]. Hence, it is unlikely that the high-temperature behavior we observe in our microgels solely results from the presence of pEG-d.

Alternatively, this behavior could result from the presence of large amounts of AAc.

When charged, AAc causes swelling in our system by drawing counterions from the outside solution into the particle. In contrast, neutral AAc exerts no influence on the swelling or deswelling behavior of the system beyond breaking up segments of pNIPAM, assuming it is randomly copolymerized throughout the particle, as in our case. To understand this, we note that the collapse of pNIPAM in water at its LCST is cooperative—that is, the entire pNIPAM chain collapses as a whole. The minimum chain length necessary for this collapse to occur is about 10 repeat units [139]. However, in the case of our particles, there is sufficient AAc to potentially frustrate this collapse. Indeed, previous work [140] found that for randomly copolymerized, neutral polymer chains composed of NIPAM and AAc, an increasing fraction of chains failed to collapse above NIPAM's LCST as the AAc content increased. We thus hypothesize that it is the presence of neutral AAc in our particles which predominantly causes the high-temperature behavior we observe.

To test our hypothesis, we estimate the average number of monomers between crosslink points as $(73\ \mathrm{mol\%_{pNIPAM}} + 24\ \mathrm{mol\%_{AAc}})/(3\ \mathrm{mol\%_{pEG\text{-}d}}) \sim 32$, and calculate the probability that there will be a run of ten or more consecutive NIPAM monomers, with a 75% probability that a given monomer is NIPAM and a 25% probability that it is AAc. We do so using that [141]

$$\mathcal{P}(\ell_n \geqslant m) = \sum_{j=1}^{\mathrm{floor}[n/m]} (-1)^{j+1} \left[p + \frac{n - jm + 1}{j}(1-p) \right] \times \binom{n-jm}{j-1} p^{jm} (1-p)^{j-1}, \quad (3.3)$$

where $\mathcal{P}(\ell_n \geqslant m)$ is the probability that there will be a run of successive "A" events with length ℓ_n greater than some number m, p is the probability of an "A" event, and $1-p$ is the probability of a "B" event. In this case, "A" represents a NIPAM monomer and "B" an AAc monomer, with $p = 0.75$, $m = 10$, and $n = 32$. We obtain that $\mathcal{P}(\ell_n \geqslant m) = 45\%$. Hence, we find there is about an even chance that a given polymer chain between two crosslinker points will have enough consecutive pNIPAM monomers to at least partially collapse. This implies that the microgel structure at the polymer level will be heterogeneous, since some monomer sequences will collapse and some will not, supporting our hypothesis.

In microgels crosslinked with pEG-d and BIS where the polymer network was successfully modeled with a Lorentzian, ξ was observed to decrease with increasing T [65, 138].

This indicates that the network length scale changes in an approximately affine way with the overall particle size. In our microgels, the characteristic internal length scale increases as the overall particle size shrinks. This, together with our finding that $\mu = 2$, indicates the formation of relatively large heterogeneous clumps within the particle at high temperature, further emphasizing the key role played by the relatively large amount of neutral AAc in our particles. We emphasize that the clumps are not composed entirely of AAc; on the contrary, we expect them to be formed from NIPAM-rich sequences that are able to collapse together, and that they are separated by regions of sequences comparatively rich in AAc that are therefore unable to collapse.

Our observation that $R_g/R_h > \sqrt{3/5}$ indicates that these clumps preferentially form at the particle periphery rather than being concentrated at the particle center or distributed homogeneously throughout. This makes sense: as confirmed by the particles' core-shell morphology at lower T, the crosslinker reacted faster than the monomers during synthesis and thus the concentration of pEG-d decreases from the particle center to the periphery. As a result, the chains between crosslink points will be shorter near the particle center, hence decreasing the number of NIPAM sequences long enough to collapse at high temperatures.

A schematic of our particles at pH 3.1 is shown in Fig. 3.9. The heterogeneities in the schematic for 59 °C are not drawn to scale; the internal length scale ξ is at least a factor of 10 smaller than the particle diameter. Hence, these heterogeneities are relevant at the polymer level and do not significantly affect the particle structure at larger length scales. This is why they are only apparent at the q values probed with SANS.

3.5 Conclusions

In measurements of NIPAM-*co*-AAc microgels with a high mol% of AAc, we have observed an increase in R_g/R_h with T that coincides with a similar increase in heterogeneity length scale ξ as modeled with the Debye-Bueche scattering term. We attribute this to the frustration of the pNIPAM coil-to-globule transition caused by the presence of large amounts of neutral AAc, which interrupt the continuous chains of pNIPAM the transition requires. At high temperatures, the measured R_g/R_h approaches 1, well above the usual homogeneous

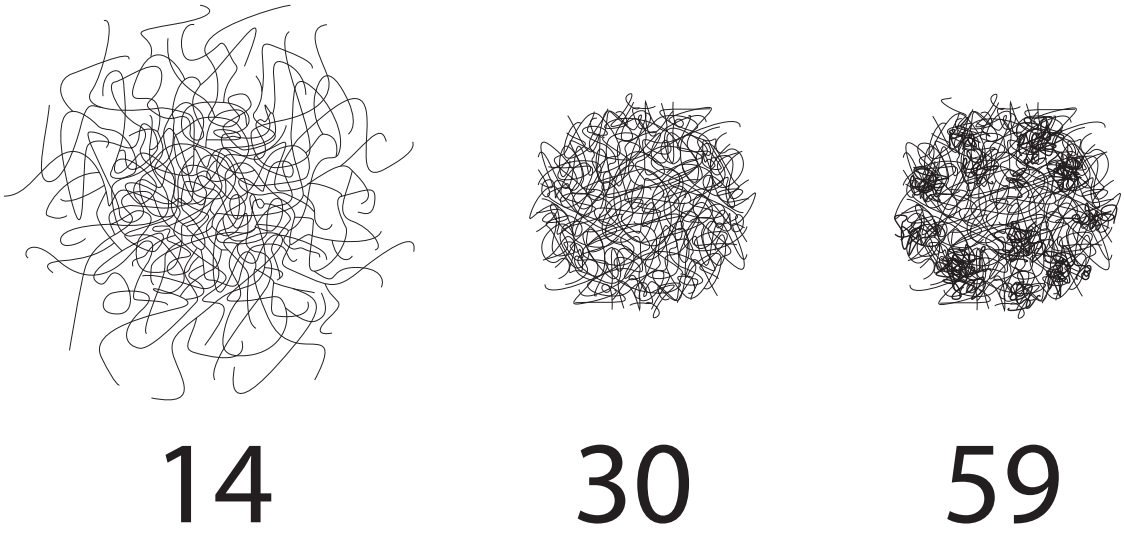

Figure 3.9: Representative schematic of the microgel conformational changes for several different T in °C.

sphere upper limit, $\sqrt{3/5} \sim 0.775$. This highly unusual observation suggests a new path for generating microgels with high $R_{\mathrm{g}}/R_{\mathrm{h}}$ morphology, as well as microgels that can transition from relatively homogeneous polymer networks to networks with dense polymer clumps separated by stretched polymer chains. Because this phenomenon should be generalizable to any polymer network with the appropriate chemistry, it should also allow the synthesis of macrogels with similar properties.

CHAPTER IV

CHARGE SEGREGATION IN THE SINGLE PARTICLE

4.1 Introduction

In Chapter III, we compared the unusual behavior of R_g/R_h at high T with the network parameters ξ and μ. This allowed us to understand the unusual intra-particle structure of the polymer. In this Chapter, we follow the same path, except in the case where our particles are partially ionized, i.e. pH 5. At high temperatures, we find an unusual concentration of mass to the particle center, coincident with a decrease in the particles' polymer distribution length scale. We understand these phenomena in the context of a theory already developed for charge segregation in weakly-charged polymer networks in a bad solvent. However, our experimental data are not fitted well by the theory. We compare the theory to experiments on microgels synthesized without crosslinker, leading to a homogeneous polymer distribution, and see good agreement. We therefore conclude that the differences observed in the crosslinked microgels are due to the crosslinker, which is concentrated towards the particle center.

4.2 Segregation of Mass at the Particle Center

In Fig. 3.1 we showed that the value of R_g/R_h decreases for pH 5 suspensions from ~ 0.5 at low T to 0.2 at high T. R_g/R_h can vary between 0, for a particle with all the mass concentrated at a point in the center, to 1, if all the mass is concentrated in a thin shell at the periphery. The value for homogeneous spheres is $\sqrt{3/5} \sim 0.775$; values lower and higher than this indicate mass concentrated towards the particle center or periphery, respectively. For typical core-shell microgels, values of $R_g/R_h \sim 0.5$–0.6 represent an approximate lower bound. To our knowledge, our results are the first to give such low values: $R_g/R_h = 0.2$ indicates that almost all of the particle mass lies within half a radius of the center.

This is unexpected, not only because of the extremely small value, but because the high-T value of R_g/R_h is lower than the low-T value, in contradiction to the usual behavior of

pNIPAM microgels. For a pNIPAM microgel (crosslinked, but synthesized without AAc or other comonomer), the low-T state of the microgel is typically core-shell, with low R_g/R_h, while the high-T state is closer to a homogeneous sphere, with a higher value [117]. This is because, during synthesis, the crosslinker reacts faster than the NIPAM monomer, leading to a higher crosslinker density near the center of the particle. At low T, the pNIPAM polymer is hydrophilic and the particle swells, but because of the inhomogeneous crosslinker distribution, the core is constrained and unable to swell as much as the periphery. At high T, when all the pNIPAM is hydrophobic, the periphery deswells to approximately match the core.

The only significant difference in our case is the presence of the ionized AAc. As observed in Ch. 3, uncharged AAc has the effect of frustrating the pNIPAM deswelling process, which in our system leads to an increased R_g/R_h. Thus, since the only difference is that the AAc is partially ionized at pH 5, the decreasing R_g/R_h we observe in our pH 5 samples must be a direct consequence of charge.

4.3 Segregation of Charged Groups: Weakly Ionized Polymer Networks in a Bad Solvent

The thermodynamic theory for partially ionized polyelectrolytes and polymer gels is well-developed. Specifically, we want to understand the behavior of partially charged polymer networks in a bad solvent, for which a theory has been developed and experimentally verified for macrogels [142, 143]. In these systems, the component of the polymer that favors demixing from the solvent tends to cause the network to contract, which localizes the network charges into a smaller area. To maintain electroneutrality, the counterions in the solvent must remain localized to these charges, and are therefore confined to a smaller volume. This imposes an entropic cost on the portion of the system represented by the counterions. The system offsets this cost by allowing the polymer network to locally swell near the charged groups, increasing the volume accessible to the localized counterions and resulting in a spatial fluctuation in polymer concentration depending on the distribution of charges. This state of affairs persists as long as the deswelling tendency is not so large that it dominates the entropic swelling effect due to the counterions.

The phase behavior of such systems is governed by two parameters: the charge concentration and the solvent quality. In dimensionless form, the charge concentration is written as

$$s = (\kappa r_0)^2, \tag{4.1}$$

where $\kappa^{-1} = \sqrt{(R_0)^3/3\ell_{\rm B}Q}$ is the Debye length (written for a spherically symmetric microgel particle), $\ell_{\rm B} \sim 0.7$ nm is the Bjerrum length, and Q is the number of charges in the microgel, and we take R_0 to be the dilute hydrodynamic radius, $R_{\rm h}$, of the particles. r_0 is the characteristic screening scale of charges in the polymer by the ions in solution, and is given by

$$r_0 = a\left(\frac{48\pi\ell_{\rm B}}{a}\phi_{\rm p}\alpha^2\right)^{-1/4} \times \begin{cases} \left[1+\left(\frac{1-2\chi}{2\phi_{\rm p}}\right)^{1/2}\right]^{1/8} & \chi < \frac{1}{2} \\ 1 & \chi \geqslant \frac{1}{2} \end{cases}, \tag{4.2}$$

where a is the length of a monomer, $\phi_{\rm p}$ is the volume fraction of the monomer *inside the network* (not to be confused with the microgel volume fraction, ϕ), α is the degree of ionization of the monomers, and χ is the temperature-dependent Flory interaction parameter between the network and the solvent, given for pNIPAM in heavy water by [144]

$$\chi = \frac{1}{2} + 25\left(1 - \frac{306.5\text{ K}}{T}\right). \tag{4.3}$$

This was experimentally measured for pNIPAM macrogels for temperatures between $T = 20$ and 40 °C, but there is no reason not to expect this equation to hold for all of our measured T. Further, since we are concerned with the microgel behavior when the solvent is poor ($\chi > 1/2$), and therefore use only that form of Eq. 4.2.

In dimensionless form, the reduced temperature (which describes the solvent quality) is given by

$$t = -12\left(\frac{r_0}{a}\right)^2\frac{h}{a^3}\phi_{\rm p}, \tag{4.4}$$

with h a solvent quality parameter defined as

$$h = -a^3(1-2\chi) - 3B_3\phi_{\rm p}, \tag{4.5}$$

where B_3 is the third virial coefficient.

A phase diagram [142, 143] is shown in Fig. 4.1. The diagram is divided into 8 regions,

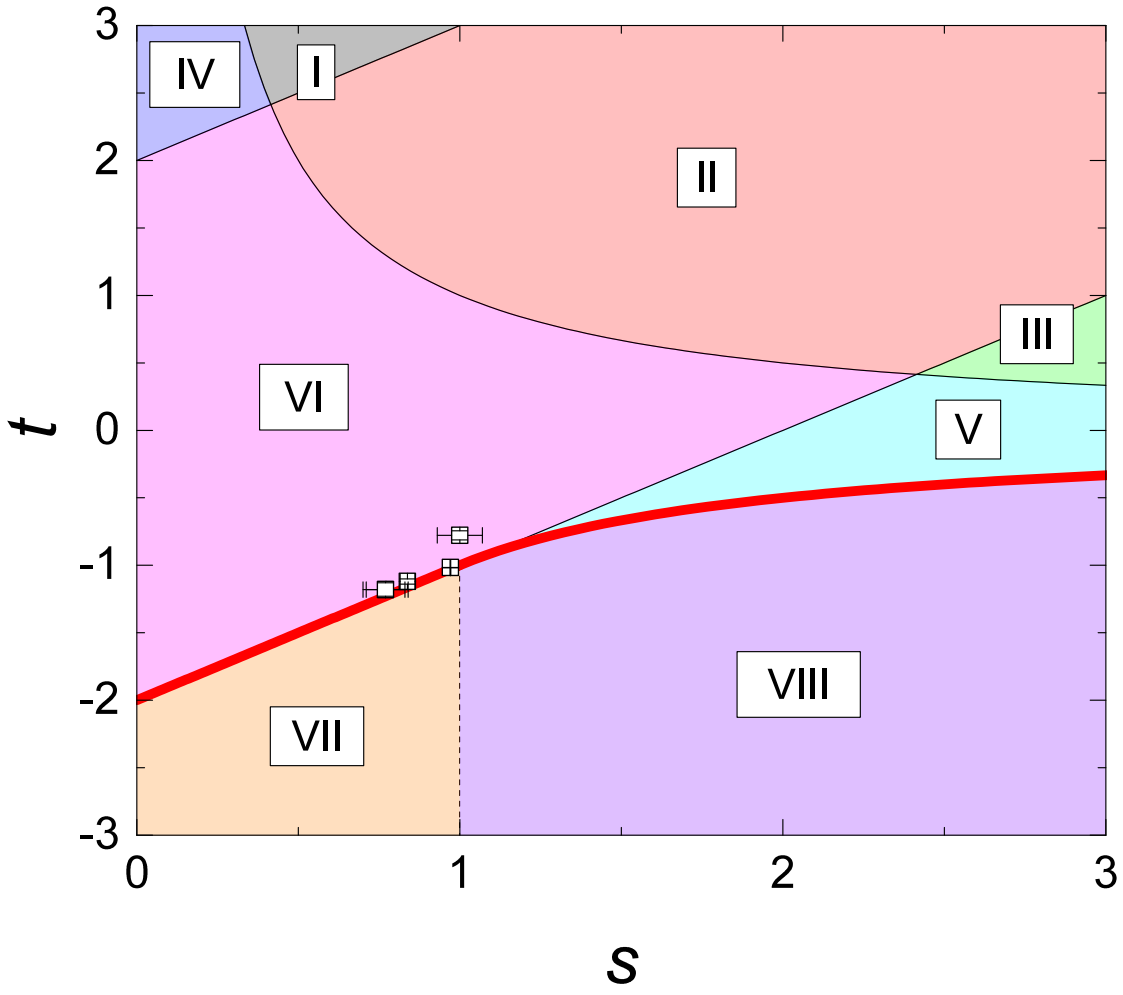

Figure 4.1: The phase diagram for charged polymer networks as a function of s, reduced charge concentration, and t, reduced temperature. Black squares are data points from ULC microgels as discussed in the text, with measurments at higher T having lower s and t values. The curves $|st| = 1$ separate regions based on their asymptotic thermodynamic behaviors. The curves $|s - 2| = 2$ separate regions based on whether the Debye length or the network correlation length is larger. The dashed line, $s = 1$ for $t < -1$, denotes the region where the Debye length and the chain screening length have the same value. The polymer demixes at the spinodal, shown as a thick red line. Regions VI and VII are discussed in the text.

labeled I–VIII, depending on the values of s and t. These regions are divided by the lines $|s - t| = 2$, which denote changes in the screening regime, and $s = 1$, $t < -1$, together with the curves $|st| = 1$, where the thermodynamic behavior changes. The detailed thermodynamic states of the 8 regions are too complex to cover extensively here, but they can be briefly summarized as follows:

In regions I–III, the solvent quality is good and the concentration of ions is high enough that κ^{-1} is larger than the network correlation length expressed in Eq. 2.32, ξ, and therefore the salt concentration effects on screening are unimportant. In region I, ξ is less than the persistence length of the polyelectrolyte that forms the network [145, 146], while the opposite is true in region III, where excluded-volume effects are negligible. In region II, they are comparable and the electrostatic potential oscillates with near-zero amplitude.

Region IV is similar to region I, except that the charged polymer itself is responsible for screening, rather than the solvated ions. Region V bears the same similarity to region III. Further, when $st = -1$ at the boundary of region V, the Coulomb interaction between charges is not screened, indicating that the system is unstable to phase separation. IIn the same way, region VI is similar to region II, and at $s - t = 2$, $s \leqslant 1$ reflects the instability of the system to microphase separation as the elecctrostatic interactions of the charged groups effectively become unscreened. In this region, the system is unstable and undergoes large concentration fluctuations.

Regions VII and VIII are the microphase separated and macrophase separated two-phase regions, respectively. In both cases, the charged/swollen and uncharged/deswollen volumes of the polymer network are separated, the only difference being that those volumes are small relative to the overall network size in the microphase separated case, and comparable to the overall size in the macrophase separated case.

The regions of interest for our experiments are those with $s < 1$, where the contributions of charged groups are important, and $t < 0$, corresponding to poor solvent quality; the specific regions are VI and VII.

In order to determine the region occupied by our pH 5 samples at high T, we need to estimate the parameters Q, α, and ϕ_{p}. We calculated the number of AAc monomers in

subsection 2.6.7, finding the number of AAc monomers per particle, and therefore potential charged groups, is $(1.1 \pm 0.6) \times 10^8$. We use the p$K_a$ of AAc, 4.4, to estimate the fraction of AAc groups that are charged, finding that $Q_{\mathrm{pH}=5} = (9 \pm 5) \times 10^7$. It further follows from this that $\alpha \sim 0.192$ Finally, we can estimate $\phi_p = (R_{dry}/R_0)^3 \sim 0.011 \pm 0.004$. Taken together, we then obtain that at pH 5 and $T = 60$ °C, $r_0 = 0.40 \pm 0.04$ nm and $s = 0.17 \pm 0.03 < 1$.

Estimating t is not possible without knowing the value of B_3. However, for a poor solvent, $t < 0$. Because of the pronounced deswelling observed for the microgels at pH 5 at high T, we are confident that this is the case. Our particles are therefore in either Region VI or VII, indicating either large concentration fluctuations or a microphase separation of the polymer. We further note that because unlike the macrogel systems for which the theory was developed, the distribution of crosslinker is not homogeneous throughout our particles. In particular, the values of R_g/R_h we obtained indicate that ϕ_p is substantially higher in the particle core than the periphery at high T. This means that for a given (high) T, both s and t are higher at the periphery than the center. We therefore expect the solvent quality to effectively increase towards the particle periphery relative to the core. This predicts the exact behavior observed in our DLS measurements, namely that the core is small and dense relative to the rest of the polymer.

4.4 Form Factors at Smaller Length Scales

As with the pH 3 suspensions studied in Chapter III, we turn to SANS to gain information about the particle structure at very small length scales to validate our reasoning. The measurement and fitting procedures are identical to that described previously, and the fits to Eq. 2.33 with $\mu = 1.75 \pm 0.25$ are shown in Fig. 4.2a. Particularly with the highest-T data, it is clear that the decay is moving to higher q, indicating that the internal length scale of the particle is shrinking. As with the pH 3 case discussed in Chapter III, he decrease in ξ from the fits exactly mirrors the decrease in R_g/R_h obtained from dilute SLS and DLS measurements, as shown in Fig. 4.3a. This seems to confirm that the same mechanism is responsible for both observations. Further, as shown in Fig. 4.3b, R_g and $\langle R_{core} \rangle$, obtained from dilute SLS measurements, track each other closely as well. As we noted previously,

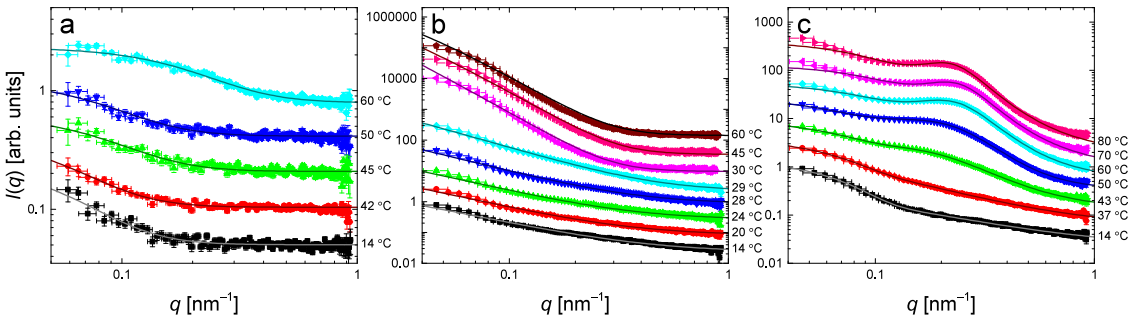

Figure 4.2: $P(q)$ measured with SANS for (a) NIPAM/pEG-d/AAc microgels at pH 5, (b) ULC microgels at pH 3.1, and (c) ULC microgels at pH 7.4. The measurement temperatures are shown to the right of each graph. Lines are fits to Eq. 2.33 in panels (a) and (b) and to Eq. 4.6 in panel (c). The data have been vertically offset for clarity.

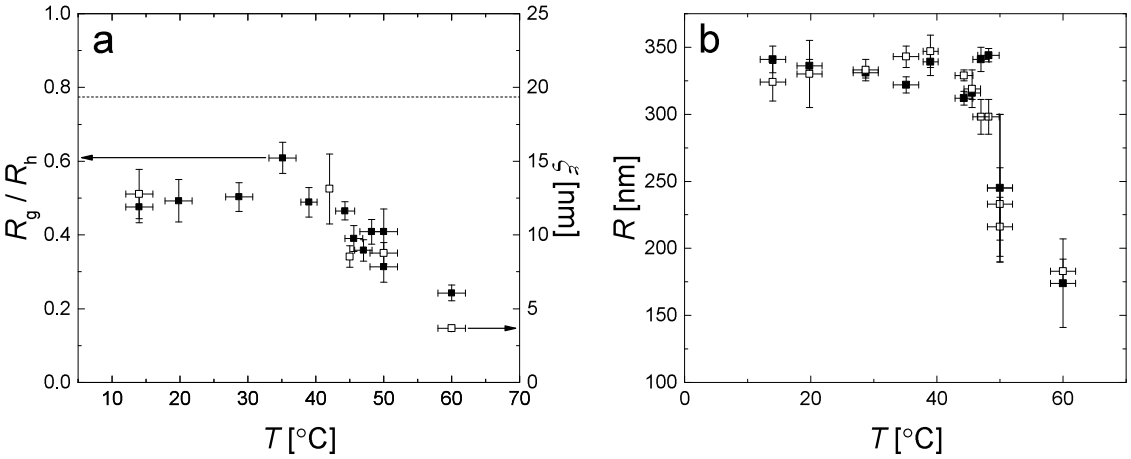

Figure 4.3: (a) R_g/R_h (filled squares), obtained from dilute SLS and DLS measurments, and ξ (open squares), obtained from SANS measurements, of crosslinked microgels at pH 5 for various temperatures. R_g/R_h follows the left y-axis, and ξ the right y-axis. The value of R_g/R_h for homogeneous spheres, $\sqrt{3/5} \sim 0.775$, is shown as a dashed line for comparison. (b) $\langle R_{core} \rangle$ (filled squares) and R_g (open squares), obtained from dilute SLS measurements, of the same microgels.

the applicability of Eq. 2.44 to these microgels at pH 5 and high T is debatable, but the similarity of the two radii implies that the small, dense core contains most of the mass of the particle and is therefore responsible for the small value of R_g/R_h.

We also attempt to complement this analysis of the SANS data with a fit to a scattering theory developed following the concepts discussed in section 4.3. According to this theory, the scattered intensity at high q should have the form [142, 143]

$$I(q) = \frac{I_1}{x^2 + t + 1/(x^2 + s)} + I_0, \tag{4.6}$$

where $x = qr_0$ and I_0 represents the background scattering. This function has one maximum at $q_{peak} = \sqrt{r_0^{-2} - \kappa^2}$, which describes a characteristic length scale between concentration fluctuations given by $2\pi/q_{peak}$. We are unable to successfully fit our high-T data with this model, but this is not surprising: from our calculated values of r_0 and κ at $T = 60$ °C, we estimate $q_{peak} \approx 2.3$ nm^{-1} and $2\pi/q_{peak} \approx 2.74$ nm. This estimated q_{peak} is outside the available range of the SANS instrument, and well into the region in which the background dominates the scattering in any event. This length scale, however, does agree very well with the length scale obtained from the fit to Eq. 2.33, $\xi = 3.7 \pm 0.1$ nm. Because the core is denser and therefore scatters much more than the periphery, this length scale will correspond to the polymer mesh in the core, consistent with our analysis.

As a check, we perform identical SANS experiments on microgels whose scattering behavior should be well-described by this theory. These are ultra-low-crosslinker (ULC) microgels [147], synthesized without added crosslinker. The polymer chains are "crosslinked" by rare chain-transfer reactions [148, 149]. These microgels have 5 mol% AAc and 95 mol% NIPAM.

We find that these microgels have a very homogeneous distribution of polymer. $P(q)$, measured by SLS, is shown in Fig. 4.4 for the ULC microgels for both neutral and charged AAc groups. In both cases, the data, which we fit to Eqs. 2.31 and 2.40, indicates that the distribution of polymer is homogeneous throughout the microgel. This is particularly clear for the low-pH case, whose deep minima also indicate size polydispersity $< 1\%$. The high-pH particles at higher T show a slightly higher polydispersity, between 4–5 %. We expect

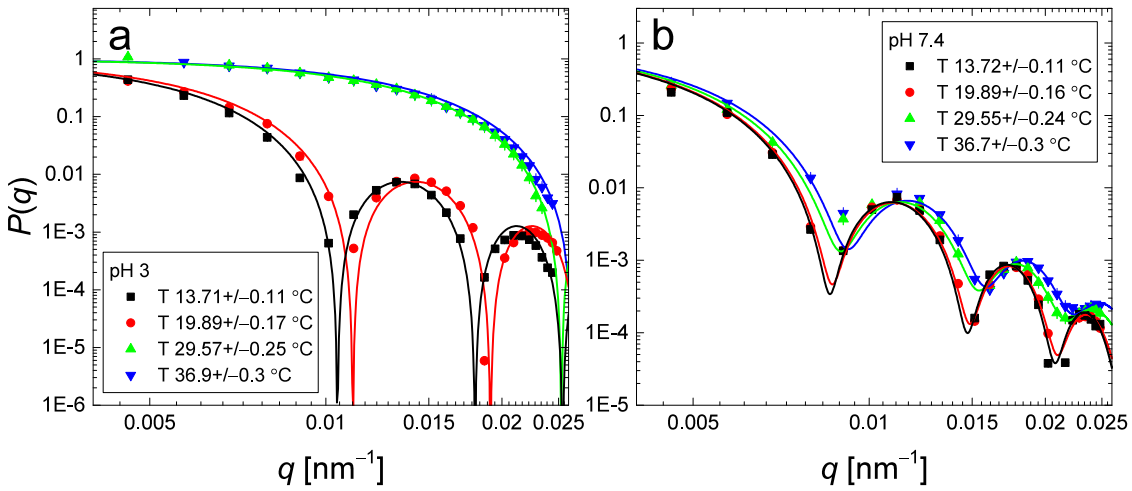

Figure 4.4: $P(q)$, measured by SLS, for suspensions of ULC microgels at (a) pH 3.1 and (b) pH 7.4. Lines are fits to Eqs. 2.31 and 2.40.

the scattering of these particles, measured with SANS, to correspond well to the macrogel theory, since the length scales probed by SANS are small enough that the homogeneous polymer network should be indistinguishable from a macrogel.

This is the case. Figs. 4.2b and c show the SANS data for the ULC particles in the neutral and ionized cases, respectively. In the neutral case, we obtain results that are qualitatively similar to the low-T measurements in Chapter III, without reproducing the heterogeneity-induced scattering at higher temperatures, which is unsurprising given both the substantially lower AAc content and the lack of crosslinker. $\mu = 1$ for $T < 30$ °C and $\mu = 2$ for $T \geqslant 30$ °C. When the AAc is completely ionized, however, we in fact do see the scattering maximum predicted by the theory, which becomes more pronounced as T increases and the solvent quality drops. Our fits give $r_0 \sim \kappa^{-1} \sim$ 1–3 nm, $t \sim -1$, and $s \sim 1$. These measurements, for $T \geqslant 43$ °C, are shown on the state diagram in Fig. 4.1, with higher-T measurements moving to slightly lower t and s values. We find that these measurements were performed right on the spinodal line between Regions VI and VII, where the system is highly unstable and possibly microphase-separated.

Because we are unable to calculate t for our crosslinked microgels at pH 5, we cannot directly compare the two systems. However, as discussed in section 4.3, the crosslinked microgels should lie in either Region VI or VII as well. A schematic of our crosslinked

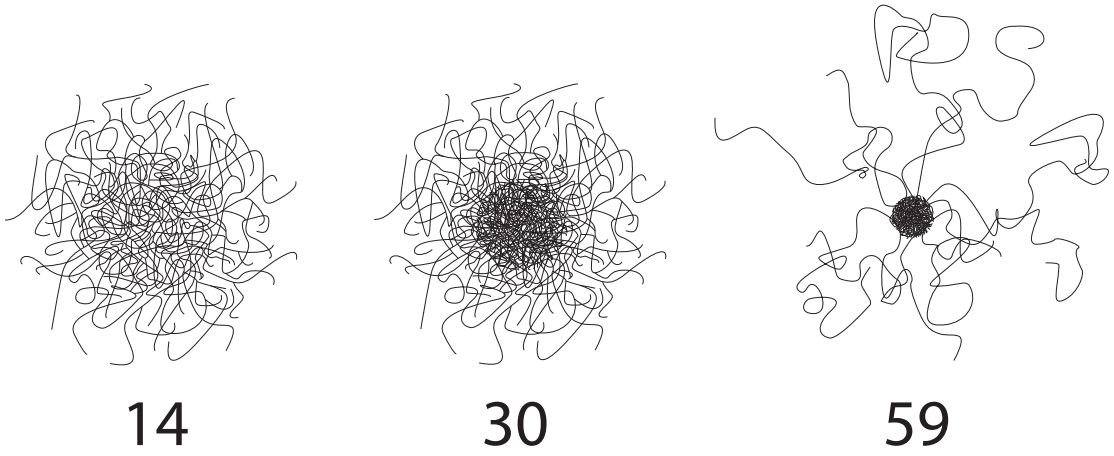

Figure 4.5: Representative schematic of the microgel conformational changes for our crosslinked microgels at several different T (labeled in °C) at pH 5.

microgels at pH 5 is shown in Fig. 4.5 for several T. At low T, the microgels assume the usual core-shell confirmation, as shown by the SLS data in Fig. 2.16b. At high T, however, the competition between hydrophobic deswelling due to the pNIPAM and the entropic cost of charge localization has the effect of densifying the core while allowing the periphery to remain solvated, leading to the extremely low values of R_g/R_h originally measured. The data shown in Fig. 4.3b support this conclusion.

4.5 Conclusion

We have obesrved an extreme core-shell microgel architecture showing R_g/R_h values, measured with light scattering, much lower than have been hitherto reported in the literature, and further having the unusual behavior of decreasing rather than increasing at higher temperature. We explain this behavior as being due to a nearly-balanced competition between the high-T hydrophobic deswelling tendency of the pNIPAM and the increasing entropic cost of charge localization the polymer must pay to deswell. Further, due to higher crosslinker density near the particle center, both the solvent quality and charge concentration increase towards the particle periphery. As a result, the internal structure of the microgel is separated into two regions: a dense, collapsed, mostly ucharged core, and a charged, swollen periphery. We were only able to obtain indirect evidence of this phenomenon in the studied microgels at pH 5 with SLS and SANS, due to high neutron scattering background and

a limited available q range. An additional complication was present in that the microgels do not have a homogeneous polymer distribution and the relevant theory was developed for homogeneous macrogels. However, we did directly observe the behavior predicted by the theory in SANS measurements of homogeneous microgels, synthesized without added crosslinker, and prepared in analogous conditions. Because the two sets of microgels are close to one another in the state diagram given by the theory, we conclude that the same physics is responsible for the unusual behavior observed in the crosslinked microgels.

CHAPTER V

AVOIDING THE GLASS TRANSITION IN CONCENTRATED SUSPENSIONS OF SOFT IONIC MICROGELS

5.1 Introduction

We combine static and dynamic measurements to investigate suspensions of ionized microgels at high concentrations where we expect the onset of a rigid, glassy state. Such a transition at high particle concentration is observed in systems of particles with widely varying properties: hard spheres [9, 29, 30, 39, 40, 150, 151], emulsions [152, 153] and foams [154, 155], star polymers [26, 33, 156–159] and linear polymer chains [11], and charged [54, 55, 64, 160] and uncharged [45, 89, 161–169] microgels. Typically, the approach to this glassy state follows analogously to molecular glassforming liquids. At low concentrations, the system is a simple liquid. At higher concentrations, the system's dynamics slow and the single characteristic timescale due to diffusion splits into a short and a long timescale, t_β and t_α, or the beta and alpha relaxation times, respectively [18, 21, 25, 170, 171]. The beta relaxation is associated to the thermal motion of a particle around its center of mass in the volume of a "cage" formed by its nearest neighbors; the alpha relaxation, to the escape of the particle from that cage due to structural rearrangement of the particles. At higher concentrations still, the particles are eventually unable to escape these cages and the system becomes a glass; finally, as the concentration becomes high enough that the particles are forced into contact, thermal motion effectively ceases and the system becomes jammed [22]. It is important to note that these are all non-equilibrium phenomena; in equilibrium, the state of the system is uniquely determined by the relevant thermodynamic variables, and the transition proceeds from liquid to crystal at the freezing point. However, often the system is unable to reach its equilibrium configuration on the experimental timescale and it is trapped in a metastable nonequilibrium state such as a supercooled liquid or glass. We do not observe an equilibrium liquid-to-solid transition in any of our experiments, and so

we consider our results only in light of these non-equilibrium concepts.

Despite the generality of these phenomena, the specifics of how and when the systems discussed above approach a glassy state vary widely depending on the specific properties of the glassforming particles. Hard spheres can neither compress nor deform, and have sharply-defined surfaces. Emulsions are incompressible, and the interactions of both emulsions and foams are mediated by the surface tension of the interstitial liquid. Linear and star polymers can interpenetrate, but linear polymers of different lengths and stiffness, and star polymers with varying functionalities and chain properties, interact very differently. Microgels can compress (changing volume), deform (changing shape), and interpenetrate, but the details of their interactions are governed by the chemistry of the monomer and crosslinker used in the synthesis, the amount and distribution of the crosslinker, and the conditions of the suspension, such as charge or salt concentration. Because of the difficulty in properly accounting for these different properties in any study of colloidal glassformers, they are often grouped under the umbrella term "softness" and not explicitly considered, and as a result the impact of different types of particle "softness" on the properties of the glass are not well understood. The goal of this Chapter is to elucidate at least some specific details about the origin and effects of "softness" by carefully studying the dynamics if dense suspensions of our microgels at different swelling conditions and charge concentrations, governed by pH and T.

The specific conditions studied are pH 5 and pH 6.5, both at $T = 14$ °C. SLS measurements of the structure factor confirm that the sample becomes somewhat more ordered, with a well-defined characteristic center-to-center distance emerging at higher ζ as particles are confined and surrounded by a shell of nearest neighbors. The center-to-center distance between particles also decreases below twice the dilute particle radius, indicating substantial deswelling. DLS and rheology measurements give us a way to measure the alpha relaxation times t_α that correspond to particle rearrangement.

At intermediate concentrations, we observe a sharp increase in t_α reminiscent of a Vogel-Fulcher-Tamann glass transition, in which t_α diverges at a finite concentration. Surprisingly, measurements at higher concentrations show that the system does not truly become

a glass. Instead, t_α saturates above a certain ζ. We interpret this as being due to a combination of the particles' softness (in the context of their bulk elastic modulus) and ion-driven deswelling, caused by an increase in the suspension osmotic pressure due to unbound counterions in the solvent.

5.2 Structure Factor Measurements

We estimate $S_{\mathrm{M}}(q)$ as described in Section 2.5 with an additional step to correct for the changes in $P(q)$ observed to occur at high ζ [89]. This correction was developed for a different system of core-shell microgel particles, but it should be approximately correct for any system of soft microgels at ζ high enough that the particles' $P(q)$ will change. We emphasize that because we do not use the exact same particles, this is inexact, and our reported $S_{\mathrm{M}}(q)$ are therefore only estimates.

For measurements of $S_{\mathrm{M}}(q)$ made at $\zeta < 1$, we do not apply any change, and divide $\langle I^{(1)}(q)\rangle_{\mathrm{E}}$ by the model $P(q)$ plotted using the parameters measured for the particles in dilute conditions. For the pH 5 system, this corresponds to Eqs. 2.35 and 2.44 with $\langle R_{\mathrm{c}}\rangle =$ 341 nm, $\sigma_{\mathrm{surf}} = 99$ nm, $\sigma_{\mathrm{p}} = 0.065$, $\mu = 2$, and $\xi = 13$ nm. For the pH 6.5 system, this corresponds to Eqs. 2.35 and 2.46, with $\langle R_{\mathrm{g}}\rangle = 520$ nm, $\sigma_{\mathrm{p}} = 0.001$, $\mu = 1.94$, and $\xi = 193$. For measurements made at $\zeta > 1$, we use the same model function but scale $\langle R_{\mathrm{c}}\rangle \propto \zeta^{-0.105}$, $\sigma_{\mathrm{surf}} \propto \zeta^{-0.82}$, and $\langle R_{\mathrm{g}}\rangle \propto \zeta^{-0.271}$. All other parameters are left unchanged. These scaling parameters are taken from the results of [89], which were measured for concentrated suspensions of neutral core-shell pNIPAM microgels crosslinked with bis-acrylamide. This admittedly ad hoc approach has several potential shortcomings:

To begin with, the true scaling of our particles with ζ almost certainly is not the same as in [89]. At pH 5, our particles are core-shell, but the length scales $\langle R_{\mathrm{c}}\rangle$ and σ_{surf} are not the same and do not have the same ratio. We also use a different crosslinker, and its distribution throughout the particles is likely to be different. Finally, our microgels are charged, and this is likely to play a significant role in determining the change in $P(q)$ at high ζ. These considerations are all true in the pH 6.5 case as well, and additionally at those conditions the particles are not even core-shell in dilute conditions; we scale $\langle R_{\mathrm{g}}\rangle$ according to the same

ζ-dependence as the overall particle size in [89]. Finally, [89] concluded that $P(q)$ changes significantly only for $\zeta > 1$, which may not be strictly true, especially since our system is charged and is likely to incorporate interparticle interactions with longer range than if they were neutral. Despite these caveats, however, the basic results of [89] should hold: namely, (i) for low enough ζ, $P(q)$ will not change, (ii) above some critical ζ of order 1, $P(q)$ will change, and (iii) the characteristic radius of the particles will change approximately as $\zeta^{-1/3}$, which will result in predictable changes to $P(q)$. While the details may vary from the exact scaling parameters we use, this approach represents a good first-order correction to $P(q)$ with increasing ζ and, as we discuss below, leads to meaningful results.

Plots of the process showing the experimental $\langle I^{(1)}(q)\rangle_{\mathrm{E}}$, the model $P(q)$ scaled with ζ where appropriate, and the resulting estimated $S_{\mathrm{M}}(q)$ (collected under the umbrella term "scattering factors") are shown in Fig. 5.1 for the pH 5 samples and Fig. 5.2 for the pH 6.5 samples. We also plot the estimated $S_{\mathrm{M}}(q)$ for different ζ together for comparison purposes in Fig. 5.3.

Both sets of data share important similarities. Key is that the value of q_{peak}, increases with ζ for all measured ζ. This means that the center-to-center distance is decreasing as ζ increases. The exact value of q_{peak} has only a very weak dependence on the exact parameters used to plot the model $P(q)$, and is always very close to the peak of the experimental intensity in any event. We are therefore very confident in the accuracy of our measurements of q_{peak}.

We are less confident about some other features of the data, particularly regarding the pH 5 measurements. It is true that dividing by the dilute $P(q)$ for samples at higher concentrations leads to unphysical $S_{\mathrm{M}}(q)$. For example, at high concentrations, this results in a peak height that can be larger than 10, which is unphysical particularly given that the Hansen-Verlet criterion for the onset of crystallization of hard spheres is that the peak height exceeds 2.85 [172]; the criterion has also been shown to apply to the liquid-crystal transition of soft spheres [173]. An example, comparing $S_{\mathrm{M}}(q)$ obtained with and without scaling $P(q)$, is shown in Fig. 5.4. In contrast, our estimated corrections result in $S_{\mathrm{M}}(q_{\mathrm{peak}}) \leqslant 1$.

We also note that both the pH 5 and pH 6.5 $S_{\mathrm{M}}(q)$ have unusual forms that we do not

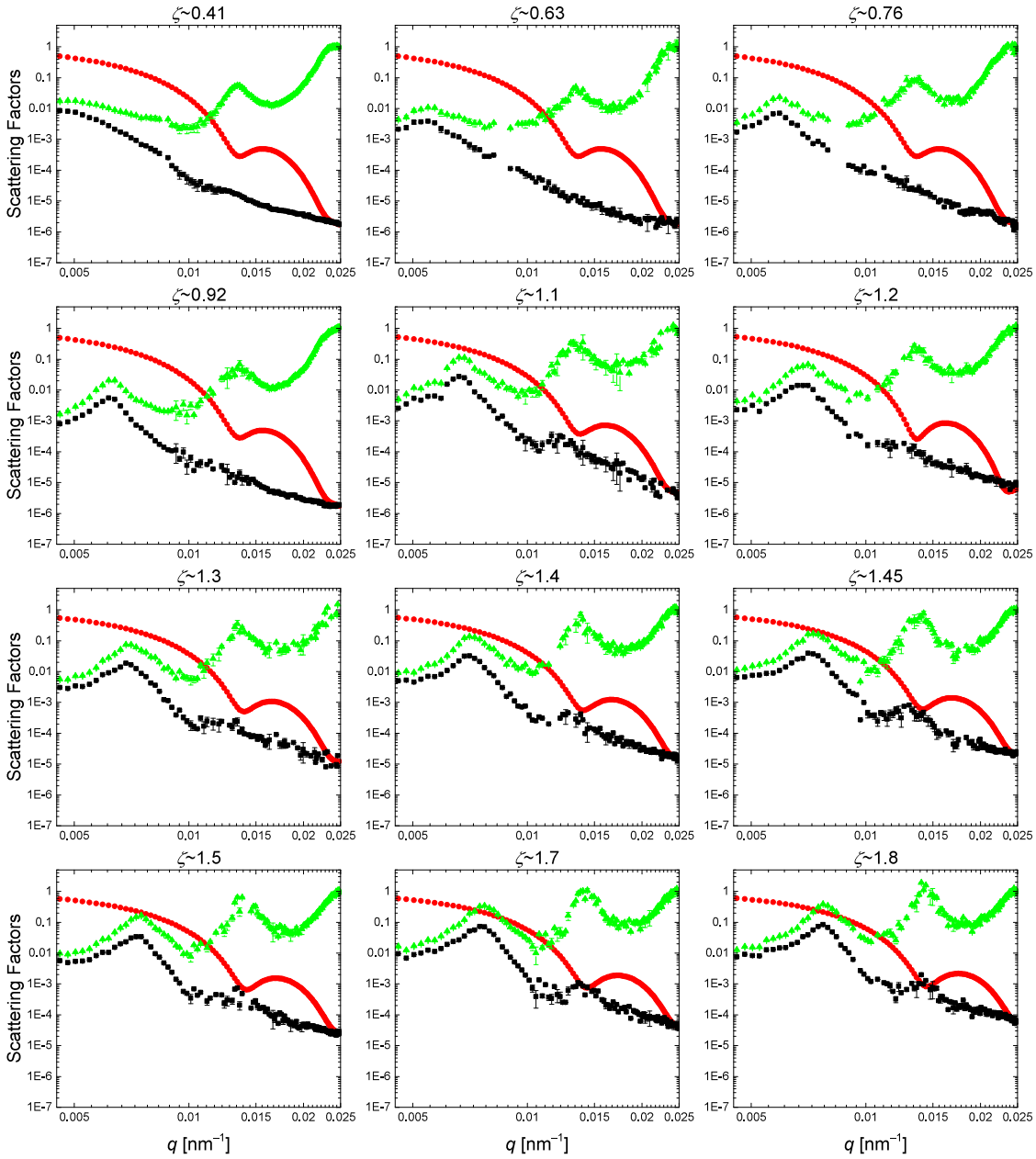

Figure 5.1: Experimental data and the estimated $S_{\mathrm{M}}(q)$ for concentrated microgel suspensions at pH 5. Black squares represent experimental $\langle I^{(1)}(q)\rangle_{\mathrm{E}}$, scaled down to $P(q)S_{\mathrm{M}}(q)$. Red circles represent the model $P(q)$ plotted as described in the text. Green triangles represent the estimated $S_{\mathrm{M}}(q)$. Each panel is labelled with the ζ of the measured suspension.

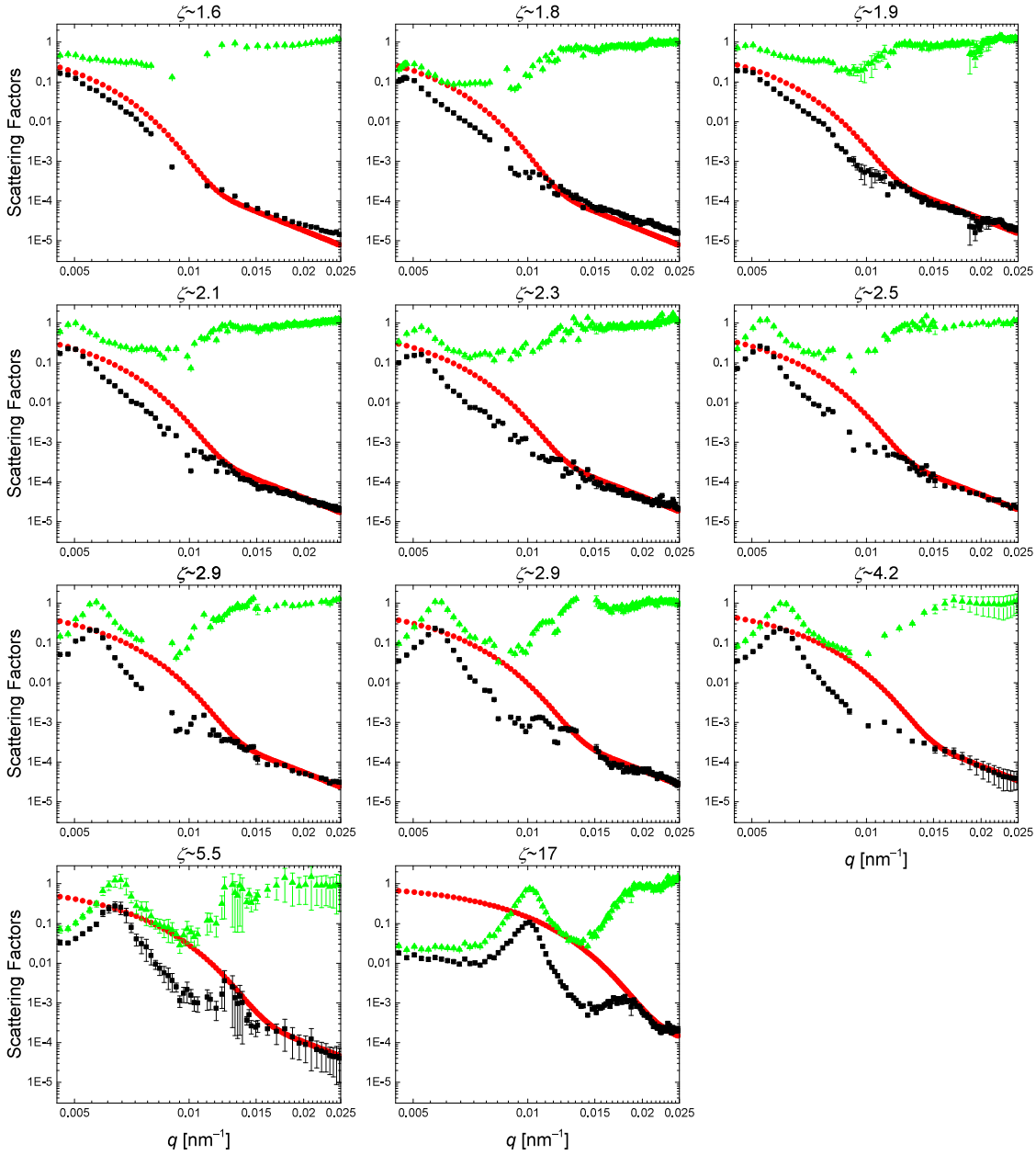

Figure 5.2: Experimental data and the estimated $S_{\mathrm{M}}(q)$ for concentrated microgel suspensions at pH 6.5. Black squares represent experimental $\langle I^{(1)}(q)\rangle_{\mathrm{E}}$, scaled down to $P(q)S_{\mathrm{M}}(q)$. Red circles represent the model $P(q)$ plotted as described in the text. Green triangles represent the estimated $S_{\mathrm{M}}(q)$. Each panel is labelled with the ζ of the measured suspension.

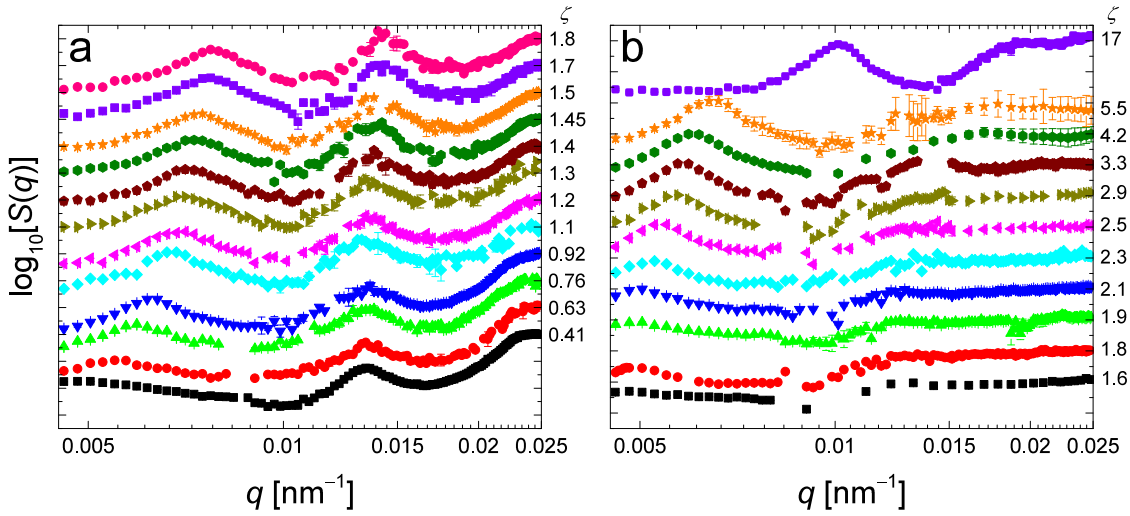

Figure 5.3: $S_{\mathrm{M}}(q)$ for different ζ for samples at (a) pH 5 and (b) pH 6.5. The plots in each panel have been offset vertically for clarity.

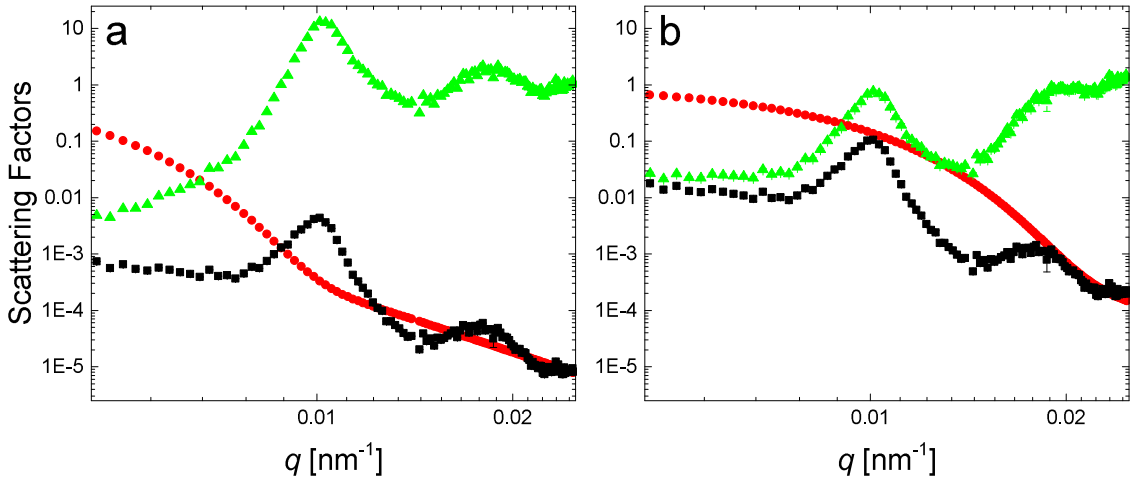

Figure 5.4: Obtaining $S_{\mathrm{M}}(q)$ from measured intensity data for pH 6.5, $\zeta = 17$, using (a) unscaled and (b) scaled $P(q)$. Black squares are $\langle I^{(1)}(q)\rangle_{\mathrm{E}}$ scaled to equal $P(q)S_{\mathrm{M}}(q)$, red circles are $P(q)$, and green triangles are $S_{\mathrm{M}}(q)$.

have a good way to model at all, although as we show in Fig. 5.4, the form of $S_{\mathrm{M}}(q)$ does depend on the exact scaling, or lack thereof, of $P(q)$. In most models, the first peak of $S_{\mathrm{M}}(q)$ should be higher than any other part, but we do not find this to be the case with our scaled $P(q)$. For the pH 5 samples, both the second visible peak and the high-q region are higher than $S_{\mathrm{M}}(q_{\mathrm{peak}})$ by factors of 10–100. The pH 6.5 samples show similar behavior, although the contrast is not as dramatic. Surprisingly, for both pH, at higher ζ, the height first peak increases to match the high-q value of $S_{\mathrm{M}}(q)$, although it does not exceed it for the measured samples. It is true that a low first peak in $S_{\mathrm{M}}(q)$ has been explained in terms of high particle polydispersity for simulations and experimental scattering studies of systems of hard spheres and emulsions [92, 93]. However, our measurements of the particles in dilute conditions suggest that their polydispersity is less than 10%, and while there is some evidence that the polydispersity of microgel suspensions can decrease as ζ increases [174], we are not aware of any results showing that polydispersity should *increase* with increasing ζ in a system of soft charged microgels similar to those we study. Measurements performed on other suspensions of soft microgel particles have observed the same behavior in $S_{\mathrm{M}}(q)$ [175], but an explanation is still lacking.

We are more confident in the qualitative features of $S_{\mathrm{M}}(q)$ for the pH 6.5 samples than the pH 5 samples. One reason is because for the pH 6.5 samples, at high q, the model $P(q)$ and the experimental $\langle I^{(1)}(q)\rangle_{\mathrm{E}}$ have the same q-dependence, which is unsurprising because $\lim_{q\to\infty} S_{\mathrm{M}}(q) = 1$ for a disordered system. This is because scattering at high q probes smaller length scales and therefore the interior of the particle, where the interparticle effects that contribute to the structure factor are less important. Aside from the surprisingly low value of $S_{\mathrm{M}}(q_{\mathrm{peak}})$ at low ζ, the qualitative shape of $S_{\mathrm{M}}(q)$ for the pH 6.5 samples is similar to previous measurements on star polymers [156, 176], in which only one peak was observed. In those experiments, $P(q)$ was not scaled with concentration before being divided out of the measured intensity to obtain $S_{\mathrm{M}}(q)$; thus, the reported peak heights ($S_{\mathrm{M}}(q_{\mathrm{peak}})$ between 1 and 5, depending on suspension concentration) are probably somewhat higher than the heights that would be obtained after taking particle compression into account.

Structure factors measured for concentrated solutions of star polymers have been theoretically predicted to show a first peak height lower than the high-q value as well (with $S_{\mathrm{M}}(q_{\mathrm{peak}})$ between about 0.5 and 1.2) [177–180]. However, while these microgels do have a scattering profile at pH 6.5 very similar to that of a star polymer (which is why we are able to use Eqs. 2.35 and 2.46 to describe the form factor), they are *not* star polymers. In particular, we do not expect them to interpenetrate as freely as star polymers in dense solutions. This is significant because the aforementioned prediction follows from the ability of the particles to interpenetrate. Specifically, once two stars begin to overlap, the energy cost they must pay to move closer is very small. Above the overlap concetration, therefore, two length scales come to describe a system of concentrated star polymers: a density-dependent length scale (the center-to-center distance) and a density-independent length scale (the star polymer size, which is mostly unchanged). Whenever the center-to-center distance has decreased enough such that it is an integer divisor of the star size, the first peak of the structure factor shrinks and eventually disappears. It is unclear whether or to what extent this mechanism can be blamed for our unusual measurements, given that even a small amount of crosslinker will make it more difficult for the particles to overlap significantly. Previous measurements on pNIPAM microgels have shown that interpenetration contributes very little to the decreasing center-to-center distance between particles as ζ increases [89].

The pH 5 samples present the same difficulties as those at pH 6.5, plus an additional one. Under certain conditions, $S_{\mathrm{M}}(q)$ for nanoemulsions has exhibited the same behavior as our pH 5 samples at low ζ, namely that there are multiple peaks, and the peak height increases with increasing q [93]. However, we note that, unlike the pH 6.5 case (in which only one peak exists and it clearly corresponds to a peak in intensity), the peaks observed in the pH 5 samples do not clearly share an origin.

The first structure factor peak, as in the pH 6.5 case, corresponds to a peak in the measured intensity, but the second peak does not do so as clearly. At q corresponding to the second peak in $S_{\mathrm{M}}(q)$, the intensity shows a slight peak in some measurements, but Fig. 5.1 makes it clear that the second peak also corresponds to the minimum in the (scaled)

$P(q)$. The same may be true of the apparent third peak at the highest measured q. In the same vein, the minima in $S_{\mathrm{M}}(q)$, except the first, are due to humps in $P(q)$ at least as much as they are due to minima in the intensity. It is difficult to say for sure that the procedure we employ to estimate $S_{\mathrm{M}}(q)$ completely corrects for the concentration dependence of $P(q)$. It is therefore possible that our scaling of $P(q)$ at high ζ fails to entirely capture the structural changes within the particles as they are concentrated. In particular, if the shape of $P(q)$ undergoes significant qualitative changes, the location, height, and even presence of the second and third peaks in $S_{\mathrm{M}}(q)$ will not be accurate. Our scaling of $P(q)$ is based on the results of measurements made on uncharged microgel suspensions [89], and it could be that the presence of charge will result in such changes at high ζ. This will not change the position of the first peak, since that is directly visible in the measured intensity and no change to the higher-q shape of $P(q)$ will cause the peak to move significantly in q.

Despite these uncertainties, however, these SLS measurements have successfully enabled us to calculate the center-to-center distance between particles, $2\pi/q_{\mathrm{peak}}$, as a function of ζ with a high degree of confidence. This is the same q we want to make our DLS measurements at [181], since relaxations at this length scale correspond to particle rearrangement. This is the topic of the next section.

5.3 Dynamic Light Scattering at the Peak Position

The structure of a glass is virtually indistinguishable from a snapshot of a liquid. Rather, a glass is distinguished from a liquid by its kinetic behavior. Specifically, the position of the center of mass of each particle that makes up the glass does not change in time, even though the particles may be allowed to vibrate around this position as a result of thermal fluctuations. In contrast, the particles in a liquid are not restricted, and can diffuse past one another freely.

In order to investigate our system's kinetic behavior, we perform 3DDLS measurements at the first peak of $S_{\mathrm{M}}(q)$. At low ζ, this is straightforward since the system relaxes on fairly short timescales, allowing us to look at the ensemble-averaged behavior of our system by simply performing a time average as discussed in Section. 2.4. However, as mentioned there

and covered in more detail in Appendix B, there is no simple way to convert a given time-averaged intensity cross-correlation function into an ensemble-averaged one. This means that at higher concentrations, when the dynamics of the system have slowed dramatically, long measurements are needed to obtain the appropriate statistics. The exact time required varies, but at the highest concentrations we performed three or more independent measurements, 48 hours long each, while rotating the cuvette 30° between measurements. These were then averaged together to obtain an approximate ensemble-averaged intensity cross-correlation function, $\langle (g_{\mathrm{I}}-1)/\beta \rangle_{\sim \mathrm{E}}$. (The criterion for determining the necessary measurement length was that all of the individual measurements produced roughly the same correlation function, and adding or removing one did not dramatically affect the resulting approximate ensemble-average.) We obtained the approximate ensemble-averaged electric field cross-correlation function by taking $\langle g_{\mathrm{E}} \rangle_{\mathrm{E}} = \sqrt{\langle (g_{\mathrm{I}}-1)/\beta \rangle_{\mathrm{E}}}$, and confirmed that in all cases this yields essentially the same result as taking $\langle g_{\mathrm{E}} \rangle_{\mathrm{E}} = \langle \sqrt{(g_{\mathrm{I}}-1)/\beta} \rangle_{\mathrm{E}}$. We plot the results for both the pH 5 and pH 6.5 experiments in Fig. 5.5. Because q_{peak} increases as ζ increases, the timescale of the measurements is due not only to the slowdown of the system, but also to the decrease of the length scale over which we are measuring the particle relaxation. To account for this, we plot the correlation functions against $q^2\tau$ in Fig. 5.5. We plot the cross-correlation functions of intensity rather than the electric field because taking the square root significantly increases noise at high τ when the value of the function is near zero. Note that the correlation functions of samples prepared at the lowest ζ display only a single decay. As ζ increases, not only does the decay move to the right, signifying a slowdown in the dynamics, but there is an additional decay, indicating that the sample becomes supercooled [170]. We fit the electric field correlation function to a sum of stretched exponentials following

$$g_{\mathrm{E}}(\tau) = A_1 \exp\left[-\left(\frac{\tau}{t_1}\right)^{\beta_1}\right] + A_2 \exp\left[-\left(\frac{\tau}{t_2}\right)^{\beta_2}\right], \tag{5.1}$$

where $A_1 + A_2 = 1$, t_1 and t_2 are fitting parameters related to the relaxation times, and β_1 and β_2 are the stretching exponents of the fit [182–185]. Example fits are shown in Figs. 5.5a and b. The timescale fitting parameters are related to the relaxation times t_α and t_β,

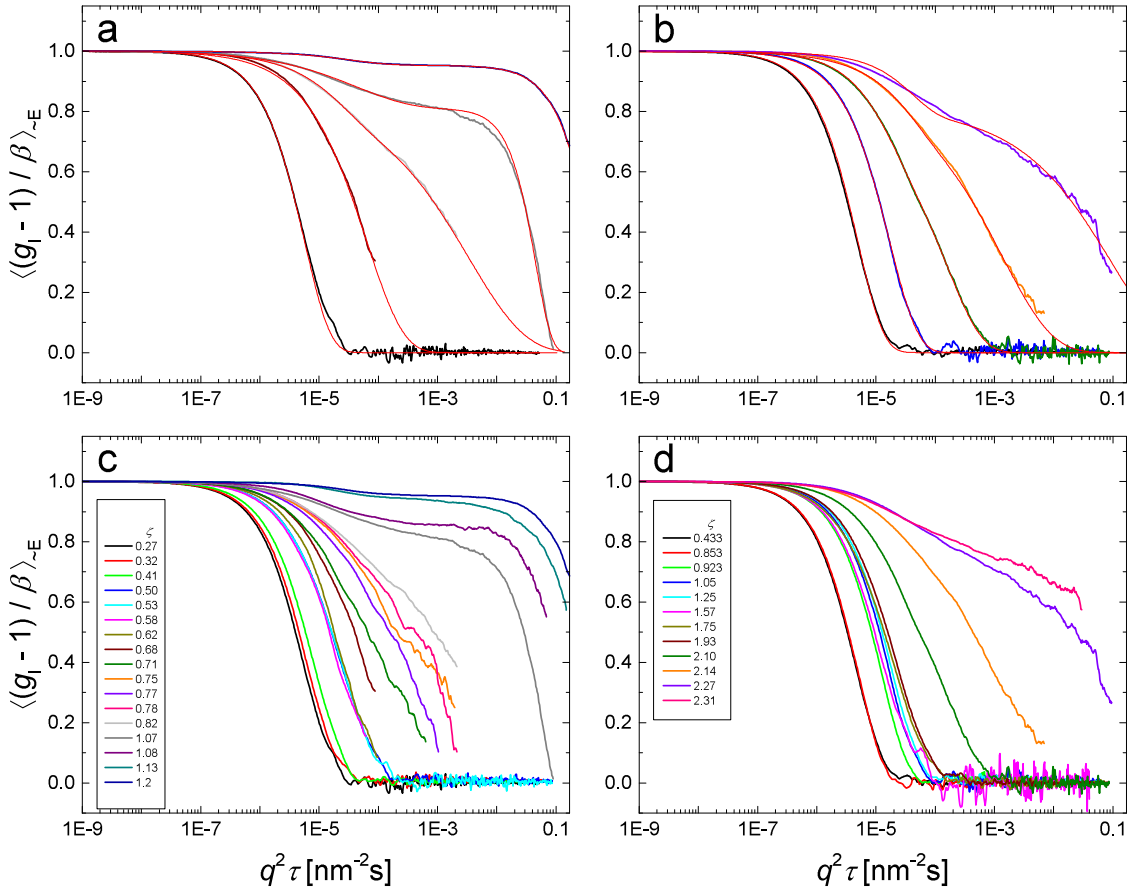

Figure 5.5: Normalized, ensemble-averaged intensity cross-correlation functions measured at q_{peak} and plotted vs. $q^2\tau$ for samples prepared at (a,c) pH 5 and (b,d) pH 6.5 for a wide range of different ζ. Panels (a) and (b) show example fits as thin red lines overlaid on the data; panels (b) and (d) show all experimental correlation functions, omitting the fits for the sake of clarity.

corresponding to the long-time structural relaxation of the particle's center of mass and the short-time motion of the particle around that center. Because the stretched exponential function represents a spectrum of exponential decays, we integrate over this spectrum to define the relaxation times as

$$\begin{aligned} t_{\alpha(\beta)} &= \int_0^\infty \mathrm{d}\tau \exp\left[-\left(\frac{\tau}{t_{1(2)}}\right)^{\beta_{1(2)}}\right] \\ &= t_{1(2)}\Gamma\left(1+\frac{1}{\beta_{1(2)}}\right), \end{aligned} \tag{5.2}$$

where $\Gamma(x) = (x-1)!$ is the gamma function. Since $\Gamma(2) = 1$, a stretching exponent of 1 (corresponding to an simple exponential decay) gives the relaxation time directly. However, because $\Gamma(x)$ is close to 1 for x close to 1, $t_{\alpha(\beta)} \approx t_{1(2)} \times (0.5\text{–}2)$. We list the values of the fitted stretching exponents in Tables 5.1 and 5.2, together with the values of $q = q_{\mathrm{peak}}$ where the measurements were made, as a function of ζ.

If the system truly does become a glass, we expect to see an emergent nondecaying component of the correlation function [39] in the form of a plateau at high τ as $t_\alpha \to \infty$; the height of this plateau would give us the fraction of the system that is "frozen" in a kinetically arrested state. However, as the plots of t_α and t_β in Fig. 5.6 show, our DLS measurements do not show such a "freezing out." t_α in both cases does increase dramatically in a narrow range of ζ, but, especially in the pH 5 case, we do not see conclusive evidence of such a divergence.

We fit the data to the empirical Vogel-Fulcher-Tamman equation, used to describe the relaxation of glassy systems [51–53], in an attempt to estimate the volume fraction, $\zeta = \zeta_0$, at which extrapolation from our low-ζ data predicts a diverging timescale:

$$t_\alpha = t_0 \exp\left(K\frac{\zeta}{\zeta_0 - \zeta}\right), \tag{5.3}$$

where t_0 is the relaxation timescale in the dilute limit and K a parameter that describes the fragility of the glassformer, a measure of how gradually t_α increases with ζ [43]. The VFT equation was originally developed for molecular glassformers, in which the relevant thermodynamic variable is temperature. In a colloidal glassforming system, that role is filled instead by ϕ, represented in our analysis by ζ. Written in the above form, the VFT

Table 5.1: ζ, q_{peak}, β_1, and β_2 for concentrated suspensions at pH 5. Some samples exhibit only a single decay. $\beta = 1$ corresponds to diffusive behavior. Some values of q_{peak} are repeated because the resolution of the goniometer, 1 °, was not small enough to differentiate between the q_{peak} change with small changes in ζ.

ζ	q_{peak} [nm^{-1}]	β_1	β_2
0.27	3.9×10^{-3}	1	
0.32	4.1×10^{-3}	0.946 ± 0.004	
0.41	4.6×10^{-3}	0.940 ± 0.004	
0.50	5.0×10^{-3}	1	
0.53	5.0×10^{-3}	1.1 ± 0.3	0.896 ± 0.017
0.58	5.0×10^{-3}	0.776 ± 0.002	
0.62	5.3×10^{-3}	0.831 ± 0.002	
0.68	5.5×10^{-3}	0.701 ± 0.002	
0.71	5.5×10^{-3}	0.609 ± 0.005	0.663 ± 0.004
0.75	5.7×10^{-3}	2.2 ± 0.1	0.676 ± 0.007
0.77	5.7×10^{-3}	1.58 ± 0.05	2.49 ± 1.04
0.78	5.9×10^{-3}	0.64 ± 0.03	0.861 ± 0.023
0.82	5.9×10^{-3}	0.454 ± 0.005	0.854 ± 0.022
0.84	5.9×10^{-3}	0.69 ± 0.08	0.530 ± 0.005
0.89	6.2×10^{-3}	2.155 ± 0.009	0.435 ± 0.005
1.03	6.4×10^{-3}	1.188 ± 0.011	0.489 ± 0.013
1.07	6.4×10^{-3}	1.61 ± 0.01	0.613 ± 0.005
1.08	6.4×10^{-3}	1.267 ± 0.006	0.613 ± 0.005
1.19	6.8×10^{-3}	1.374 ± 0.002	0.557 ± 0.007
1.17	6.8×10^{-3}	1.900 ± 0.012	0.384 ± 0.012

equation can equally be used to describe colloidal glassformers [167].

Because of the difficulty in measuring t_α with DLS at high ζ—and to confirm the absence of a diverging timescale—we turn to rheology, as discussed in the next section, to determine t_α at higher ζ.

5.4 Rheology at High ζ

Broadly speaking, rheology concerns itself with the flow and deformation of matter. This expansive definition allows for a diverse family of possible experiments. In this section we discuss results from two types of shear rheology experiments: oscillatory and steady-state.

In a shear rheology experiment, we study the relationship between applied shear stress and the resulting shear. Fig. 5.7a provides a simplified schematic of the experiment. A force F is applied to one surface of the sample, which has surface area A, while the other

Table 5.2: ζ, q_{peak}, β_1, and β_2 for concentrated suspensions at pH 6.5. Some samples exhibit only a single decay. $\beta = 1$ corresponds to diffusive behavior. Some values of q_{peak} are repeated because the resolution of the goniometer, 1 °, was not small enough to differentiate between the q_{peak} change with small changes in ζ.

ζ	q_{peak} [nm^{-1}]	β_1	β_2
0.43	3.1×10^{-3}	1	
0.63	3.5×10^{-3}	1	
0.85	3.9×10^{-3}	1	
0.93	3.9×10^{-3}	0.94 ± 0.03	
1.05	4.1×10^{-3}	0.923 ± 0.014	
1.25	4.4×10^{-3}	0.914 ± 0.001	
1.57	4.8×10^{-3}	0.926 ± 0.019	1
1.75	4.8×10^{-3}	0.775 ± 0.004	1
1.93	4.8×10^{-3}	0.814 ± 0.005	1
2.02	5.0×10^{-3}	0.835 ± 0.012	1
2.10	5.0×10^{-3}	0.752 ± 0.002	1
2.14	5.0×10^{-3}	0.514 ± 0.003	1
2.18	5.3×10^{-3}	0.719 ± 0.006	1
2.22	5.3×10^{-3}	0.563 ± 0.003	1
2.27	5.3×10^{-3}	0.468 ± 0.007	1

surface is held fixed. The shear stress is given by the ratio $\sigma = F/A$. This stress causes the deformation of the sample, defined in terms of the strain $\gamma = \Delta x/h$, where h is the sample thickness and Δx is the deformation of the sheared sample.

We use a cone-plate geometry to measure our samples, illustrated in Fig. 5.7b. In this setup, the sample is confined between a conical tool and the loading plate; the tip of the cone is truncated to avoid contact with the plate. The tool is rotated through an angle ϕ as shown in the figure. Because the height of the cone and the distance from the axis of rotation are related through the cone angle θ, with $\tan\theta = h/r$, and the deformation at the top of the sample is given by $\Delta x = r\phi$, the strain is constant throughout the sample, with $\gamma = \phi/\tan\theta$. This means that the strain is constant throughout the sample. This is in contrast to the simpler plate-plate setup, in which the tool and plate are both flat, but the strain increases farther from the axis of rotation. Our tool has a diameter of 25 mm, a cone angle of $\theta = 2°$, and is roughened to avoid sample slip. Our rheometer, an Anton-Paar Physica MCR-501, imposes a stress and measures strain, but incorporates a

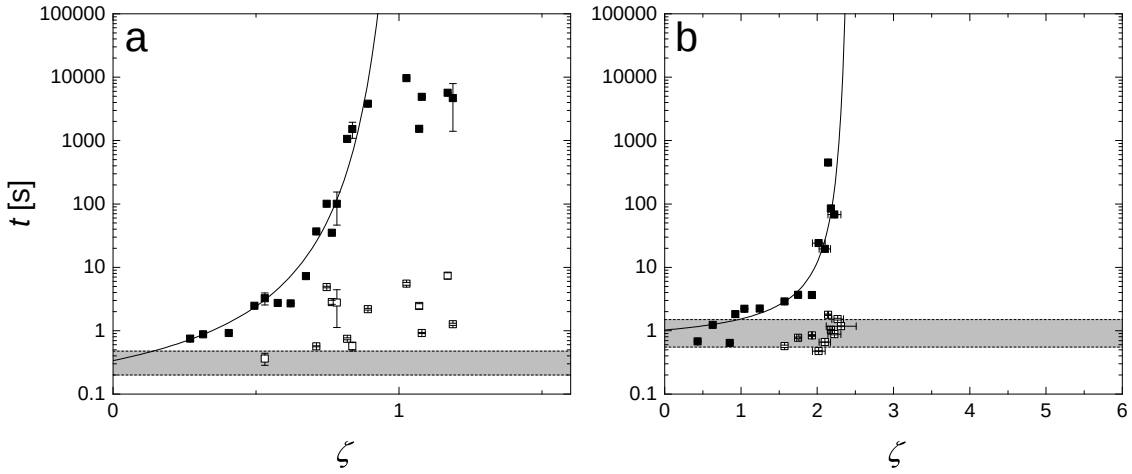

Figure 5.6: Plots of t_α (closed points) and t_β (open points) vs. ζ for samples prepared at (a) pH 5 and (b) pH 6.5, as measured by DLS at q_{peak}. The gray bar represents the diffusive timescale measured via DLS of dilute suspensions, and the black line a fit to Eq. 5.3. For the case of the pH 5 sample, we did not include the points at highest ζ, where t_α appears to level off, when performing the fit.

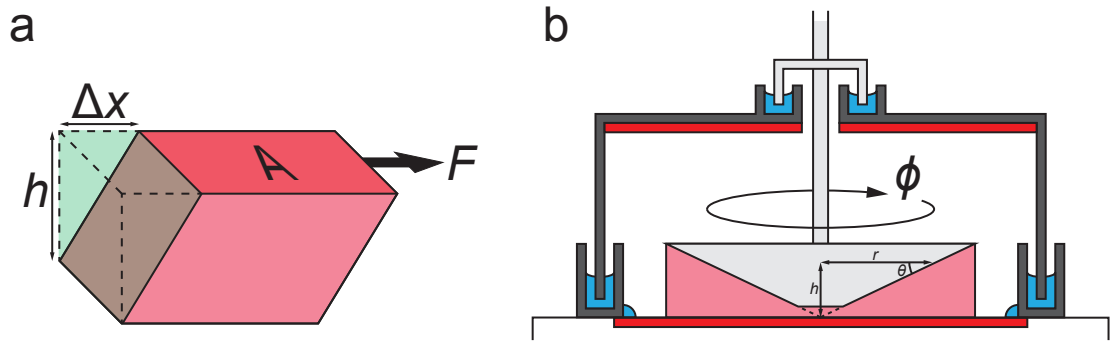

Figure 5.7: A schematic illustrating shear rheology. (a) A sample (red) with surface area A is subjected to a shearing force F and deforms as discussed in the text. The dashed outline represents the undeformed sample. (b) Our cone-plate setup. The sample (pink) is pressed between the conical tool (light gray) and the loading plate. The sample and tool are confined within an evaporation blocker (dark gray) that does not rotate. Troughs filled with water (blue) seal the system and prevent evaporation; an additional bead of water is placed around the circumference of the plate to saturate the air and help prevent evaporation. Temperature is controlled by two Peltier plates (red), one built into the plate and one into the evaporation blocker.

feedback loop in order to allow experiments with imposed strain. The response time of this feedback loop is ~ 1 ms. Because the shortest timescales in any of our measurements are at least a factor of 10 longer than this, we can perform our experiments with either imposed stress or effectively imposed strain, as desired.

We also control the temperature of our samples during the experiment. A Peltier temperature controller is built into the loading plate, and since the sample volume and thickness are on the order of 0.1 mL and 1 mm, respectively, temperature throughout the sample is constant throughout the measurement. An evaporation blocker with a second, built-in Peltier temperature controller protects the sample from water loss throughout the measurement and provides additional temperature stability.

Finally, the instrument is calibrated to account for various sources of error prior to each measurement. We account for noise due to (i) imperfections in the motor operation and (ii) turbulence in the high-pressure air bearing, by running the motor without coupling to the tool, as well as (iii) correcting for the effect of tool inertia on the measured stress, by measuring the moment of inertia of the tool prior to each measurement. As a last precaution, we follow established preshear protocols [26, 153, 169, 186] in order to erase any history dependence of the sample: we shear the sample at $\dot{\gamma} = 500$ s^{-1} for 60 s, then allow it to rest for 300 s before measuring. Tests on several samples showed that this allowed us to obtain reproducible results.

5.4.1 Oscillatory Rheology

In an oscillatory measurement [187], we apply a strain that varies in time according to $\gamma(t) = \gamma_0 \sin(\omega t)$, where γ_0 is the strain amplitude and ω the angular frequency, and measure the resulting shear stress. For small enough amplitudes, the stress will also be sinusoidal, but with a phase difference δ relative to the input strain. For a perfectly elastic solid, $\delta = 0$ (input and output are in phase) and the stress will go as $\sigma = G'\gamma$, where G' is the elastic modulus. For a perfectly viscous liquid with viscosity η, $\delta = \pi/2$ (input and output are out of phase), and the stress follows $\sigma = (G''/\omega)\dot{\gamma}$, where G'' is the viscous modulus and $\eta = G''/\omega$. A viscoelastic material is one in which both G' and G'' are nonzero and

$\delta \in (0, \pi/2)$.

Again, these definitions are only meaningful for small strain amplitudes. For larger amplitudes, the response is instead a sum of higher-order harmonic terms [188]. In this case δ, and therefore G' and G'', can no longer be meaningfully defined. We therefore perform all of our oscillatory measurements at low amplitudes. We perform preliminary measurements sweeping through γ while keeping ω constant, for each sample, as shown in Fig. 5.8a for one sample. For γ that are low enough, σ is a linear function of γ and G' and G'' are independent of γ. We note that the maximum γ for which the linear interpretation is valid may depend weakly on ω. To ensure that our measurements are accurate, we therefore set γ to be 90% of the one indicated by the plot when performing our frequency sweeps. Further, because we do not "reset" the sample history by preshearing after every point, the points after the system enters the nonlinear regime will be cumulatively affected by each preceding nonlinear point, leading to quantitative deviations from the "true" response. However, these differences are likely to be quite small, and in any event unimportant, since we are only concerned with finding the limits of the linear regime.

Oscillatory rheology frequency sweeps for a viscoelastic liquid have a characteristic shape that is extremely robust, and displayed by a wide variety of viscoelastic systems including microgel suspensions [40, 152, 188–190]. At low ω (long timescales), $G' \sim \omega^2$ and $G'' \sim \omega$, with $G'' > G'$, since any viscoelastic material will flow over long enough timescales. However, at higher ω, G' becomes higher than G'' and levels off, becoming nearly constant over many orders of magnitude of ω, and G'' peaks, then decreases. The moduli in this regime are exemplified in the simplest form by the Maxwell model [187]:

$$G'(\omega) = G'_{\mathrm{P}} \frac{x^2}{1+x^2}, \tag{5.4a}$$

$$G''(\omega) = G'_{\mathrm{P}} \frac{x}{1+x^2}, \tag{5.4b}$$

where $x = \omega/\omega_{\mathrm{crossover}}$, $\omega_{\mathrm{crossover}}$ is the frequency at which $G' = G''$ (and equivalently, $x = 1$), and G'_{P} is the high-ω plateau value of $G'(\omega)$. This crossover point gives the alpha relaxation of the system according to $t_\alpha = 2\pi/\omega_{\mathrm{crossover}}$. At higher frequencies (shorter

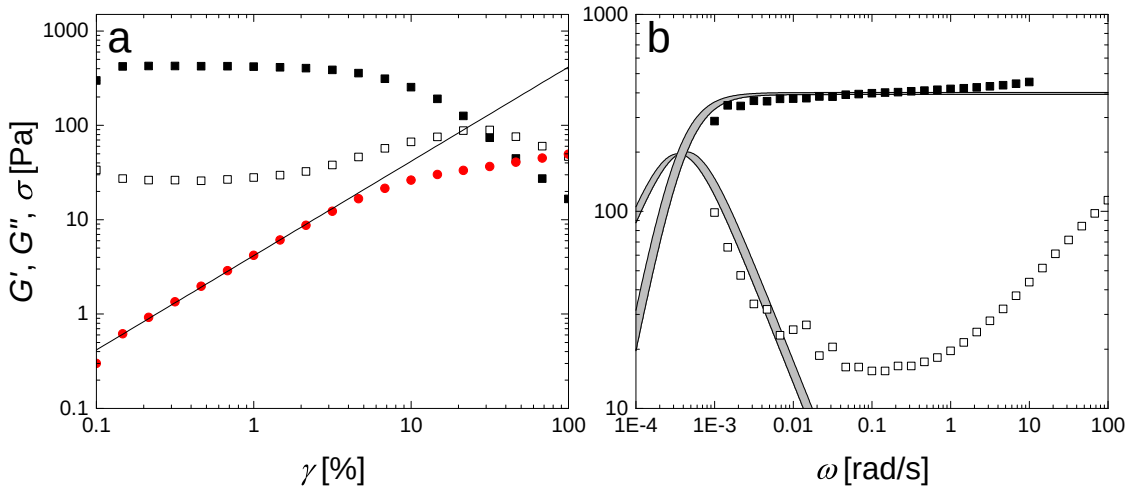

Figure 5.8: Oscillatory rheology of a pH 5 sample with concentration 1.7 wt%. (a) An example strain sweep. G' and G'' are the filled and open black squares, respectively, and the maximum shear stress for each point is shown by red circles. The black line shows a linear fit to the stress at low γ with slope G'; where this line fails to describe the data, the linear approximation is invalid. (b) An example frequency sweep together with fits to the Maxwell model at low ω. The filled and open squares represent G' and G'', respectively. The gray regions show the fit uncertainty; the uncertainty in relaxation time is given by their region of overlap.

timescales), the system is solid-like; on longer timescales, it is liquid-like, indicating rearrangement (structural relaxation) of the particles. At much higher ω still, viscous dissipation in the system is dominated by random slippage of the particles past one another, rather than affinely deforming without rearranging; this leads to G'' increasing again according to $G'' \sim \omega^{1/2}$ [191].

Our data follows these general trends, as shown in Figs. 5.8b and 5.9. However, as also shown in the figures, in most cases the $\omega_{\text{crossover}}$ does not lie within the experimentally accessible window. This crossover time, which we also observed in light scattering measurements for samples prepared at lower ζ, is the primary feature we are interested in. We can estimate the approximate crossover just by looking at the graphs, but to quantify it more carefully we fit the low-ω regions of the plots to the Maxwell model. To find the values of $\omega_{\text{crossover}}$ and G'_{P} that best fit both $G'(\omega)$ and $G''(\omega)$, we fit both data sets simultaneously. An example of this fit is shown in Fig. 5.8b. Uncertainty in the fit leads to uncertainty in the resulting value of $\omega_{\text{crossover}}$, but as shown in the figure this uncertainty (the range of ω

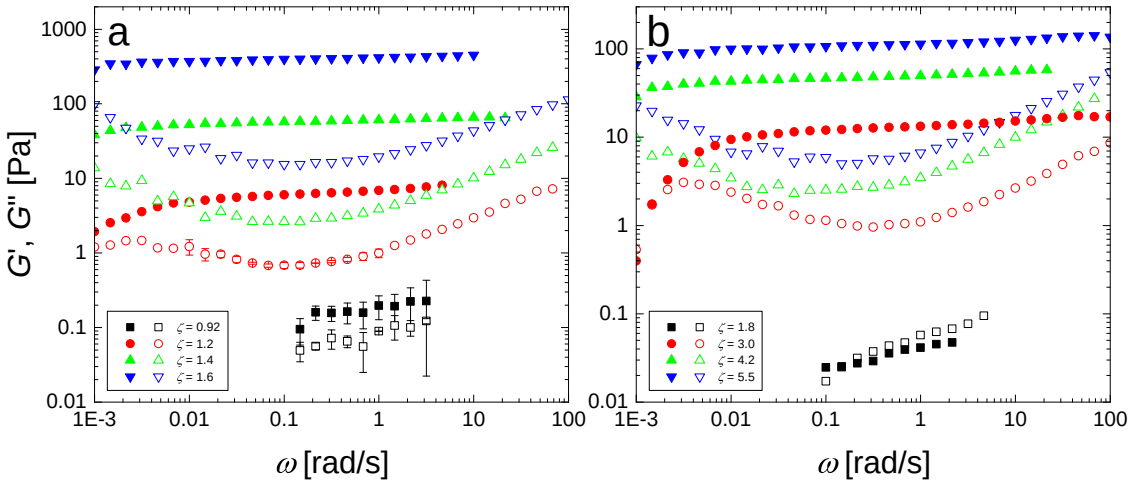

Figure 5.9: Oscillatory measurements for (a) pH 5 samples and (b) pH 6.5 samples at the values of ζ shown in the legend. We do not show points for which the measured torque was below the specifications of our device (20 nNm for oscillatory measurements), which are not reliable. Note that in a few cases (for example, the pH 6.5 sample prepared with $\zeta = 3.0$), the crossover is visible within the experimental window.

where the two fits overlap) is quite small. We note that Eqs. 5.4a and b are simplifications: in a real system, there will be a spectrum of relaxation times, analoguous to the stretched exponential function used to describe light scattering correlation functions. However, similarly to the simplification used in our DLS analysis, in which we integrate over this spectrum to obtain a single characteristic timescale, t_α, we perform this simple Maxwell model fit to estimate t_α from our oscillatory measurements. Because this model fits the data well and we primarily are concerned with obtaining t_α anyway, this fit is satisfactory. As we will see in the next Subsection, we obtain almost identical values of t_α from our steady-state measurements, validating this approach.

Oscillatory rheology frequency sweeps for our samples at both pH 5 and 6.5 are shown in Fig. 5.9 for a range of ζ. The values of t_α obtained from these measurements are shown in Fig. 5.10a as black squares. The observed relaxation times do not continue increasing with ζ as we would expect for a system undergoing a glass transition. In order to confirm the absence of a glassy state, we turn to steady-state rheology.

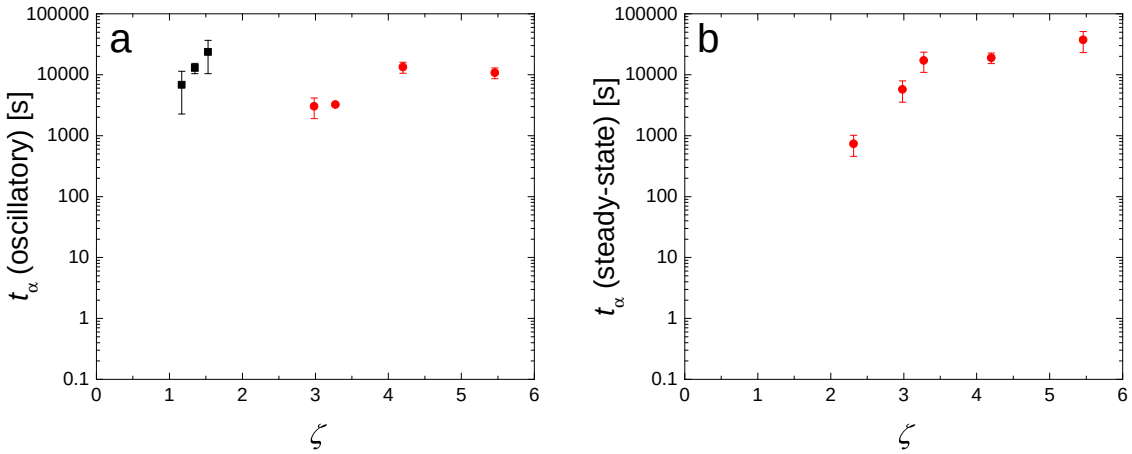

Figure 5.10: Values of t_α obtained from (a) oscillatory and (b) steady-state rheology, as discussed in the text, plotted on the same scale as in Fig. 5.6. Black squares are from the pH 5 samples (data only available for oscillatory measurements) and red circles from the pH 6.5 samples.

5.4.2 Steady-state Rheology

In a steady-state measurement, we apply a constant strain rate to each point and measure the resulting stress. For a simple Newtonian liquid, the stress required to shear the material is proportional to the shear rate, $\sigma = \eta_s \dot{\gamma}$, with η_s the viscosity of the liquid. Viscoelastic materials will have a more complex response. One possible behavior is the emergence of a yield stress, meaning that the system behaves as a solid unless a minimum stress is applied, above which it flows. The Herschel-Bulkley model, $\sigma = \sigma_{\text{yield}} + m\dot{\gamma}^n$ with σ_{yield} the minimum stress required to achieve flow and m and n fitting parameters, is commonly used to describe such a system [192]. Another possible deviation from Newtonian behavior is a viscosity that depends on $\dot{\gamma}$. This can be as simple as $\sigma = \eta(\dot{\gamma})\dot{\gamma}$; the Herschel-Bulkley model, for example, also exhibits this behavior at high $\dot{\gamma}$ for $n \neq 1$, but it is a general feature of non-Newtonian fluids.

In our experiments, shown in Fig. 5.11a, we observe a response that *resembles* that of a yield-stress material: at higher ζ, a plateau develops at low and intermediate $\dot{\gamma}$. However, at very low $\dot{\gamma}$, this plateau disappears, indicating that the sample *does* flow on long enough timescales. To verify that this behavior is not an artifact due to the measurement protocol, we perform several additional tests, shown in Fig. 5.11b, in which we confirm that imposing

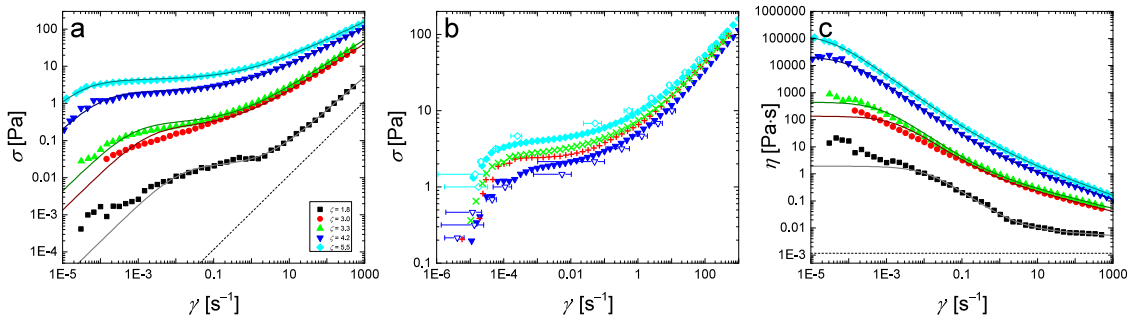

Figure 5.11: Flow curves for suspensions at pH 6.5. The raw stress-vs.-strain-rate curves are shown in (a) for different ζ. Solid lines are fits to Eqs. 5.5a and b, and the dashed line represents the viscous stress response of the solvent (water) at the measurement temperature. Note that at the lowest shear rates, the "apparent" yield stress, visible over several orders of magnitude in $\dot{\gamma}$ for the higher ζ, does continue to decrease. In (b), we show several tests performed to confirm that this behavior was not an artifact of the measurement protocol. Closed points reproduce the imposed-strain-rate measurements shown in (a), and open points, measurements in which we impose a stress and measure the resulting strain rate. We performed an additional test at $\zeta = 5.5$ with a smooth tool (red + symbols) to show that wall slip was not affecting the results. Finally, we performed a test at the same ζ in which we waited one hour (comparable to the entire measurement time) after preshearing the sample and before performing the measurement; these points are shown by green $\times$ symbols. In all cases the flow curves are virtually identical to the initial tests, validating our results. In panel (c), we show the shear-dependent viscosity obtained by dividing the stress in panel (a) by the strain rate at each point. The viscosity of water is shown as a dashed black line. Note the zero-shear-rate viscosity at the lowest $\dot{\gamma}$, corresponding to the downturn observed in the stress curves. In all cases, we neglect points with torque below the specifications of our device (100 nNm for steady-state measurements).

a stress and measuring the resulting strain rate gives the same results, and also that neither wall slip [193] nor waiting time after the preshear is responsible for our observations.

To understand our results, we fit the data to a semi-empirical model [23, 24] developed to describe the transition from a liquid to a glass, and from a glass to a jammed state. Reflecting a fairly well established consensus in the soft matter community [22, 194–204], this model treats the glass and jammed states separately. Both are disordered, nonequilibrium states that appear to share many similarities. The glassy state, however, is still thermalized, and the glassforming particles are able to vibrate around their center of mass. The rigidity of a glassy system is entropic in nature. The jammed state, in contrast, is athermal, appearing in macroscopic systems such as packings of marbles or sand, or in colloidal systems at low temperatures. Rigidity due to jamming emerges when the particles in the system

exceed the isostatic point. In three dimensions, this is when each particle has an average of 6 nearest neighbors, and the system becomes mechanically stable [205–207].

For a thermal system at high packing fractions, both glassy and jamming physics can determine the behavior of the system. One effect or the other may be dominant, depending on the interactions between particles, the temperature, and ϕ. For example, experimental studies of different colloidal suspensions have found that the behavior of hard polymer spheres and dry foams are dominated by glassy and jamming physics, respectively, while emulsions are sensitive to both mechanisms [23, 24]. The same experiments found that soft polymer microgels, undergo a glass transition and are strongly affected by thermal fluctuations, meaning that jamming does not play a significant part in their behavior.

This last point agrees with our findings. The model we use to describe our stress flow curves is given by

$$\sigma(\phi,\dot{\gamma},\epsilon,\phi_{\mathrm{G}},\phi_{\mathrm{J}}) = \sigma_{\mathrm{G}}(\phi,\dot{\gamma},\epsilon,\phi_{\mathrm{G}},\phi_{\mathrm{J}}) + \sigma_{\mathrm{J}}(\phi,\dot{\gamma},\epsilon,\phi_{\mathrm{J}}) + \eta_{\mathrm{s}}\dot{\gamma}, \tag{5.5a}$$

$$\sigma_{\mathrm{G}}(\phi,\dot{\gamma},\epsilon,\phi_{\mathrm{G}},\phi_{\mathrm{J}})/\sigma_{\mathrm{T}} = \sigma_{\mathrm{GY}}(\phi,\epsilon,\phi_{\mathrm{G}},\phi_{\mathrm{J}}) + \frac{Y_{\mathrm{G}}}{[\dot{\gamma}\tau_{\mathrm{T}}G(\phi,\phi_{\mathrm{G}})]^{-1} + [1+p_{\mathrm{G}}(\dot{\gamma}\tau_{\mathrm{T}})^{\alpha_{\mathrm{G}}}]^{-1}}, \tag{5.5b}$$

$$\sigma_{\mathrm{J}}(\phi,\dot{\gamma},\epsilon,\phi_{\mathrm{G}},\phi_{\mathrm{J}})/\sigma_0(\epsilon) = \sigma_{\mathrm{JY}}(\phi,\epsilon,\phi_{\mathrm{J}}) + \frac{Y_{\mathrm{J}}}{[\dot{\gamma}\tau_0(\epsilon)J(\phi,\phi_{\mathrm{J}})]^{-1} + [p_{\mathrm{J}}(\dot{\gamma}\tau_0)^{\alpha_{\mathrm{J}}}]^{-1}}. \tag{5.5c}$$

Here σ_{G} and σ_{J} are the glassy and jamming contributions to the shear stress, and $\eta_{\mathrm{s}}\dot{\gamma}$ is the contribution from the solvent. ϕ_{G} and ϕ_{J} are the volume fractions where the system undergoes the glass and jamming transitions. $\sigma_{\mathrm{T}} = k_{\mathrm{B}}T/R^3$ is the thermal stress scale of the particles and $\sigma_0(\epsilon) = \epsilon/R^3$ the stress scale set by the interaction strength of the particles, ϵ. Similarly, the timescale of thermal motion is given by $\tau_{\mathrm{T}} = 6\pi\eta_{\mathrm{s}}R^3/k_{\mathrm{B}}T$ and the timescale of energy dissipation due to interparticle interactions by $\tau_0 = \tau_{\mathrm{T}}(k_{\mathrm{B}}T/\epsilon)$.

σ_{GY} and σ_{JY} are functions proportional to the the yield stresses of the glass at ϕ_{G} and the jammed system at ϕ_{J}, respectively, given by

$$\sigma_{\mathrm{GY}}(\phi,\epsilon,\phi_{\mathrm{G}},\phi_{\mathrm{J}}) = \begin{cases} 0 & \phi < \phi_{\mathrm{G}} \\ \left[Y_{\mathrm{GJ}}^{-1}\sqrt{\frac{\sigma_{\mathrm{T}}}{\sigma_0(\epsilon)}} + Y_{\mathrm{G}}'^{-1}(\phi-\phi_{\mathrm{G}})^{-\beta_{\mathrm{G}}}(\phi-\phi_{\mathrm{J}})^{\beta_{\mathrm{GJ}}}\right]^{-1} & \phi_{\mathrm{G}} \leqslant \phi \leqslant \phi_{\mathrm{J}} \\ 0 & \phi_{\mathrm{J}} < \phi \end{cases} \tag{5.6}$$

and

$$\sigma_{\mathrm{JY}}(\phi,\epsilon,\phi_{\mathrm{J}}) = \begin{cases} 0 & \phi < \phi_{\mathrm{J}} \\ Y_{\mathrm{GJ}}\sqrt{\frac{\sigma_{\mathrm{T}}}{\sigma_0(\epsilon)}} + Y_{\mathrm{J}}(\phi-\phi_{\mathrm{J}})^{\beta_{\mathrm{J}}} & \phi_{\mathrm{J}} \leqslant \phi \end{cases} . \tag{5.7}$$

Finally, $G(\phi,\phi_{\mathrm{G}})$ and $J(\phi,\phi_{\mathrm{J}})$ are functions that describe the increasing relaxation times of the samples with increasing ϕ. These functions are given by

$$G(\phi,\phi_{\mathrm{G}}) = \begin{cases} h_{\mathrm{G}}(\phi_{\mathrm{G}}-\phi)^{-\gamma_{\mathrm{G}}} & \phi < \phi_{\mathrm{G}} \\ \infty & \phi_{\mathrm{G}} \leqslant \phi \end{cases} \tag{5.8}$$

and

$$J(\phi,\phi_{\mathrm{J}}) = \begin{cases} h_{\mathrm{J}}(\phi_{\mathrm{J}}-\phi)^{-\gamma_{\mathrm{J}}} & \phi < \phi_{\mathrm{J}} \\ \infty & \phi_{\mathrm{J}} \leqslant \phi \end{cases} . \tag{5.9}$$

Y_{G}, Y_{J}, Y_{GJ}, Y'_{G}, p_{G}, p_{J}, α_{G}, α_{J}, β_{G}, β_{GJ}, β_{J}, h_{G}, h_{J}, γ_{G}, and γ_{J} are all fitting parameters. We plot some possible curves described by this model in Fig. 5.12 to illustrate the differences in different regions of ϕ. Specifically, note that in the region $\phi < \phi_{\mathrm{G}}$, the "apparent" yield stress fails at low $\dot{\gamma}$, as seen in our measurements, while for $\phi > \phi_{\mathrm{G}}$, a true yield stress exists. This is due to the difference between the denominators in the second terms of Eqs. 5.5b and 5.5c. The pre-glassy region is characterized by the presence of this "apparent" yield stress, which becomes more and more like a true yield stress as ϕ approaches ϕ_{G}. The key difference between the glassy and jammed states is that for a glass, the important stress scale is σ_{T}, and for a jammed state, it is σ_0, as mentioned above. One consequence of this is that the detailed behavior of the glassy state, where the particles are still thermalized, should be relatively independent of specific properties of the particles, while the behavior of the jammed state should depend much more on the interparticle interactions. (As we will show by the end of this Chapter, this is not strictly speaking true, if the particle properties change with ζ.)

We find that the jamming term is not needed to fit our data, and in fact cannot be meaningfully included because it presupposes a yield stress. Since our samples do not have a true yield stress, including the jamming term would require that its magnitude be very small compared to the other terms, overparameterizing the fit without contributing additional information. Thus, we use only the first and third terms in Eq. 5.5a. We also

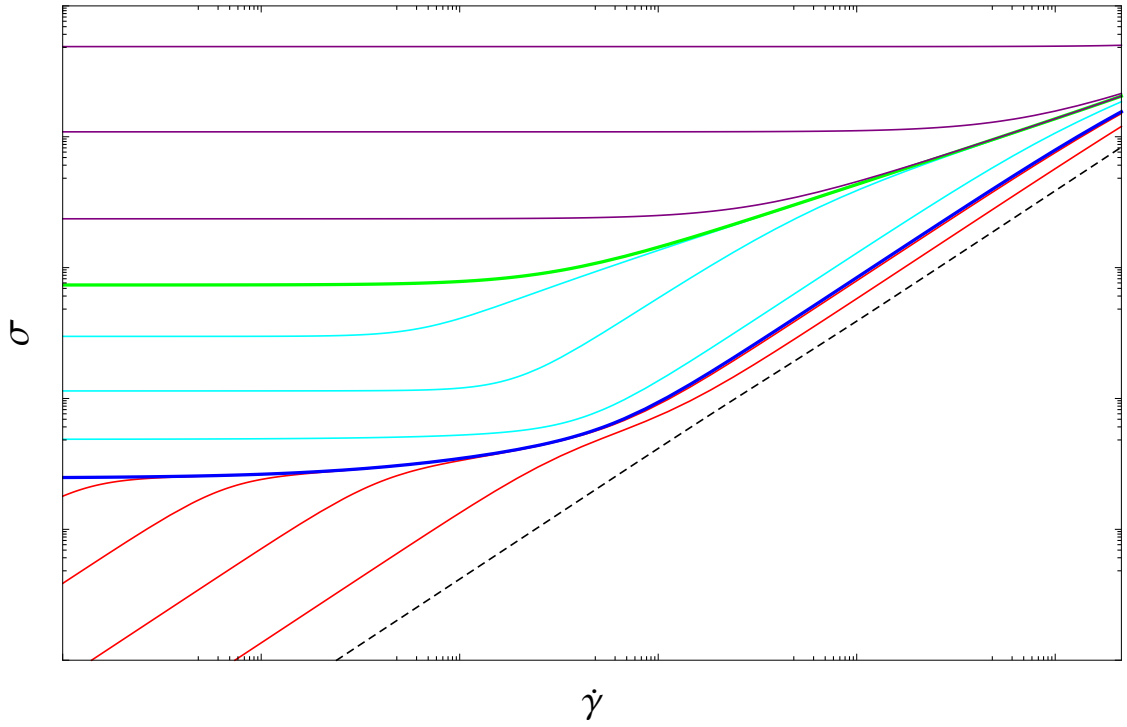

Figure 5.12: Stress-vs.-strain-rate flow curves following Eq. 5.5a-c plotted with arbitrary parameters to illustrate the model. The dashed black line represents the dilute behavior of a Newtonian liquid with viscosity η_s, $\sigma = \eta_s\dot{\gamma}$. The red lines are in the region $\phi < \phi_G$; note the "apparent" yield stress at low $\dot{\gamma}$ becomes a true yield stress at the glass transition, $\phi = \phi_G$, represented by the blue curve. Cyan curves lie in the region between the glass and jammed states, $\phi_G < \phi < \phi_J$, the green curve represents $\phi = \phi_J$, and the purple curves represent higher $\phi > \phi_J$.

replace $\phi \to \zeta$ and $\phi_G \to \zeta_G$. The fits, shown as solid lines in Fig. 5.11a and c, are quite good, although they deviate somewhat for low ζ in the low-$\dot{\gamma}$ regime. In all cases, the fits do not show a true yield stress, and thus $\zeta < \zeta_G$, confirming our observations from DLS and oscillatory rheology that our samples have not yet reached the glassy state. We note that other models have been developed for use with viscoelastic colloidal suspensions [208–210] that predict the same qualitative behavior we observe in our flow curves (namely an "apparent" yield stress below the glass transition, shear thinning at intermediate $\dot{\gamma}$, and an approach to some infinite-shear viscosity at high $\dot{\gamma}$).

Finally, we are able to extract t_α from these measurements as well. The downturn at low $\dot{\gamma}$ of the stress curve (or equivalently, the flattening-off of η at low $\dot{\gamma}$) is due to the fact that at lower $\dot{\gamma}$, the particles are able to rearrange as though they are not being sheared. Above this $\dot{\gamma}$, the dominant relaxation process is driven by shear advection. This can be seen from Eq. 5.5b. For $\phi < \phi_G$, the first term is zero. The second term has two limiting behaviors: for $\dot{\gamma} \lesssim (\tau_T G(\phi, \phi_G))^{-1}$, $\sigma_G \propto \dot{\gamma}\tau_T G(\phi, phi_G)$; for $\dot{\gamma} \gtrsim (\tau_T G(\phi, \phi_G))^{-1}$, $\sigma_G \propto 1 + p_G(\dot{\gamma}\tau_T)^{\alpha_G}$. The function $G(\phi, \phi_G)$ determines the increase of t_α with ϕ [23**?**], and because the crossover between these two regimes corresponds to the downturn of σ at low $\dot{\gamma}$ that we observe experimentally, we determine $t_\alpha = 1/\dot{\gamma}_c$, where $\dot{\gamma}_c$ is the value of $\dot{\gamma}$ that this downturn occurs. Values of t_α, obtained from this method are the same as from oscillatory rheology, as shown by red circles in Fig. 5.10. We note that the identification of this downturn with the alpha relaxation time is generic [208, 209] and not restricted to this model.

5.5 Relaxation Times vs. ζ

We now examine our relaxation time measurements from DLS (shown in Fig. 5.6) and oscillatory and steady-state rheology (shown in Fig. 5.10) together. Fig. 5.13 shows the combined measurements. At low ζ, only one characteristic timescale is present, the diffusive timescale. As ζ increases, the system becomes supercooled and a second timescale emerges, t_β, shown by white squares. Although t_β changes comparatively little with ζ, remaining less than an order of magnitude above the diffusive timescale, t_α, shown by black squares,

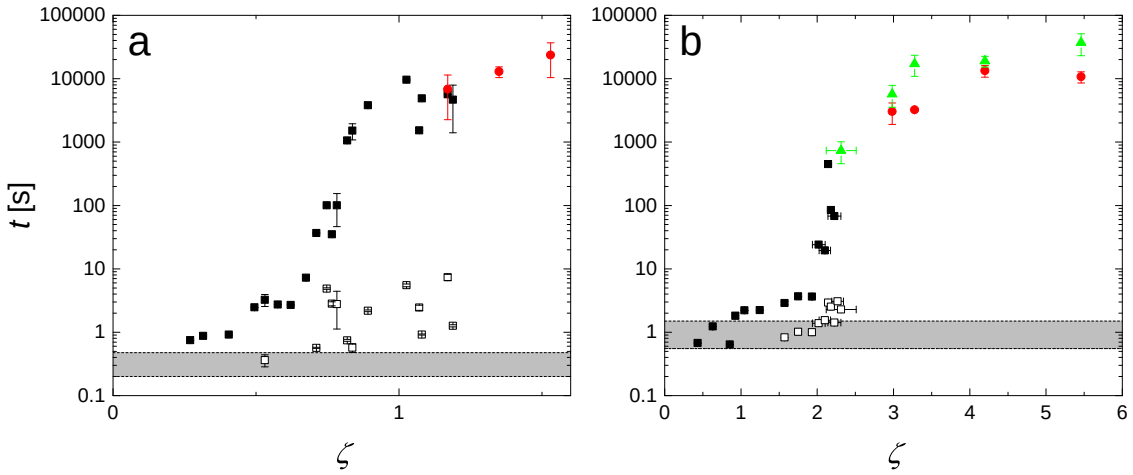

Figure 5.13: The complete set of measurements of t_α and t_β vs ζ for (a) pH 5 and (b) pH 6.5. Filled and open black squares represent t_α and t_β obtained from DLS, respectively; red circles are $t_\alpha = 2\pi/\omega_{\text{crossover}}$ from oscillatory rheology; and green triangles are $t_\alpha = 1/\dot{\gamma}$ from steady-state rheology. Gray bars represent the diffusive timescale measured via DLS in dilute conditions.

increases several orders. At higher ζ still, t_α levels off, which our rheological measurements confirm (red circles for oscillatory and green triangles for steady-state). Not only do we see that our three independent measurements of t_α agree very well, but the plots conclusively show that the divergence predicted by our fit to Eq. 5.3 does not occur.

Previous studies of glassforming polymers using a variety of experimental methods have found deviations from the "expected" divergence of relaxation times at the glass transition [15, 211–219]. Combining these and other studies, reviews [220, 221] conducted of the literature of polymeric and molecular glassformers have investigated the evidence that relaxation times diverge at some finite $T = T_0$, corresponding to $\phi = \phi_0$ for colloidal glassformers. They find that, while the VFT equation and others that assume diverging relaxation timescales for $T = T_0$ are successful in describing the data *in the region* $T > T_0$, there is little evidence that the relaxation time actually diverges for $T \leqslant T_0$. In large part this is due to the difficulty of preparing samples deep in the glassy state, which requires long equilibration times. This has been partially avoided in studies of ancient naturally-formed amber glass [14–16] and molecular glasses generated deep within the glassy state via physical vapor deposition [17]. These studies seem to confirm the idea that the relaxation times do not truly diverge, although they continue to increase.

The relaxation of colloidal glassformers at high concentrations, when t_α has increased significantly, has been examined comparatively little. Two DLS studies of model hard spheres measured t_α as a function of ϕ, but only for ϕ "below the glass transition," i.e. in the region of initial increase of t_α [9, 39]. Another DLS experiment, also performed on hard spheres, observed a slight deviation from t_α divergence at high ϕ [30]. In this study, t_α continued increasing rapidly throughout the studied range of ϕ, but the rate of increase slowed for t_α above about 10^4 times the dilute value. DLS measurements on colloids of various stiffnesses have determined that soft colloids make less fragile glasses [167]—that is, t_α increases more gradually with ζ for softer particles—however, the measurements in this study were also restricted to low ζ below the apparent divergence of t_α. Similar results were observed for a system of soft colloids in a combined DLS and rheology study [35].

To our knowledge, only two studies similar to ours have been performed. The first [38] did not incorporate DLS, instead relying on a combination of oscillatory and steady-state rheology. The particles used in this study were produced by grafting a dense layer of poly(ethylene glycol), with length about 1 nm, onto spherical silica cores each of radius about 5 nm. The behavior of t_α was qualitatively similar to that shown in Fig. 5.13: an initial apparent divergence gave way to a regime in which t_α leveled off, but those results were not explained. The authors also noted that the measured values of t_α and zero-shear viscosity were proportional across the entire range of particle concentrations studied, which follows from the relation $t_\alpha = \eta_0/G'_\infty$, if G'_∞, the limiting value of $G'(\omega)$ as $\omega \to \infty$, remains constant with particle concentration, as is the case with, for example, suspensions of hard spheres [222].

The second [223] combined autocorrelation DLS, modified for use with non-ergodic systems [224], with steady-state and oscillatory rheology. They examined dense suspensions of partially charged ethyl acrylate/methacrylic acid microgels crosslinked with dicyclopentenyloxyethyl methacrylate. The microgels used in this study were not temperature-sensitive and although the acid groups made up nearly 40 mol% of the total monomer content in the particles, 5% or less of these groups were charged at the studied conditions: rather than fixing pH or salt concentration, the amount of added NaOH was fixed to be equal to the amount

of methacrylic acid in the suspension. This resulted in suspensions of different pH (not measured), with most of the methacrylic acid uncharged. No salt was added. Additionally, the amount of crosslinker included was much smaller, and the authors expected that the particles would be homogeneous spheres rather than core-shell as a result. Notably, the light scattering measurements were performed only at $\theta = 90$ °, rather than at the peak of $S_{\mathrm{M}}(q)$, corresponding to $qR_{\mathrm{h}} \gtrsim 6$ at the studied conditions. Relaxation times calculated from steady-state measurements were also at least an order of magnitude lower than the inverse of the shear rate at which shear thinning begins, although this was likely due to the different criterion used: rather than taking the $\dot{\gamma}_{\mathrm{c}}$ to be the shear rate at the onset of shear thinning, it was taken from the onset of the power-law-like region, $\eta(\dot{\gamma}) \propto \dot{\gamma}^n$, which occurs *after* the downturn. Finally, the calculated relaxation times were always proportional to η_0, increased with increasing ζ, and remained concave-up throughout the entire studied range of concentration. This is reminiscent of the behavior we observe for t_α at low ζ, but does not reproduce the leveling-off we observe for the most concentrated suspensions.

Our system shows markedly different behavior. Specifically, t_α and η_0 are *not* proportional: a quick comparison of Figs. 5.11c and 5.13 shows that for the pH 6.5 samples, as ζ increases from 0 to 5.5, η_0 and t_α increase by factors of almost exactly 10^8 and 10^4, respectively, indicating that G'_∞ is *not* constant with increasing ζ. The likely physical explanation for the differences between our results and those of [38] and [223] will be discussed in the Conclusions section of this Chapter.

Even though G'_∞ is not observable with our oscillatory measurements because the relevant ω window is far above what is accessible with the instrument, we expect that the plateau value of the elastic modulus, G'_{P}, should qualitatively fill the same function as a measure of the elasticity of the suspension measured at short timescales. In Fig. 5.14, we plot the values of t_α obtained from our rheology measurements vs. the ratio η_0/G'_{P}. We find that the relationship between the two is reasonably described either by a line or a power law with exponent between 0.5–1. This is consistent with the idea that even though the viscosity of the system increases many orders of magnitude with increasing ζ, this is largely compensated for by an increasing elastic modulus of the particles, resulting in a

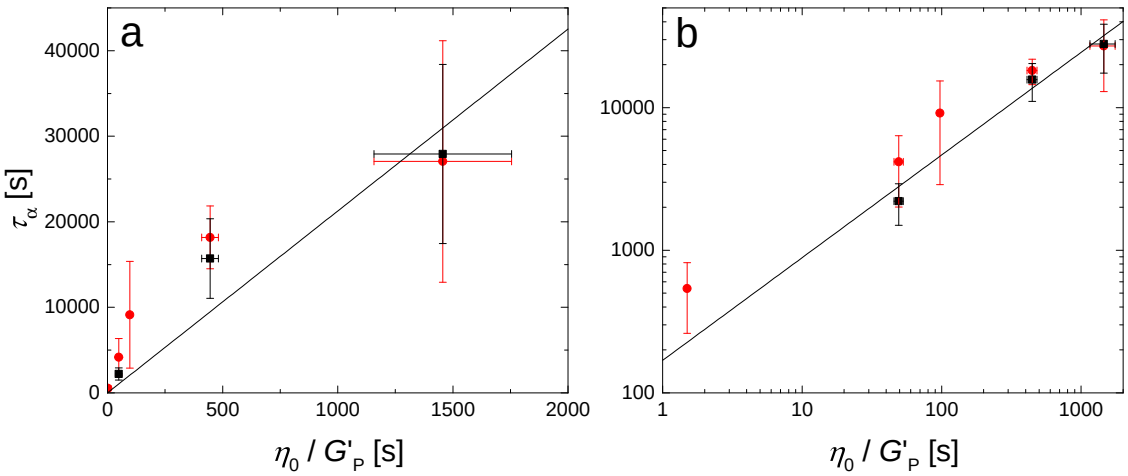

Figure 5.14: Plots of t_α, as measured by oscillatory and steady-state rheology (black squares and red circles, respectively), vs. the ratio $\eta_0/G'_{\rm P}$. (a) A linear plot. The black line is the best fit to a line with slope 21 ± 6. (b) A log-log plot. The black line is the best fit to a power law fit with $t_\alpha \propto (\eta_0/G'_{\rm P})^{0.72\pm0.14}$.

nearly constant t_α.

5.6 Ionic Deswelling: How the System Remains Liquid-like

The dependence of the elastic modulus on ζ indicates that the structure of the particles is changing as ζ continues to increase. In fact, our SLS measurements of $S_{\rm M}(q)$ provide independent confirmation of this: as ζ is increased, the peak of $S_{\rm M}(q)$, $q_{\rm peak}$, increases, as shown in Fig. 5.3. This indicates that the center-to-center distance between particles, $2\pi/q_{\rm peak}$, is decreasing with increasing ζ. We emphasize that the center-to-center distance may *not* correspond to twice the radius of the particles, although this will be true once the particles are in contact and compressing. For more dilute systems, provided that the particles are concentrated enough to develop "shells" of nearest neighbors, the center-to-center distance will be greater than twice the dilute particle radius and the particles may not shrink.

We do expect that for ζ greater than some $\zeta_{\rm c}$, the particles must begin to compress, deform, or interpenetrate. The center-to-center distance should then go as

$$\frac{2\pi}{q_{\rm peak}} = 2R_{\rm h}\left(\frac{\zeta}{\zeta_{\rm c}}\right)^{-\nu}, \tag{5.10}$$

where $R_{\rm h}$ is the particle hydrodynamic radius measured in dilute conditions and ν is the rate

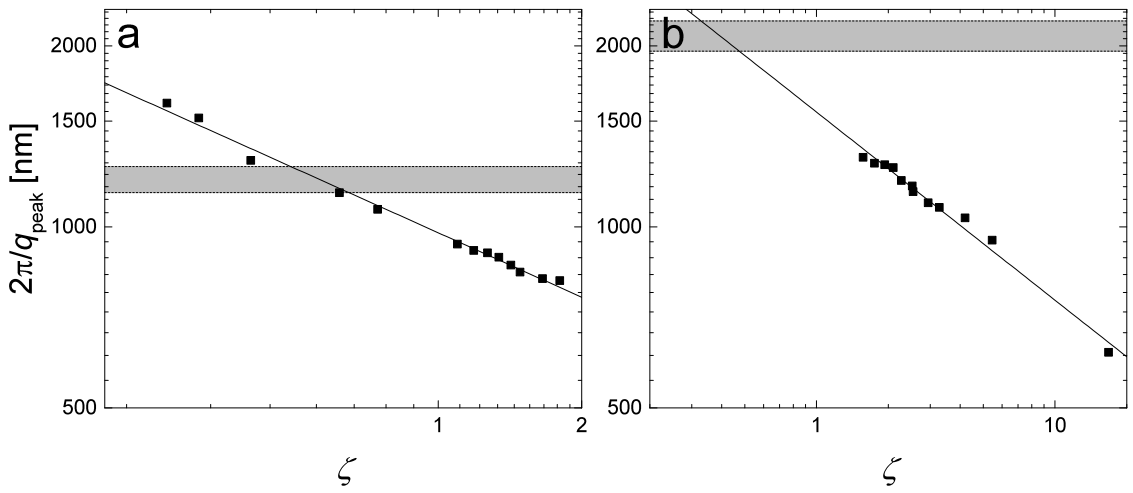

Figure 5.15: We plot the calculated center-to-center distances obtained from SLS as a function of ζ for samples at (a) pH 5 and (b) pH 6.5. The gray bars represent twice the radius of one particle in dilute conditions, $2R_{\rm h}^{\rm dil} = 1200 \pm 60$ nm for pH 5 and $2R_{\rm h}^{\rm dil} = 2080 \pm 120$ nm for pH 6.5. The black lines are fits to Eq. 5.10. The range of $\zeta_{\rm c}$ is given by the region of overlap of the black line and the gray bar.

at which the particles compress or interpenetrate with increasing ζ. For spherical particles that shrink isotropically, $\nu = 1/3$. For spherical particles, $\nu < 1/3$ if the particles interpenetrate, and $\nu > 1/3$ if the particles do not come into contact, for example due to some long-range repulsion. ν can also vary from 1/3 if the particles are not spherical, for example if facets form on contact between neighbors. We plot the center-to-center distances obtained from our SLS measurements in Fig. 5.15, find that the data follows this expectation, with ν close to 1/3. For particles at pH 5, we find $\zeta_{\rm c} = 0.57 \pm 0.10$ and $\nu = 0.356 \pm 0.010$, and for pH 6.5, $\zeta_{\rm c} = 0.40 \pm 0.11$ and $\nu = 0.313 \pm 0.012$. Using these measurements, we estimate the *actual* volume fraction, ϕ, from the *generalized* volume fraction, ζ, by assuming that the microgels remain spherical at all concentrations. Then $\phi/\zeta = v^{\rm P}(\phi)/v_0^{\rm P}$, where $v^{\rm P}(\phi)$ is the actual volume of the microgels [54]. We emphasize that obtaining ϕ is not trivial. In our case, we assume that at high ζ (i) significant interpenetration does not occur, (ii) the particles remain approximately spherical, and (iii) the particle radius is roughly equal to half the center-to-center distance for $\zeta > \zeta_{\rm c}$. These assumptions have been shown to be valid in concentrated suspensions of microgels at ζ high enough that significant deswelling begins to occur [89]. For $\zeta < \zeta_{\rm c}$, before the microgels have begun to compress, $\zeta = \phi$. We

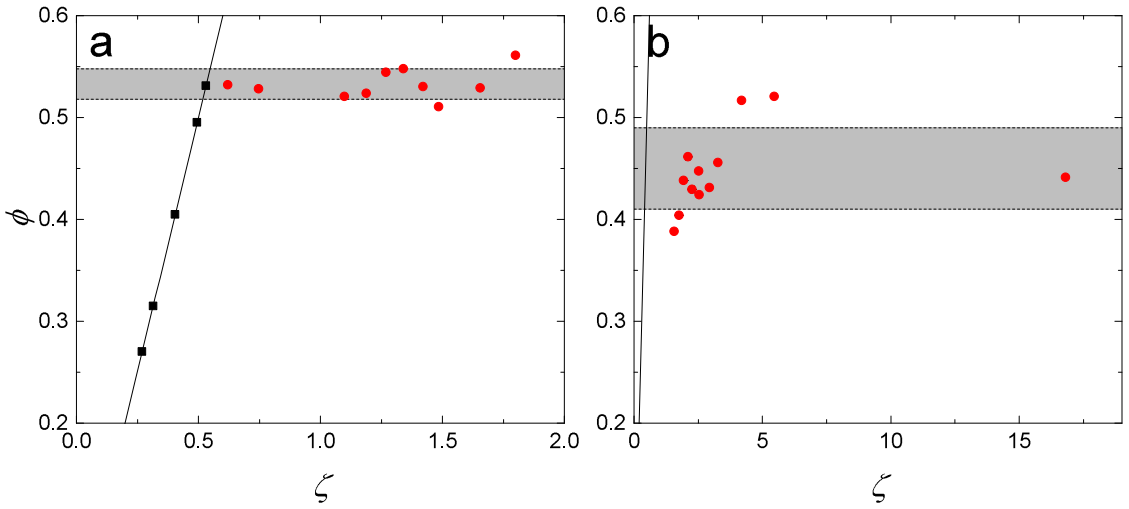

Figure 5.16: The calculated values of ϕ as a function of ζ for samples at (a) pH 5 and (b) pH 6.5. The black lines represent $\phi = \zeta$, the behavior for $\zeta < \zeta_c$, and the black points in panel (a) were measured in this region and therefore fall onto the line. Red points were measured for $\zeta > \zeta_c$. The gray bar represents one standard deviation around the mean value of the red points, assuming that ϕ is constant above ζ_c.

thus have

$$\phi(\zeta) = \begin{cases} \zeta & \zeta < \zeta_c \\ \zeta \left(\frac{2\pi/q_{peak}}{2R_h} \right)^3 & \zeta \geqslant \zeta_c \end{cases} . \tag{5.11}$$

We show the resulting calculated ϕ in Fig. 5.16 for both pHs. In fact, we see that as ζ increases, the particles shrink just enough to keep ϕ approximately constant for $\zeta > \zeta_c$. This also enables us to plot t_α as a function of ϕ, which we do in Fig. 5.17. That the pH 5 data shown in Fig. 5.17a appear to show ϕ decreasing as t_α increases for high ζ is an artifact of using Eq. 5.11 to estimate ϕ. For low $\zeta < \zeta_c$, $\phi = \zeta$; these points are the nearly horizontal line of black squares just above the gray bar in the figure. The negative slope for higher ζ is due to the fact that Eq. 5.11 has $2\pi/q_{peak} \propto \phi^{1/3}$, while the experimental exponent, ν in Eq. 5.10, is greater than 1/3. (If ν were exactly equal to 1/3, the high-ζ region in Figs. 5.17a and b would be vertical.) The uncertainty in ν is large enough to account for this observation, but in any event the ϕ at which t_α begins to increase does not noticeably change for any ν near 1/3.

We see that t_α increases over a very narrow range of ϕ above a critical value, which is also when the particles begin to deswell. Because for these soft particles, unlike hard

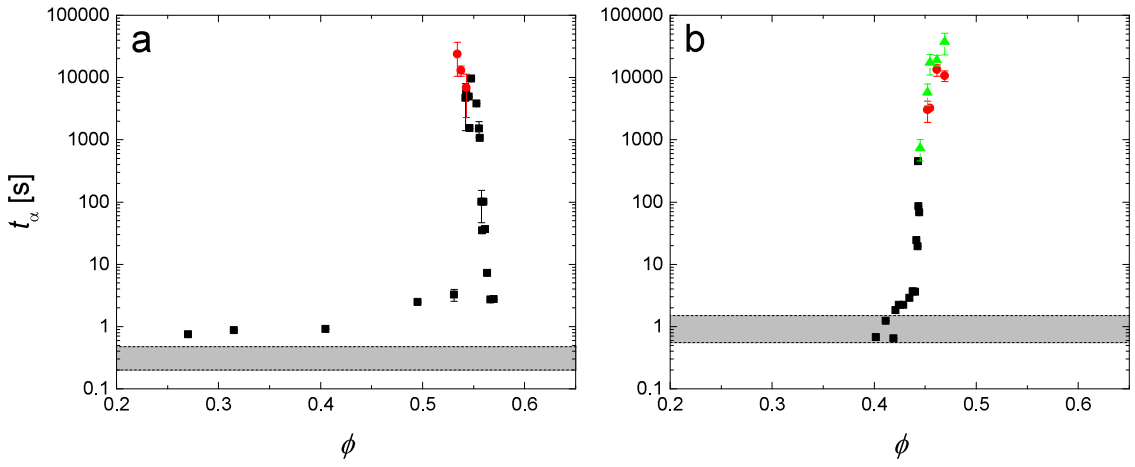

Figure 5.17: t_α, as measured from DLS (black squares) and rheology (red circles for oscillatory and green triangles for steady-state), vs. ϕ calculated from SLS as discussed in the text for (a) pH 5 and (b) pH 6.5. The gray bar represents the diffusive timescale.

spheres, ϕ is not the only relevant thermodynamic quantity—we must also consider particle stiffness—this does not provide a complete picture of the particles' glassforming behavior, but it serves to illustrate the important distinction between ζ and ϕ in determining the dynamic behavior of the system.

We can also explain the source of this observed deswelling. Previous work [54] showed that ionic microgels deswell due to the osmotic pressure contribution of unbound counterions in the solvent, which dominates the total osmotic pressure of the system. (Provided such deswelling begins substantially below random close packing, as we will show that in our case it does, this implies that deswelling caused by steric repulsion between the particles plays at most a secondary role.) This contribution in turn is dependent on the real microgel volume fraction ϕ [55]. The particles begin to deswell appreciably when the counterion osmotic pressure, $\Pi_c(\phi)$,

$$\Pi_c(\phi) = k_B T \frac{\Gamma Q}{v_0^P} \frac{\phi}{1-\phi}, \tag{5.12}$$

exceeds the microgel bulk modulus K. The fraction of unbound counterions is given by [54, 55]

$$\Gamma = \sqrt{\frac{3R_0}{\ell_B Q}}, \tag{5.13}$$

where $\ell_B \approx 0.7$ nm is the Bjerrum length of the solvent and Q is the number of charged

groups attached to the microgel. We can estimate Q, and therefore Γ, from the details of the microgel synthesis. As discussed in Ch. 2, section 2.2, our particles are 24 mol% AAc, 73 mol% NIPAM, and 3 mol% pEG-d. Only the AAc can be charged, and the fraction that is charged depends on the pH of the sample.

We already calculated $Q_{\mathrm{pH}=5} = (9 \pm 5) \times 10^7$ in section 4.3. Following the same arguments, and noting that at pH 6.5, more than 99% of the AAc groups should be ionized, we take $Q_{\mathrm{pH}=6.5} = (1.1 \pm 0.6) \times 10^8$. We obtain $\Gamma_{\mathrm{pH}=5} = (6.2 \pm 1.9) \times 10^{-3}$ and $\Gamma_{\mathrm{pH}=6.5} = (7.4 \pm 2.3) \times 10^{-3}$, giving $(\Gamma Q)_{\mathrm{pH}=5} = (4.6 \pm 1.4) \times 10^5$ and $(\Gamma Q)_{\mathrm{pH}=6.5} = (6.7 \pm 2.1) \times 10^5$; note that $\Gamma_{\mathrm{pH}=5} < \Gamma_{\mathrm{pH}=6.5}$ and $Q_{\mathrm{pH}=5} < Q_{\mathrm{pH}=6.5}$, indicating that the effect of the counterions is more important at pH 6.5.

We can therefore estimate the parameters in Eq. 5.12 for our particles as

$$\Pi_{\mathrm{c}}^{(5)} = (2100 \pm 800 \text{ Pa}) \frac{\phi}{1-\phi}, \tag{5.14a}$$

$$\Pi_{\mathrm{c}}^{(6.5)} = (590 \pm 250 \text{ Pa}) \frac{\phi}{1-\phi}. \tag{5.14b}$$

Plugging in $\phi = \zeta_{\mathrm{c}}$, the point at which our microgels begin to deswell, we then obtain an estimate for the bulk moduli as $K = 2900 \pm 1300$ Pa for the microgels at pH 5, and $K = 420 \pm 190$ Pa at pH 6.5. These values agree very well with previously-published measurements of the bulk modulus for microgels with similar crosslinker content, and therefore stiffness [54, 225]. Further, we note that the ratio of our estimated bulk moduli, 6.9, is close to the ratio of volumes of the microgels at both pHs measured in dilute conditions, 5.2, which is reasonable if the elasticity of the polymer chains dominates the particle elasticity, since more chains are packed into a smaller volume for the relatively deswollen pH 5 particles. Finally, we note that the relatively low ϕ at which deswelling begins, $\phi = \zeta_{\mathrm{c}} \approx 0.45$, is explained in this picture as well. A higher fraction of unbound counterions, lower bulk modulus, and higher dilute particle volume imply that the particles should begin deswelling due to ionic osmotic pressure at lower ϕ, which is exactly what we see. These results validate our analysis of the particles at high concentrations.

5.7 Conclusions

We attribute the non-divergence of t_α with increasing ζ to a combination of increasing single-particle elasticity and relatively constant ϕ. These effects are due to the fact that the particles deswell at high ζ, which in our system is caused by ionic deswelling similar to that previously observed in charged, concentrated microgel systems. This also helps to explain the differences between our results and those of [223], where the fraction of ionized groups was too low to induce ionic deswelling in the microgels at ζ low enough that the system had yet to solidify. Thus, when the particles came into contact at high enough ζ, the system became rigid and the relaxation time diverged. In the case of [38], although the system was uncharged, those particles were able to interpenetrate due to the majority of their volume being made up of uncrosslinked pEG brushes, effectively making them star polymers. At high concentrations, star polymers, like linear polymers, can remain liquid even at $\phi = 1$, depending on the number and stiffness of arms, and it is therefore not surprising that no diverging timescale was observed.

Because it inherently relies on the ability of soft colloidal particles to deswell, the mechanism described in this Chapter should also have no analogue to molecular glassforming systems, and therefore represents both a new type of glassforming physics unique to soft colloids, and a potential obstacle to modeling molecular glassforming systems with colloids.

CHAPTER VI

CONCLUSIONS

From this Thesis we can extract the following conclusions:

Light scattering data processing We have developed a method for processing static and dynamic light scattering data and incorporated it into a suite of Matlab programs for easy use.

- We obtain the best fits from DLS data for dilute samples by sequentially fitting larger and larger subsets of the data for each measurement to an exponential decay. The fit with the lowest value of χ^2 is taken as the best fit, and the process is repeated for each measurement point. The resulting relaxation times are fitted all together to give the best value of the diffusion coefficient for the system.
- Our program corrects for the effect of the nonlinearity of the detectors, which has been quantified by experimental measurement of the individual dead times for both detectors in our setup. This corrects both the measured intensity and the intercept. We confirm that the intercept correction developed for autocorrelation DLS can also be successfully applied to cross-correlation 3DDLS.
- Our program contains the standard corrections for the baseline intensity, the angular dependence of the projected scattering volume, and instrument alignment.
- Our program corrects for multiple scattering due to turbid samples and those with deep scattering minima, incorporating measured reference intercepts with isotropic scatterers across a wide range of temperatures.

3DDLS interference fringe and convection effects We have also described a new phenomenon in 3DDLS at high temperatures, due to the convection-driven movement of particles through an interference fringe formed by the crossed beams, which does not occur in autocorrelation DLS. For particles in a specific size range, measured at

high enough temperatures that the sample convects, the movement of these particles through the fringe causes intensity correlations whose timescale overlaps with that due to the particles' diffusive motion. The resulting correlation functions cannot be used to measure the diffusion coefficient of the particles. We avoid this by performing autocorrelation experiments on dilute samples, or by using very small sample volumes, such that the temperature difference across the sample is too low for convection to occur.

SLS and SANS data stitching We have developed a method to combine non-overlapping light and neutron scattering data onto the same intensity scale for direct comparison and implemented it in a Mathematica program. The method relies on a composite model that can describe the scattering data over a wide range of length scales. Having such a model, we first fit it separately to both sets of data to obtain approximate values for the fitting parameters. We then simultaneously fit both sets of data, with the comparative intensity scales as additional free parameters. We obtain similar values for the fitting parameters as those from the independent fits, but with smaller uncertainty.

Comonomer frustration of pNIPAM chain collapse in microgels NIPAM microgels synthesized with large amounts of randomly-distributed AAc are unable to homogeneously collapse at high temperatures above the LCST of pNIPAM even when the AAc is neutral. This is because the collapse of a pNIPAM polymer chain is cooperative and requires a minimum number of consecutive NIPAM monomers to execute. AAc breaks up the NIPAM sequence and prevents its collapse.

- SANS measurements at high T require the Debye-Bueche model to fit, rather than the Lorentzian, indicating that the material inside the microgel is clumped and inhomogeneous.
- The length scale of this clumping increases with T and corresponds with a similar increase in $R_{\mathrm{g}}/R_{\mathrm{h}}$ of the microgels as measured with light scattering. This value increases to 1, indicating that the particle periphery is denser than the core, the

opposite of the low-temperature case. This is because the microgel crosslinker is preferentially located in the core, shortening the chain length between crosslink points, and decreasing the probability that a given sequence will have enough consecutive NIPAM monomers to collapse. The longer chains in the periphery are more likely to be able to collapse, leading to the denser periphery.

- This phenomenon is not limited to microgels or to this particular polymer chemistry. In principle, macrogels and other polymer-based systems could be synthesized with this property of frustrated collapse. Other combinations of polymer would work as well; for example, AAc could be replaced with styrene, or NIPAM with NIPMAM.

Charge segregation in weakly-charged microgels in a poor solvent When weakly charged and at high temperatures, the microgels microphase separate into charged and uncharged regions. The AAc in the core is left uncharged, while the AAc at the periphery is ionized.

- The characteristic length scale measured by SANS decreases at high T because scattering from the denser core dominates over that from the diffuse periphery. This corresponds with a similar decrease in $R_{\mathrm{g}}/R_{\mathrm{h}}$ as measured with light scattering. This value decreases to 0.2, indicating that almost all of the mass is concentrated in a small core.
- SANS measurements of chemically similar microgels synthesized without crosslinker are well-described by the relevant theory for weakly-charged polymer networks in a poor solvent, showing a peak at high q predicted by the theory and identified with microphase separation within the microgel. The microgels with crosslinker do not show this maximum because the crosslinker interferes with a particle-wide microphase separation.

Suppression of the glass transition in dense suspensions of charged soft microgels Dense suspensions of soft, ionized microgels display several hallmarks of an approach

to the glass transition. No such transition occurs, however. Instead, the system remains a supercooled liquid as ζ continues to increase.

- Structure factor measurements show an increasingly-ordered system and a decreasing center-to-center distance between particles as ζ increases. At high ζ, the center-to-center distance decreases below two dilute particle radii, meaning that deswelling is certainly occurring.
- DLS measurements at the position of the first peak of $S_{\mathrm{M}}(q)$ show that the relaxation splits from a single diffusive decay at low ζ into two decays. The first, the β decay, remains close to the dilute decay and represents the thermal motion of a particle trapped within its cage of neighbors. The second, the α decay, follows a stretched exponential and slows down dramatically as ζ increases.
- Oscillatory and steady-state rheology provide two independent measurements of the alpha relaxation. They confirm that t_α nearly plateaus above some critical ζ.
- Steady-state flow curves confirm that there is no true liquid-to-solid transition within the measured range of ζ. Although there is an "apparent" yield stress for suspensions at high ζ, the suspension in fact continues to flow at long timescales, although the low-shear viscosity does continue to increase. Fits to theory developed to differentiate between the liquid, supercooled liquid, glassy, and jammed states confirms this behavior.
- This avoidance of the glass transition is caused by deswelling in the system. Osmotic pressure due to ions in solution causes the microgels to shrink. This has the dual effects of keeping ϕ roughly constant as ζ increases, and increasing the elasticity of the particles. Increased particle elasticity and increased suspension viscosity partially cancel out and keep t_α nearly constant.
- Considering t_α as a function of ϕ instead reveals that t_α diverges sharply at some critical ϕ for both studied charge states of the particles.

This Thesis has demonstrated profound effects of particle charge and softness on the approach to a glassy state. Soft, charged particles are able to deswell on the approach to the glass, keeping the system in a supercooled state even as the number of particles in the system increases by an order of magnitude. This phenomenon is only visible in systems with ζ above the glass transition that would be predicted by the system behavior at intermediate ζ, such as by a fit to the VFT equation. Measurements of these systems must therefore be made very carefully to avoid drawing incorrect conclusions about high-ζ, "glassy" regimes from the behavior observed at lower ζ. We further emphasize that this mechanism is fundamentally unique to soft colloidal systems, and comparisons between the glassforming physics of such systems and molecular glassformers cannot be made trivially.

APPENDIX A

DEFINITIONS USED IN THE TEXT

A.1 Fourier Transform

The Fourier Transform is defined as

$$\begin{aligned}\hat{f}(\mathbf{k}) &= \mathcal{F}\{f(\mathbf{r})\}(\mathbf{k}) = K\int_{\mathbb{R}^3} \mathrm{d}\mathbf{r} f(r)\exp\left(\mathrm{i}\mathbf{k}\cdot\mathbf{r}\right),\\ f(\mathbf{r}) &= \mathcal{F}^{-1}\{\hat{f}(\mathbf{k})\}(\mathbf{r}) = \hat{K}\int_{\mathbb{R}^3_k} \mathrm{d}\mathbf{q}\hat{f}(q)\exp\left(-\mathrm{i}\mathbf{k}\cdot\mathbf{r}\right),\end{aligned} \tag{A.1}$$

where $K\hat{K} = (2\pi)^{-3}$. However, for the case of a spherically symmetric $f(r)$ there is a somewhat commonly-used and more intuitive way to write the Fourier transform:

$$\begin{aligned}\int_{\mathbb{R}^3} \mathrm{d}\mathbf{r} f(r)\exp\left(\pm\mathrm{i}\mathbf{k}\cdot\mathbf{r}\right) &= \int_0^{2\pi}\mathrm{d}\phi\int_0^{\pi}\sin\theta\mathrm{d}\theta\int_0^{\infty} r^2\mathrm{d}r f(r)\exp\left(\pm\mathrm{i}\mathbf{k}\cdot\mathbf{r}\right)\\ &= 2\pi\int_0^{\pi}\sin\theta\mathrm{d}\theta\int_0^{\infty} r^2\mathrm{d}r f(r)\exp\left(\pm\mathrm{i}kr\cos\theta\right)\\ &= 2\pi\int_0^{\infty} r^2\mathrm{d}r\int_{-1}^{1}\mathrm{d}(\cos\theta) f(r)\exp\left[\pm\mathrm{i}kr\cos\left(\theta\right)\right]\\ &= 2\pi\int_0^{\infty} r^2\mathrm{d}r f(r)\frac{\exp\left(\pm\mathrm{i}kr\right)-\exp\left(\mp\mathrm{i}kr\right)}{\pm\mathrm{i}kr}\\ &= 2\pi\int_0^{\infty} r^2\mathrm{d}r f(r)\frac{2\sin\left(kr\right)}{kr}\\ &= 4\pi\int_0^{\infty} r^2\mathrm{d}r f(r)\frac{\sin\left(kr\right)}{kr},\end{aligned} \tag{A.2}$$

where in the second line the z-axis is chosen to lie along $\mathbf{k}$ and in the third line the order of integration is switched and the variable of integration in the angular integral is changed from θ to $\cos\theta$. The limits of integration on the angular integral are switched to absorb the minus sign that follows from this variable change.

Then the Fourier Transform can more transparently be written as

$$\begin{aligned}\hat{f}(k) &= \mathcal{F}\{f(r)\}(k) = \sqrt{\frac{2}{\pi}}\int_0^{\infty} r^2\mathrm{d}r f(r)\frac{\sin\left(kr\right)}{kr},\\ f(r) &= \mathcal{F}^{-1}\{\hat{f}(k)\}(r) = \sqrt{\frac{2}{\pi}}\int_0^{\infty} k^2\mathrm{d}k\hat{f}(k)\frac{\sin\left(kr\right)}{kr}.\end{aligned} \tag{A.3}$$

A.2 Convolution

The convolution of two functions f and g is defined by

$$(f * g)(t) = \int_{-\infty}^{\infty} \mathrm{d}\tau f(\tau) g(t-\tau) = \int_{-\infty}^{\infty} \mathrm{d}\tau f(t-\tau) g(\tau). \tag{A.4}$$

The convolution theorem states that Fourier transforms and convolutions are commutative in the following sense:

$$\mathcal{F}\{f * g\} = \mathcal{F}\{f\} \times \mathcal{F}\{g\} \tag{A.5}$$

and

$$\mathcal{F}\{f \times g\} = \mathcal{F}\{f\} * \mathcal{F}\{g\}. \tag{A.6}$$

APPENDIX B

NON-ERGODIC 3DDLS

B.1 Autocorrelation DLS

In this type of experiment, a beam of laser light is directed through the sample and its measured scattered intensity at time t and a later time $t+\tau$ are correlated, defining the Intensity Autocorrelation Function (IACF):

$$G_{\mathrm{I}}(q,\tau) = \langle I(q,t)I(q,t+\tau)\rangle_{\mathrm{E}} = \frac{\epsilon_{\mathrm{s}}}{4\mu_0}\langle E(q,t)E(q,t+\tau)E^*(q,t)E^*(q,t+\tau)\rangle_{\mathrm{E}}. \tag{B.1}$$

The brackets $\langle\cdots\rangle_{\mathrm{E}}$ represent ensemble averages of the measured quantities.

The scattered field strength is a sum over statistically independent terms. Provided that there are sufficiently many of these terms, the central limit theorem says that E is a Gaussian variable with zero mean; in that case Wick's theorem says that the above ensemble average can be rewritten to give:

$$\begin{aligned} G_{\mathrm{I}}(q,\tau) = \frac{\epsilon_{\mathrm{s}}}{4\mu_0}[&\langle E(q,t)E^*(q,t)\rangle_{\mathrm{E}}\langle E(q,t+\tau)E^*(q,t+\tau)\rangle_{\mathrm{E}} \\ &+\langle E(q,t)E(q,t+\tau)\rangle_{\mathrm{E}}\langle E^*(q,t)E^*(q,t+\tau)\rangle_{\mathrm{E}} \\ &+\langle E(q,t)E^*(q,t+\tau)\rangle_{\mathrm{E}}\langle E^*(q,t)E(q,t+\tau)\rangle_{\mathrm{E}}]. \end{aligned} \tag{B.2}$$

The first term in the square brackets is $\langle I(q)\rangle_{\mathrm{E}}^2$, the square of the mean scattered intensity. The second is zero for nonzero scattering vectors [74], and therefore in experiment. The third term defines the Electric Field Autocorrelation Function (EACF):

$$|G_{\mathrm{E}}(q,\tau)|^2 = \frac{\epsilon_{\mathrm{s}}}{4\mu_0}\langle E(q,t)E^*(q,t+\tau)\rangle_{\mathrm{E}}\langle E^*(q,t)E(q,t+\tau)\rangle_{\mathrm{E}}. \tag{B.3}$$

This then gives the Siegert relation for autocorrelation spectroscopy:

$$G_{\mathrm{I}}(q,\tau) = \langle I(q)\rangle_{\mathrm{E}}^2 + |G_{\mathrm{E}}(q,\tau)|^2\,. \tag{B.4}$$

Or, rewritten in terms of the normalized functions,

$$g_{\mathrm{I}}(q,\tau) = \frac{G_{\mathrm{I}}(q,\tau)}{\lim\limits_{\tau\to\infty} G_{\mathrm{I}}(q,\tau)} = \frac{G_{\mathrm{I}}(q,\tau)}{\lim\limits_{\tau\to\infty}\langle I(q,t)I(q,t+\tau)\rangle_{\mathrm{E}}} = \frac{G_{\mathrm{I}}(q,\tau)}{\langle I(q)\rangle_{\mathrm{E}}^2}, \tag{B.5}$$

$$|g_{\mathrm{E}}(q,\tau)|^2 = \frac{|G_{\mathrm{E}}(q,\tau)|^2}{|G_{\mathrm{E}}(q,0)|^2} = \frac{|G_{\mathrm{E}}(q,\tau)|^2}{\frac{\epsilon_{\mathrm{s}}}{4\mu_0}\langle E(q,t)E^*(q,t+0)\rangle_{\mathrm{E}}\langle E^*(q,t)E(q,t+0)\rangle_{\mathrm{E}}} = \frac{|G_{\mathrm{E}}(q,\tau)|^2}{\langle I(q)\rangle_{\mathrm{E}}^2}, \tag{B.6}$$

$$g_{\mathrm{I}}(q,\tau) - 1 = |g_{\mathrm{E}}(q,\tau)|^2 . \tag{B.7}$$

However, this fails to take into account experimental error such as misalignment. An experimentally measured quantity called the intercept, denoted β, quantifies imperfections that cause the real experiment to differ from the theoretical ideal. It is defined as:

$$\beta = g_{\mathrm{I}}(q,0) - \lim_{\tau\to\infty} g_{\mathrm{I}}(q,\tau) = \frac{\langle I(q,t)I(q,t+0)\rangle_{\mathrm{E}} - \lim_{\tau\to\infty}\langle I(q,t)I(q,t+\tau)\rangle_{\mathrm{E}}}{\lim_{\tau\to\infty}\langle I(q,t)I(q,t+\tau)\rangle_{\mathrm{E}}}. \tag{B.8}$$

Since for long times $\langle I(q,t)I(q,t+\tau)\rangle_{\mathrm{E}}$ decorrelates, this reduces to

$$\beta = \frac{\langle I(q)^2\rangle_{\mathrm{E}} - \langle I(q)\rangle_{\mathrm{E}}^2}{\langle I(q)\rangle_{\mathrm{E}}^2}. \tag{B.9}$$

The Siegert relation is rewritten, defining the experimental $g_{\mathrm{I}}(q,\tau)$ and $|g_{\mathrm{E}}(q,\tau)|^2$ in terms of their ideal-experiment values and the intercept:

$$g_{\mathrm{I}}(q,\tau) - 1 = \beta\,|g_{\mathrm{E}}(q,\tau)|^2 . \tag{B.10}$$

The maximum β in an autocorrelation experiment is 1; $g_{\mathrm{I}}(q,0) = 2$ and $|g_{\mathrm{E}}(q,0)|^2 = 1$.

B.1.1 Ergodic Case

As a practical matter, provided that the measured system is ergodic and thus accesses all of phase space given enough time, a long enough time average is equivalent to an ensemble average, so $\langle\cdots\rangle_{\mathrm{E}}$ can be replaced with the time average, $\langle\cdots\rangle_{\mathrm{T}}$.

B.1.2 Non-ergodic Case

For a non-ergodic system, any DLS experiment becomes more difficult to carry out because the ensemble average and time average are no longer identical. Time-independent quantities can be ensemble-averaged by continuously rotating the sample during a measurement, exploring phase space in a way that the kinetically arrested sample cannot. However, this introduces an artificial time dependence into the measurement that makes it impossible to accurately measure ensemble-averaged time-dependent quantities accurately.

Pusey and van Megen developed a theory to relate the time-averaged autocorrelation function for a non-ergodic system to the true ensemble-averaged correlation function [224]. They found that

$$\begin{aligned} g_{\mathrm{I}}^{(\mathrm{T})}(q,\tau) - 1 = & \frac{\langle I(q,t)I(q,t+\tau)\rangle_{\mathrm{T}}}{\langle I(q)\rangle_{\mathrm{T}}^2} - 1 = \\ & Y^2\left\{\left[g_{\mathrm{E}}^{(\mathrm{E})}(q,\tau)\right]^2 - \left[g_{\mathrm{E}}^{(\mathrm{E})}(q,\infty)\right]^2\right\} \\ & + 2Y\left(1-Y\right)\left[g_{\mathrm{E}}^{(\mathrm{E})}(q,\tau) - g_{\mathrm{E}}^{(\mathrm{E})}(q,\infty)\right], \end{aligned} \tag{B.11}$$

where "(T)" and "(E)" signify time- and ensemble-averaged quantities, respectively, $g_{\mathrm{E}}^{(\mathrm{E})}(q,\infty)$ is the non-ergodicity parameter representing the amount of fluctuations that are "frozen into" the sample, and $Y = \langle I(q)\rangle_{\mathrm{E}}/\langle I(q)\rangle_{\mathrm{T}}$.

B.2 3D cross-correlation DLS

B.2.1 Ergodic Case

As with the autocorrelation case, provided that the measured system is ergodic and thus accesses all of phase space given enough time, a long enough time average is equivalent to an ensemble average, so $\langle\cdots\rangle_{\mathrm{E}}$ can be replaced with the time average, $\langle\cdots\rangle_{\mathrm{T}}$.

B.2.2 Non-ergodic Case

Following the first few steps from the ensemble-averaged case gives

$$\begin{aligned} G_{\mathrm{I}}^{(\mathrm{T})}(q,\tau) = & \left[\langle I_1^1(q)\rangle_{\mathrm{T}}\langle I_2^1(q)\rangle_{\mathrm{T}} + \langle I_1^2(q)\rangle_{\mathrm{T}}\langle I_2^1(q)\rangle_{\mathrm{T}} + \langle I_1^2(q)\rangle_{\mathrm{T}}\langle I_2^2(q)\rangle_{\mathrm{T}}\right] \\ & + \langle I_1^1(q,t)I_2^2(q,t+\tau)\rangle_{\mathrm{T}}. \end{aligned} \tag{B.12}$$

Following [224], we divide the electric field into a time-dependent fluctuating component with zero mean and a constant component:

$$E_j^k(q,t) = E_j^{k(\mathrm{F})}(q,t) + E_j^{k(\mathrm{C})}(q), \tag{B.13}$$

with $\langle E_j^{k(\mathrm{F})}(q,t)\rangle_{\mathrm{T}} = 0$. Then

$$\begin{aligned} \langle I_j^k(q,t)\rangle_{\mathrm{T}} &= \sqrt{\frac{\epsilon_{\mathrm{s}}}{4\mu_0}}\langle E_j^k(q,t)E_j^{k*}(q,t)\rangle_{\mathrm{T}} \\ &= \sqrt{\frac{\epsilon_{\mathrm{s}}}{4\mu_0}}\left[\langle E_j^{k(\mathrm{F})}(q,t)E_j^{k(\mathrm{F})*}(q,t)\rangle_{\mathrm{T}} + E_j^{k(\mathrm{C})}(q)E_j^{k(\mathrm{C})*}(q)\right] \\ &= \langle I_j^{k(\mathrm{F})}(q,t)\rangle_{\mathrm{T}} + I_j^{k(\mathrm{C})}(q). \end{aligned} \tag{B.14}$$

Similarly,

$$\sqrt{\frac{\epsilon_{\mathrm{s}}}{4\mu_0}}\langle E_j^j(q,t)E_k^{k*}(q,t)\rangle_{\mathrm{T}} = \sqrt{\frac{\epsilon_{\mathrm{s}}}{4\mu_0}}\left[\langle E_j^{j(\mathrm{F})}(q,t)E_k^{k(\mathrm{F})*}(q,t)\rangle_{\mathrm{T}} + E_j^{j(\mathrm{C})}(q)E_k^{k(\mathrm{C})*}(q)\right]. \tag{B.15}$$

Only the first term on the right side of Eq. B.15 is pure single scattering. The second term has no fluctuations to correlate and cannot suppress multiple scattering contributions. As a reminder, neither term in Eq. B.14 suppresses multiple scattering because that equation is not a cross-correlation term.

The term outside the brackets in Eq. B.12 can be expanded, using Eq. B.13, as

$$\begin{aligned}\langle I_1^1(q,t)I_2^2(q,t+\tau)\rangle_{\mathrm{T}} = \frac{\epsilon_{\mathrm{s}}}{4\mu_0}\Big[&\langle E_1^{1(\mathrm{F})}(q,t)E_1^{1(\mathrm{F})*}(q,t)\rangle_{\mathrm{T}}\langle E_2^{2(\mathrm{F})}(q,t+\tau)E_2^{2(\mathrm{F})*}(q,t+\tau)\rangle_{\mathrm{T}}\\ &+\langle E_1^{1(\mathrm{F})}(q,t)E_2^{2(\mathrm{F})*}(q,t+\tau)\rangle_{\mathrm{T}}\langle E_1^{1(\mathrm{F})*}(q,t)E_2^{2(\mathrm{F})}(q,t+\tau)\rangle_{\mathrm{T}}\\ &+\langle E_1^{1(\mathrm{F})}(q,t)E_1^{1(\mathrm{F})*}(q,t)\rangle_{\mathrm{T}}E_2^{2(\mathrm{C})}(q)E_2^{2(\mathrm{C})*}(q)\\ &+\langle E_1^{1(\mathrm{F})}(q,t)E_2^{2(\mathrm{F})*}(q,t+\tau)\rangle_{\mathrm{T}}E_1^{1(\mathrm{C})*}(q)E_2^{2(\mathrm{C})}(q)\\ &+\langle E_1^{1(\mathrm{F})*}(q,t)E_2^{2(\mathrm{F})}(q,t+\tau)\rangle_{\mathrm{T}}E_1^{1(\mathrm{C})}(q)E_2^{2(\mathrm{C})*}(q)\\ &+\langle E_2^{2(\mathrm{F})}(q,t+\tau)E_2^{2(\mathrm{F})*}(q,t+\tau)\rangle_{\mathrm{T}}E_1^{1(\mathrm{C})}(q)E_1^{1(\mathrm{C})*}(q)\\ &+E_1^{1(\mathrm{C})}(q)E_1^{1(\mathrm{C})*}(q)\ E_2^{2(\mathrm{C})}(q)E_2^{2(\mathrm{C})*}(q)\Big].\end{aligned} \tag{B.16}$$

Here, we have used Wick's theorem in the expansion. We have also used that terms with an odd number of fluctuating components vanish; some terms also vanish for the same reason that the second term in Eq. 2.6 vanishes for $q \neq 0$.

Combining Eqs. B.12 and B.16 gives

$$\begin{aligned}G_1^{(T)}(q,\tau) =&\langle I_1(q)\rangle_{\mathrm{T}}\langle I_2(q)\rangle_{\mathrm{T}} + \frac{\epsilon_{\mathrm{s}}}{4\mu_0}\left\{\left|\langle E_1^{1(\mathrm{F})}(q,t)E_2^{2(\mathrm{F})*}(q,t+\tau)\rangle_{\mathrm{T}}\right|^2\right.\\ &\left.+2\mathrm{Re}\left[\langle E_1^{1(\mathrm{F})}(q,t)E_2^{2(\mathrm{F})*}(q,t+\tau)\rangle_{\mathrm{T}}E_1^{1(\mathrm{C})*}(q)E_2^{2(\mathrm{C})}(q)\right]\right\}.\end{aligned} \tag{B.17}$$

Eq. B.17 can be simplified if the $2\mathrm{Re}[\cdots]$ term can be rewritten as $2|\cdots|$. This is only true if $\langle E_1^{1(\mathrm{F})}(q,t)E_2^{2(\mathrm{F})*}(q,t+\tau)\rangle_{\mathrm{T}}E_1^{1(\mathrm{C})*}(q)E_2^{2(\mathrm{C})}(q) \in \mathbb{R}$. Following [224],

$$E(q,t) = \sum_{j=1}^{N} b_j \exp\left[\mathrm{i}\mathbf{q}\cdot\mathbf{r}_j(t)\right] \tag{B.18}$$

with $\mathbf{r}_j(t) = \mathbf{R}_j + \mathbf{\Delta}_j(t)$ and $\langle \mathbf{\Delta}_j(t) \rangle_{\mathrm{T}} = 0$,

$$E^{(\mathrm{F})}(q,t) = \sum_{j=1}^{N} b_j \exp\left[\mathrm{i}\mathbf{q}\cdot\mathbf{R}_j\right] \left\{\exp\left[\mathrm{i}\mathbf{q}\cdot\mathbf{\Delta}_j(t)\right] - w_j\right\} \tag{B.19}$$

with $w_j = \langle \exp\left[\mathrm{i}\mathbf{q}\cdot\mathbf{\Delta}_j(t)\right]\rangle_{\mathrm{T}}$, and

$$E^{(\mathrm{C})}(q) = \sum_{j=1}^{N} b_j w_j \exp\left[\mathrm{i}\mathbf{q}\cdot\mathbf{R}_j\right]. \tag{B.20}$$

Consider that

$$E_1^{1(\mathrm{C})*}(q) E_2^{2(\mathrm{C})}(q) = \sum_{j=1}^{N}\sum_{k=1}^{N} b_j b_k w_j^* w_k \exp\left[-\mathrm{i}\mathbf{q}\cdot(\mathbf{R}_j - \mathbf{R}_k)\right]. \tag{B.21}$$

Complex conjugating and switching the dummy indices $j \leftrightarrow k$ changes nothing. Thus, $E_1^{1(\mathrm{C})*}(q) E_2^{2(\mathrm{C})}(q) \in \mathbb{R}$. What about the fluctuating part?

Following [224],

$$w_j = \langle \exp\left[\mathrm{i}\mathbf{q}\cdot\mathbf{\Delta}(t)\right]\rangle_{\mathrm{T}} = \langle \exp\left[\mathrm{i}\mathbf{q}\cdot\mathbf{\Delta}(t+\tau)\right]\rangle_{\mathrm{T}}. \tag{B.22}$$

$$\begin{aligned}
&\langle E_1^{1(\mathrm{F})}(q,t) E_2^{2(\mathrm{F})*}(q,t+\tau)\rangle_{\mathrm{T}} \\
&\quad = \Bigg\langle \sum_{j=1}^{N}\sum_{k=1}^{N} b_j b_k \exp\left[\mathrm{i}\mathbf{q}\cdot(\mathbf{R}_j - \mathbf{R}_k)\right] \\
&\qquad \times \left\{\exp\left[\mathrm{i}\mathbf{q}\cdot\mathbf{\Delta}_j(t)\right] - w_j\right\} \left\{\exp\left[\mathrm{i}\mathbf{q}\cdot\mathbf{\Delta}_k(t+\tau)\right] - w_k^*\right\} \Bigg\rangle_{\mathrm{T}} \\
&\quad = \sum_{j=1}^{N}\sum_{k=1}^{N} b_j b_k \exp\left[\mathrm{i}\mathbf{q}\cdot(\mathbf{R}_j - \mathbf{R}_k)\right] \\
&\qquad \times \left\{\langle \exp\left[\mathrm{i}\mathbf{q}\cdot\mathbf{\Delta}_j(t)\right] \exp\left[-\mathrm{i}\mathbf{q}\cdot\mathbf{\Delta}_k(t+\tau)\right]\rangle_{\mathrm{T}} \right. \\
&\qquad\quad \left. - \langle \exp\left[\mathrm{i}\mathbf{q}\cdot\mathbf{\Delta}_j(t)\right]\rangle_{\mathrm{T}} \langle \exp\left[-\mathrm{i}\mathbf{q}\cdot\mathbf{\Delta}_k(t+\tau)\right]\rangle_{\mathrm{T}} \right\},
\end{aligned} \tag{B.23}$$

where in the second equality terms have been collected and some have cancelled. If this is real, it should be invariant under complex conjugation and switching of the dummy indices:

$$\begin{aligned}
&\langle E_1^{1(\mathrm{F})}(q,t) E_2^{2(\mathrm{F})*}(q,t+\tau)\rangle_{\mathrm{T}}^* \\
&\quad = \sum_{j=1}^{N}\sum_{k=1}^{N} b_j b_k \exp\left[\mathrm{i}\mathbf{q}\cdot(\mathbf{R}_j - \mathbf{R}_k)\right] \\
&\qquad \times \left\{\langle \exp\left[\mathrm{i}\mathbf{q}\cdot\mathbf{\Delta}_j(t+\tau)\right] \exp\left[-\mathrm{i}\mathbf{q}\cdot\mathbf{\Delta}_k(t)\right]\rangle_{\mathrm{T}} \right. \\
&\qquad\quad \left. - \langle \exp\left[\mathrm{i}\mathbf{q}\cdot\mathbf{\Delta}_j(t+\tau)\right]\rangle_{\mathrm{T}} \langle \exp\left[-\mathrm{i}\mathbf{q}\cdot\mathbf{\Delta}_k(t)\right]\rangle_{\mathrm{T}} \right\}.
\end{aligned} \tag{B.24}$$

From Eq. B.22, the product of averages on the last line of Eq. B.24 is the same as the corresponding product in Eq. B.23. I have not been able to show that the first term inside the curly brackes of both equations are the same, although they are certainly similar. If they are the same, then only the absolute value of the cross-correlation term matters and $G_{\mathrm{I}}(q,\tau)$ can be defined following arguments similar to the autocorrelation case, albeit after taking into account complications from the presence of multiple scattering.

Looking back at Eq. B.17, there are three terms on the right side. First, the product of the time-averaged intensities measured by each detector. Second, a term which is analogous to Eq. 2.7. Both of these terms are similar to those in the ensemble-averaged Siegert relation. There is also a third term which additionally complicates matters: a cross term which contains both fluctuating and non-fluctuating electric field components.

The first term is something we can measure experimentally.

The second and third terms both contain a time-averaged cross-correlation term. In [224], which dealt with non-ergodic scattering measured using regular DLS, the analogous term could be expressed in terms of the ensemble-averaged intensity (another property that could be measured experimentally) and the dynamic structure factor (i.e. the electric field autocorrelation function). [226] makes a similar claim in their paper's Eqs. 9 and 10. However, the analogy they make with [224] is not mathematically rigorous. Also, Eq. 8 in [226] is incorrect, but they use it later to derive their Eq. 13. Finally, [226] does not take multiple scattering into account correctly. As mentioned above, only the fluctuating component of the electric field can suppress multiple scattering, meaning that the cross term in Eq. B.17 contains multiple scattering contributions. This fact is completely missed in [226], who insert the multiple scattering correction by hand at the end, with no mathematical reason for doing so. Unfortunately the correct solution to the problem would be extremely complicated because of the presence of multiple scattering, which is not an issue in [224].

In order to correctly write the time-averaged intensity cross-correlation function in terms of the ensemble-averaged electric field correlation function and experimental observables, all of these things must be addressed. Thus, when measuring very slowly-relaxing samples, rather than attempt to correct a shorter measurement for non-ergodicity, we increase the

measurement times to hours or days per point to ensure ergodicity.

Bibliography

[1] J. Varberg, B. Gratuze, and F. Kaul, "Between Egypt, Mesopotamia and Scandinavia: Late Bronze Age glass beads found in Denmark," *J. Archaeol. Sci.* **54**, 168 (2015).

[2] A. Greer and N. Mathur, "Materials science: Changing face of the chameleon," *Nature* **437**, 1246 (2005).

[3] W. Klement Jr., R. Willens, and P. Duwez, "Non-crystalline structure in solidified gold-silicon alloys," *Nature* **187**, 869 (1960).

[4] W. Wang, C. Dong, and C. Shek, "Bulk metallic glasses," *Mat. Sci. Eng. R* **44**, 45 (2004).

[5] J. Disa, J. Vossoughi, and N. Goldberg, "A comparison of obsidian and surgical steel scalpel wound healing in rats," *Plast. Reconstr. Surg.* **92**, 884 (1993).

[6] J.-P. Hansen, *Theory of Simple Liquids*, 3rd ed. (Elsevier Science B.V., Amsterdam, 2006).

[7] C. Herbst, R. Cook, and H. King Jr., "Density-mediated transport and the glass transition: high pressure viscosity measurements in the diamond anvil cell," *J. Non-Cryst. Solids* **172-174**, 265 (1994).

[8] T. Egami and Y. Waseda, "Atomic size effect on the formability of metallic glasses," *J. Non-Cryst. Solids* **64**, 113 (1984).

[9] P. Pusey and W. van Megen, "Observation of a glass transition in suspensions of spherical colloidal particles," *Phys. Rev. Lett.* **59**, 2083 (1987).

[10] W. van Megen and S. Underwood, "Dynamic-light-scattering study of glasses of hard colloidal spheres," *Phys. Rev. E* **47**, 248 (1993).

[11] D. Cangialosi, "Dynamics and thermodynamics of polymer glasses," *J. Phys.: Condens. Matter* **26**, 153101 (2014).

[12] K. Binder and A. Young, "Spin glasses: Experimental facts, theoretical concepts, and open questions," *Rev. Mod. Phys.* **58**, 801 (1986).

[13] J. Mydosh, "Spin glasses: redux: an updated experimental/materials survey," *Rep. Prog. Phys.* **78**, 052501 (2015).

[14] J. Zhao, S. Simon, and G. McKenna, "Using 20-million-year-old amber to test the super-Arrhenius behavior of glass-forming systems," *Nat. Commun.* **4**, 1783 (2013).

[15] J. Zhao, E. Ragazzi, and G. McKenna, "Something about amber: fictive temperature and glass transition temperature of extremely old glasses from copal to Triassic amber," *Polymer* **54**, 7041 (2013).

[16] J. Zhao and G. McKenna, "The apparent activation energy and dynamic fragility of ancient ambers," *Polymer* **55**, 2246 (2014).

[17] E. Pogna, C. Rodríguez-Tinoco, G. Cerullo, C. Ferrante, J. Rodríguez-Viejo, and T. Scopigno, "Probing equilibrium glass flow up to exapoise viscosities," *Proc. Natl. Acad. Sci. USA* **112**, 2331 (2015).

[18] U. Bengtzelius, W. Götze, and A. Sjölander, "Dynamics of supercooled liquids and the glass transition," *J. Phys. C* **17**, 5915 (1984).

[19] W. Götze and L. Sjögren, "Relaxation processes in supercooled liquids," *Rep. Prog. Phys.* **55**, 241 (1992).

[20] X. Xia and P. Wolynes, "Fragilities of liquids predicted from the random first order transition theory of glasses," *Proc. Natl. Acad. Sci. USA* **97**, 2990 (2000).

[21] V. Lubchenko and P. Wolynes, "Theory of structural glasses and supercooled liquids," *Annu. Rev. Phys. Chem.* **58**, 235 (2007).

[22] Z. Zhang, N. Xu, D. Chen, P. Yunker, A. Alsayed, K. Aptowicz, P. Habdas, A. Liu, S. Nagel, and A. Yodh, "Thermal vestige of the zero-temperature jamming transition," *Nature* **459**, 230 (2009).

[23] A. Ikeda, L. Berthier, and P. Sollich, "Unified study of glass and jamming rheology in soft particle systems," *Phys. Rev. Lett.* **109**, 018301 (2012).

[24] A. Ikeda, L. Berthier, and P. Sollich, "Disentangling glass and jamming physics in the rheology of soft materials," *Soft Matter* **9**, 7669 (2013).

[25] E. Weeks, J. Crocker, and D. Weitz, "Short- and long-range correlated motion observed in colloidal glasses and liquids," *J. Phys.: Condens. Matter* **19**, 205131 (2007).

[26] M. Helgeson, N. Wagner, and D. Vlassopoulos, "Viscoelasticity and shear melting of colloidal star polymer glasses," *J. Rheol.* **51**, 297 (2007).

[27] K. Pham, G. Petekidis, D. Vlassopoulos, S. Egelhaaf, W. Poon, and P. Pusey, "Yielding behavior of repulsion- and attraction-dominated colloidal glasses," *J. Rheol.* **52**, 649 (2008).

[28] A. Le Grand and G. Petekidis, "Effects of particle softness on the rheology and yielding of colloidal glasses," *Rheol. Acta* **47**, 579 (2008).

[29] V. Martinez, G. Bryant, and W. van Megen, "Slow dynamics and aging of a colloidal hard sphere glass," *Phys. Rev. Lett.* **101**, 135702 (2008).

[30] D. El Masri, G. Brambilla, M. Pierno, G. Petekidis, A. Schofield, L. Berthier, and L. Cipelletti, "Dynamic light scattering measurements in the activated regime of dense colloidal hard spheres," *J. Stat. Mech.* **2009**, P07015 (2009).

[31] C. Christopoulou, G. Petekidis, B. Erwin, M. Cloitre, and D. Vlassopoulos, "Ageing and yield behaviour in model soft colloidal glasses," *Phil. Trans. R. Soc. A* **367**, 5051 (2009).

[32] G. Ovarlez, Q. Barral, and P. Coussot, "Three-dimensional jamming and flows of soft glassy materials," *Nature Mater.* **9**, 115 (2010).

[33] B. Erwin, D. Vlassopoulos, M. Gauthier, and M. Cloitre, "Unique slow dynamics and aging phenomena in soft glassy suspensions of multiarm star polymers," *Phys. Rev. E* **83**, 061402 (2011).

[34] G. Hunter and E. Weeks, "The physics of the colloidal glass transition," *Rep. Prog. Phys.* **75**, 066501 (2012).

[35] J. Crassous, L. Casal-Dujat, M. Medebach, M. Obiols-Rabasa, R. Vincent, F. Reinhold, V. Boyko, I. Willerich, A. Menzel, C. Moitzi, B. Rech, and P. Schurtenberger, "Structure and dynamics of soft repulsive colloidal suspensions in the vicinity of the glass transition," *Langmuir* **29**, 10346 (2013).

[36] Y. Joshi, "Dynamics of colloidal glasses and gels," *Annu. Rev. Chem. Biomol. Eng.* **5**, 181 (2014).

[37] C. Amann, D. Denisov, M. Dang, B. Struth, P. Schall, and M. Fuchs, "Shear-induced breaking of cages in colloidal glasses: Scattering experiments and mode coupling theory," *J. Chem. Phys.* **143**, 034505 (2015).

[38] Y. Wen, J. Schaefer, and L. Archer, "Dynamics and rheology of soft colloidal glasses," *ACS Macro. Lett.* **4**, 119 (2015).

[39] W. van Megen and P. Pusey, "Dynamic light-scattering study of the glass transition in a colloidal suspension," *Phys. Rev. A* **43**, 5429 (1991).

[40] T. Mason and D. Weitz, "Linear viscoelasticity of colloidal hard sphere suspensions near the glass transition," *Phys. Rev. Lett.* **75**, 2770 (1995).

[41] W. Kegel and A. van Blaaderen, "Direct observation of dynamical heterogeneities in colloidal hard-sphere suspensions," *Science* **287**, 290 (2000).

[42] E. Weeks, J. Crocker, A. Levitt, A. Schofield, and D. Weitz, "Three-dimensional direct imaging of structural relaxation near the colloidal glass transition," *Science* **287**, 627 (2000).

[43] C. Angell, K. Ngai, G. McKenna, P. McMillan, and S. Martin, "Relaxation in glass-forming liquids and amorphous solids," *J. Appl. Phys.* **88**, 3113 (2000).

[44] S. Auer and D. Frenkel, "Suppression of crystal nucleation in polydisperse colloids due to increase of the surface free energy," *Nature* **413**, 711 (2001).

[45] B. Sierra-Martín and A. Fernández-Nieves, "Phase and non-equilibrium behaviour of microgel suspensions as a function of particle stiffness," *Soft Matter* **8**, 4141 (2012).

[46] J. Roovers, "Concentration dependence of the relative viscosity of star polymers," *Macromolecules* **27**, 5359 (1994).

[47] G. Romeo, A. Fernández-Nieves, H. Wyss, D. Acierno, and D. Weitz, "Temperature-controlled transitions between glass, liquid, and gel states in dense p-NIPA suspensions," *Adv. Mater.* **22**, 3441 (2010).

[48] J.-J. Liétor-Santos, B. Sierra-Martín, R. Vavrin, Z. Hu, U. Gasser, and A. Fernández-Nieves, "Deswelling microgel particles using hydrostatic pressure," *Macromolecules* **42**, 6225 (2009).

[49] A. Fernández-Nieves, A. Fernández-Barbero, B. Vincent, and F. de las Nieves, "Charge controlled swelling of microgel particles," *Macromolecules* **33**, 2114 (2000).

[50] A. Fernández-Nieves, A. Fernández-Barbero, and F. de las Nieves, "Salt effects over the swelling of ionized mesoscopic gels," *J. Chem. Phys.* **115**, 7644 (2001).

[51] H. Vogel, "Das Temperaturabhängigkeitsgesetz der Viskosität von Flüssigkeiten," *Phys. Z.* **22**, 645 (1921).

[52] G. Fulcher, "Analysis of recent measurements of the viscosity of glasses," *J. Am. Ceram. Soc.* **8**, 339 (1925).

[53] G. Tamman and W. Hesse, "Die Abhängigkeit der Viskosität von der Temperatur bei unterkühlten Flüssigkeiten," *Z. Anorg. Allg. Chem.* **156**, 245 (1926).

[54] M. Pelaez-Fernandez, A. Souslov, L. Lyon, P. Goldbart, and A. Fernández-Nieves, "Impact of single-particle compressibility on the fluid-solid phase transition for ionic microgel suspensions," *Phys. Rev. Lett.* **114**, 098303 (2015).

[55] R. Borrega, M. Cloitre, I. Betremieux, B. Ernst, and L. Leibler, "Concentration dependence of the low-shear viscosity of polyelectrolyte micro-networks: From hard spheres to soft microgels," *Europhys. Lett.* **47**, 729 (1999).

[56] M. Heuberger, T. Drobek, and N. Spencer, "Interaction forces and morphology of a protein-resistent poly(ethylene glycol) layer," *Biophys. J.* **88**, 495 (2005).

[57] Z. Meng, M. Smith, and L. Lyon, "Temperature-programmed synthesis of micron-sized multi-responsive microgels," *Colloid Polym. Sci.* **287**, 277 (2009).

[58] M. Shibayama, S. Mizutani, and S. Nomura, "Thermal properties of copolymer gels containing *N*-Isopropylacrylamide," *Macromolecules* **29**, 2019 (1996).

[59] K. Kratz, T. Hellweg, and W. Eimer, "Influence of charge density on the swelling of colloidal poly(*N*-isopropylacrylamide-co-acrylic acid) microgels," *Colloids Surf., A* **170**, 137 (2000).

[60] C. Jones and L. Lyon, "Synthesis and characterization of multiresponsive core-shell microgels," *Macromolecules* **33**, 8301 (2000).

[61] T. Hoare and R. Pelton, "Functionalized microgel swelling: Comparing theory and experiment," *J. Phys. Chem. B* **111**, 11895 (2007).

[62] M. Muluneh, J. Sprakel, H. Wyss, J. Mattsson, and D. Weitz, "Direct visualization of pH-dependent evolution of structure and dynamics in microgel suspensions," *J. Phys.: Condens. Matter* **23**, 505101 (2011).

[63] T. Si, Y. Wang, W. Wei, P. Lv, G. Ma, and Z. Su, "Effect of acrylic acid weight percentage on the pore size in poly(N-isopropylacrylamide-*co*-acrylic acid) microspheres," *React. Funct. Polym.* **71**, 728 (2011).

[64] G. Romeo, L. Imperiali, J.-W. Kim, A. Fernández-Nieves, and D. Weitz, "Origin of de-swelling and dynamics of dense ionic microgel suspensions," *J. Chem. Phys.* **136**, 124905 (2012).

[65] J. Clara-Rahola, A. Fernández-Nieves, B. Sierra-Martín, A. South, L. Lyon, J. Kohlbrecher, and A. Fernández-Barbero, "Structural properties of thermoresponsive poly(N-isopropylacrylamide-poly(ethyleneglycol) microgels," *J. Chem. Phys.* **136**, 214903 (2012).

[66] J. Virtanen, C. Baron, and H. Tenhu, "Grafting of poly(N-isopropylacrylamide) with poly(ethylene oxide) under various reaction conditions," *Macromolecules* **33**, 336 (2000).

[67] R. Motokawa, K. Morishita, S. Koizumi, T. Nakahira, and M. Annaka, "Thermosensitive diblock copolymer of poly(N-isopropylacrylamide) and poly(ethylene glycol) in water: polymer preparation and solution behavior," *Macromolecules* **38**, 5748 (2005).

[68] A. Einstein, "Eine neue Bestimmung der Moleküldimensionen," *Annln. Phys.* **19**, 289 (1906).

[69] A. Einstein, "Berichtigung zu meiner Arbeit: "Eine neue Bestimmung der Moleküldimensionen"," *Annln. Phys.* **34**, 591 (1911).

[70] G. Batchelor, "The effect of Brownian motion on the bulk stress in a suspension of spherical particles," *J. Fluid Mech.* **83**, 97 (1977).

[71] J. Brady and M. Vicic, "Normal stresses in colloidal dispersions," *J. Rheol.* **39**, 545 (1995).

[72] D. Lide, editor, *CRC Handbook of Chemistry and Physics*, 70th ed. (CRC Press, Boca Raton, Florida, 1990).

[73] J. Watson, R. Basu, and J. Sengers, "An improved representative equation for the dynamic viscosity of water substance," *J. Phys. Chem. Ref. Data* **9**, 1255 (1980).

[74] J. Dhont, *An Introduction to Dynamics of Colloids*, 2nd ed. (Elsevier Science B.V., Amsterdam, 2003).

[75] K. Schätzel, "Suppression of multiple scattering by photon cross-correlation techniques," *J. Mod. Opt.* **38**, 1849 (1991).

[76] W. Brown, *Dynamic Light Scattering: The Method and Some Applications* (Oxford Science Publications, Oxford, 1993).

[77] A. Routh and W. Zimmerman, "The diffusion coefficient of a swollen microgel particle," *J. Colloid Interface Sci.* **261**, 547 (2003).

[78] K. Pearson, "On the criterion that a given system of deviations from the probable in the case of a correlated system of variables is such that it can reasonably be supposed to have arisen from random sampling," *Philos. Mag. 5* **50**, 157 (1900).

[79] D. Koppel, "Analysis of macromolecular polydispersity in intensity correlation spectroscopy: The method of cumulants," *J. Chem. Phys.* **57**, 4814 (1972).

[80] A. Scotti, W. Liu, J. Hyatt, E. Herman, H. Choi, J. Kim, L. Lyon, U. Gasser, and A. Fernández-Nieves, "The CONTIN algorithm and its application to determine the size distribution of microgel suspensions," *J. Chem. Phys.* **142**, 234905 (2015).

[81] G. Fournet, *Étude théorique et expérimentale de la diffusion des Rayons X par les ensembles denses de particlules*, PhD thesis L'Universit'e de Paris 1951.

[82] L. Blum and G. Stell, "Polydisperse systems. I. Scattering function for polydisperse fluids of hard or permeable spheres," *J. Chem. Phys.* **71**, 42 (1979).

[83] A. Vrij, "Light scattering of a concentrated multicomponent system of hard spheres in the Percus-Yevick approximation," *J. Chem. Phys.* **69**, 1742 (1978).

[84] A. Vrij, "Mixtures of hard spheres in the Percus-Yevick approximation. Light scattering at finite angles," *J. Chem. Phys.* **71**, 3267 (1979).

[85] P. van Beurten and A. Vrij, "Polydispersity effects in the small-angle scattering of concentrated solutions of colloidal spheres," *J. Chem. Phys.* **74**, 2744 (1981).

[86] W. Griffith, R. Triolo, and A. Compere, "Analytical structure function of a polydisperse Percus-Yevick fluid with Schulz (gamma) distributed diameters," *Phys. Rev. A* **33**, 2197 (1986).

[87] M. Ginoza and M. Yasutomi, "Analytical structure factors for colloidal fluids with size and interaction polydispersities," *Phys. Rev. E* **58**, 3329 (1998).

[88] M. Ginoza and M. Yasutomi, "Analytical model of the static structure factor of a colloidal dispersion: interaction polydispersity effect," *Mol. Phys.* **93**, 399 (1998).

[89] U. Gasser, J. Hyatt, J.-J. Liétor-Santos, E. Herman, L. Lyon, and A. Fernández-Nieves, "Form factor of pNIPAM microgels in overpacked states," *J. Chem. Phys.* **141**, 034901 (2014).

[90] G. Senatore and L. Blum, "Size effects and polydispersity in ionic micellar solutions within the mean spherical approximation," *J. Phys. Chem.* **89**, 2676 (1985).

[91] M. Ginoza and M. Yasutomi, "Measurable structure factor of a multi-species polydisperse Percus-Yevick fluid with Schulz distributed diameters," *J. Phys. Soc. Jpn.* **68**, 2292 (1999).

[92] D. Frenkel, R. Vos, C. de Kruif, and A. Vrij, "Structure factors of polydisperse systems of hard spheres: A comparison of Monte Carlo simulations and Percus-Yevick theory," *J. Chem. Phys.* **84**, 4625 (1986).

[93] F. Scheffold and T. Mason, "Scattering from highly packed disordered colloids," *J. Phys.: Condens. Matter* **21**, 332102 (2009).

[94] G. Yevick and J. Percus, "New approach to the many-body problem," *Phys. Rev.* **101**, 1186 (1956).

[95] J. Percus and G. Yevick, "Dynamical considerations on a new approach to the many-body problem," *Phys. Rev.* **101**, 1192 (1956).

[96] J. Percus and G. Yevick, "Statistical approach to the domain of action of collective co-ordinates in the many body problem," *Nuovo Cimento* **5**, 1057 (1957).

[97] L. Ornstein and F. Zernike, "Accidental deviations of density and opalescence at the critical point of a single substance," in *Proceedings of the Royal Netherlands Academy of Arts and Sciences* volume 17 pp. 793–806 1914.

[98] J. Percus and G. Yevick, "Analysis of classical statistical mechanics by means of collective coordinates," *Phys. Rev.* **110** (1958).

[99] M. Wertheim, "Exact solution of the Percus-Yevick integral equation for hard spheres," *Phys. Rev. Let.* **10**, 321 (1963).

[100] E. Thiele, "Equation of state for hard spheres," *J. Chem. Phys.* **39**, 474 (1963).

[101] N. Ashcroft and J. Lekner, "Structure and resistivity of liquid metals," *Phys. Rev.* **145**, 83 (1966).

[102] J. Lebowitz, "Exact solution of generalized Percus-Yevick equation for a mixture of hard spheres," *Phys. Rev.* **133**, A895.

[103] R. Baxter, "Ornstein-Zernike relation and Percus-Yevick approximation for fluid mixtures," *J. Chem. Phys.* **52**, 4559 (1970).

[104] M. Ginoza and M. Yasutomi, "Mathematical comment on adhesive hard sphere models for fluids," *Mol. Phys.* **87**, 593 (1996).

[105] M. Yasutomi and M. Ginoza, "Analytical solution of Ornstein-Zernike equation for adhesive-hard-sphere Yukawa fluids," *Mol. Phys.* **89**, 1755 (1996).

[106] M. Ginoza and M. Yasutomi, "Static structure factor for a colloidal dispersion with size and "charge" polydispersities: Mean spherical approximation model in hard-sphere Yukawa fluids," *Phys. Rev. E* **59**, 2060 (1999).

[107] R.-S. Cheng, H. Yang, X.-H. Yan, Z.-L. Wang, and L. Li, "The solvation and desolvation process in the course of coil-globule transition of aqueous poly(*N*-isopropylacrylamide) solution," *Chem. J. Chinese U.* **22**, 1262 (2001).

[108] B. Evans, K. Hocking, M. Osgood, I. Voskresensky, J. Dmowska, K. Kilchrist, C. Brophy, and C. Duvall, "MK2 inhibitory peptide delivered in nanopolyplexes prevents vascular graft intimal hyperplasia," *Sci. Transl. Med.* **7**, 291ra95 (2015).

[109] Y. Liu, R. Lipowsky, and R. Dimova, "Concentration dependence of the interfacial tension for aqueous two-phase polymer solutions of dextran and polyethylene glycol," *Langmuir* **28**, 3831 (2012).

[110] A. Guinier, "La diffusion des rayon X sous les très faibles angles appliquée à l'étude de fines particules et de suspensions colloidales," *C.R. Acad. Sci.* **206**, 1374 (1938).

[111] W. Dozier, J. Huang, and L. Fetters, "Colloidal nature of star polymer dilute and semidilute solutions," *Macromolecules* **24**, 2810 (1991).

[112] P.-G. de Gennes, *Scaling Concepts in Polymer Physics* (Cornell University Press, Ithaca, New York, 1979).

[113] P. Debye and A. Bueche, "Scattering by an inhomogeneous solid," *J. Appl. Phys.* **20**, 518 (1949).

[114] W. Wu, M. Shibayama, S. Roy, H. Kurokawa, L. Coyne, S. Nomura, and R. Stein, "Physical gels of aqueous poly(vinyl alcohol) solutions: A small-angle neutron-scattering study," *Macromolecules* **23**, 2245 (1990).

[115] M. Daoud and J. Cotton, "Star shaped polymers: a model for the conformation and its concentration dependence," *J. Physique* **43**, 531 (1982).

[116] N. Baddour, "Operational and convolution properties of three-dimensional Fourier transforms in spherical polar coordinates," *J. Opt. Soc. Am. A* **27**, 2144 (2010).

[117] M. Stieger, W. Richtering, J. Pedersen, and P. Lindner, "Small-angle neutron scattering study of structural changes in temperature sensitive microgel colloids," *J. Chem. Phys.* **120**, 6197 (2004).

[118] J.-J. Liétor-Santos and A. Fermández-Nieves, "Motion of microgels in electric fields," *Adv. Colloid Interface Sci.* **147-148**, 178 (2009).

[119] A. Apelblat and E. Manzurola, "Volumetric properties of water, and solutions of sodium chloride and potassium chloride at temperatures from $T = 277.15$ K to $T = 343.15$ K at molalities of (0.1, 0.5, and 1.0) $\mathrm{mol \cdot kg^{-1}}$," *J. Chem. Thermodynamics* **31**, 869 (1999).

[120] D. James, "The thermal diffusivity of ice and water between -40 and $+60$ °C," *J. Mat. Sci.* **3**, 540 (1968).

[121] W. Heitz and J. Westwater, "Critical Rayleigh numbers for natural convection of water confined in square cells with L/D from 0.5 to 8," *J. Heat Transfer* **93**, 188 (1971).

[122] R. Lucke, "Counting statistics for nonnegligible dead time corrections," *Rev. Sci. Instrum.* **47**, 766 (1976).

[123] K. Schätzel, R. Kalström, B. Stampa, and J. Ahrens, "Correction of detection-system dead-time effects on photon-correlation functions," *J. Opt. Soc. Am. B* **6**, 937 (1989).

[124] P. Wyatt, "Light scattering and the absolute characterization of macromolecules," *Anal. Chim. Acta* **272**, 1 (1993).

[125] I. Schoen and E. Ellsworth, "The disposable glass culture tube as a cuvette," *J. Clin. Pathol.* **23**, 825 (1970).

[126] D. Capriles-González, B. Sierra-Martín, A. Fernández-Nieves, and A. Fernández-Barbero, "Coupled deswelling of multiresponse microgels," *J. Phys. Chem. B* **112**, 12195 (2008).

[127] A. Lele, M. Hirve, M. Badiger, and R. Mashelkar, "Predictions of bound water content in poly(N-isopropylacrylamide) gel," *Macromolecules* **30**, 157 (1997).

[128] H. Schild, "Poly(N-isopropylacrylamide): Experiment, theory, and application," *Prog. Polym. Sci.* **17**, 163 (1992).

[129] I. Varga, T. Gilányi, R. Mészáros, G. Filipcsei, and M. Zrínyi, "Effects of cross-link density on the internal structure of poly(N-isopropylacrylamide) microgels," *J. Phys. Chem. B* **105**, 9071 (2001).

[130] J. Zhao, C. Gao, and D. Liu, "The extended Q-range small-angle neutron scattering diffractometer at the SNS," *J. Appl. Cryst.* **43**, 1068 (2010).

[131] J. Pedersen, D. Posselt, and K. Mortensen, "Analytical treatment of the resolution function for small-angle scattering," *J. Appl. Cryst.* **23**, 321 (1990).

[132] R. May, *Neutron Data Booklet*, 2nd ed. (Old City Publishing, Philadelphia, Pennsylvania, 2003).

[133] P. Glasoe and F. Long, "Use of glass electrodes to measure acidities in deuterium oxide," *J. Phys. Chem.* **64**, 188 (1960).

[134] A. Covington, M. Paabo, R. Robinson, and R. Bates, "Use of the glass electrode in deuterium oxide and the relation between the standardized pD ($\mathrm{pa_D}$) scale and the operational pH in heavy water," *Anal. Chem.* **40**, 700 (1968).

[135] A. Krężel and W. Bal, "A formula for correlating $\mathrm{p}K_\mathrm{a}$ values determined in $\mathrm{D_2O}$ and $\mathrm{H_2O}$," *J. Inorg. Biochem.* **98**, 161 (2004).

[136] A. Guinier and G. Fournet, "Small Angle Scattering of X-rays," *J. Wiley & Sons, New York* (1955).

[137] H. Bale and P. Schmidt, "Small-angle X-Ray-scattering investigation of submicroscopic porosity with fractal properties," *Phys. Rev. Lett.* **53**, 596 (1984).

[138] A. Fernández-Barbero, A. Fernández-Nieves, I. Grillo, and E. López-Cabarcos, "Structural modifications in the swelling of inhomogeneous microgels by light and neutron scattering," *Phys. Rev. E* **66**, 051803 (2002).

[139] Z. Ahmed, E. Gooding, K. Pimenov, L. Wang, and S. Asher, "UV resonance Raman determination of molecular mechanism of poly(N-isopropylacrylamide) volume phase transition," *J. Phys. Chem. B* **113**, 4248 (2009).

[140] Y. Weng, Y. Ding, and G. Zhang, "Microcalorimetric investigation on the lower critical Solution temperature behavior of N-isopropylacrylamide-*co*-acrylic acid copolymer in aqueous solution," *J. Phys. Chem. B* **110**, 11813 (2006).

[141] M. Villarino, "The probability of a run," *arXiv* , 0511652v1 (2008).

[142] V. Borue and I. Erukhimovich, "A statistical theory of weakly charged polyelectrolytes: fluctuations, equation of state and microphase separation," *Macromolecules* **21**, 3240 (1988).

[143] M. Shibayama, T. Tanaka, and C. Han, "Small-angle neutron scattering study on weakly charged temperature sensitive polymer gels," *J. Chem. Phys.* **97**, 6842 (1992).

[144] M. Shibayama, T. Tanaka, and C. Han, "Small angle neutron scattering study on poly(N-isopropyl acrylamide) gels near their volume-phase transition temperature," *J. Chem. Phys.* **97**, 6829 (1992).

[145] T. Odijk, "Polyelectrolytes near the rod limit," *J. Polym. Sci., Polym. Phys. Ed.* **15**, 477 (1977).

[146] J. Skolnick and M. Fixman, "Electrostatic persistence length of a wormlike polyelectrolyte," *Macromolecules* **10**, 944 (1977).

[147] A. Brown, S. Stabenfeldt, B. Ahn, R. Hannan, K. Dhada, E. Herman, V. Stefanelli, N. Guzzetta, A. Alexeev, W. Lam, L. Lyon, and T. Barker, "Ultrasoft microgels displaying emergent platelet-like behaviours," *Nature Mater.* **13**, 1108 (2014).

[148] J. Gao and B. Frisken, "Cross-linker-free N-isopropylacrylamide gel nanospheres," *Langmuir* **19**, 5212 (2003).

[149] J. Gao and B. Frisken, "Influence of reaction conditions on the synthesis of self-crosslinked N-isopropylacrylamide microgels," *Langmuir* **19**, 5217 (2003).

[150] R. Lionberger and W. Russel, "High frequency modulus of hard sphere colloids," *J. Rheol.* **38**, 1885 (1994).

[151] W. van Megen, V. Martinez, and G. Bryant, "Arrest of flow and emergence of activated processes at the glass transition of a suspension of particles with hard spherelike interactions," *Phys. Rev. Lett.* **102**, 168301 (2009).

[152] T. Mason, J. Bibette, and D. Weitz, "Elasticity of compressed emulsions," *Phys. Rev. Lett.* **75**, 2051 (1995).

[153] F. Cardinaux, T. Mason, and F. Scheffold, "Elasticity and glassy dynamics of dense emulsions," *AIP Conf. Proc.* **1518**, 222 (2013).

[154] D. Durian, "Foam mechanics at the bubble scale," *Phys. Rev. Lett.* **75**, 4780 (1995).

[155] B. Herzhaft, S. Kakadijian, and M. Moan, "Measurement and modeling of the flow behavior of aqueous foams using a recirculating pipe rheometer," *Colloids Surf. A* **263**, 153 (2005).

[156] D. Richter, O. Jucknischke, L. Willner, L. Fetters, M. Lin, J. Huang, J. Roovers, C. Toporovski, and L. Zhou, "Scaling properties and ordering phenomena of star polymers in solution," *J. de Phys. IV* **3**, 3 (1993).

[157] G. Foffi, F. Sciortino, P. Tartaglia, E. Zaccarelli, F. Lo Verso, L. Reatto, K. Dawson, and C. Likos, "Structural arrest in dense star-polymer solutions," *Phys. Rev. Lett.* **90**, 238301 (2003).

[158] S. Rogers, P. Callaghan, G. Petekidis, and D. Vlassopoulos, "Time-dependent rheology of colloidal star glasses," *J. Rheol.* **54**, 133 (2010).

[159] A. Chremos, E. Glynos, and P. Green, "Structure and dynamical intra-molecular heterogeneity of star polymer melts above glass transition temperature," *J. Chem. Phys.* **142**, 044901 (2015).

[160] D. Gottwald, C. Likos, G. Kahl, and H. Löwen, "Ionic microgels as model systems for colloids with an ultrasoft electrosteric repulsion: Structure and thermodynamics," *J. Chem. Phys.* **122**, 074903 (2005).

[161] E. Bartsch, M. Antonietti, W. Schupp, and H. Sillescu, "Dynamic light scattering study of concentrated microgel solutions as mesoscopic model of the glass transition in quasiatomic fluids," *J. Chem. Phys.* **97**, 3950 (1992).

[162] M. Cloitre, R. Borrega, and L. Leibler, "Rheological aging and rejuvenation in microgel pastes," *Phys. Rev. Lett.* **85**, 4819 (2000).

[163] T. Eckert and E. Bartsch, "The effect of free polymer on the interactions and the glass transition dynamics of microgel colloids," *Faraday Discuss.* **123**, 51 (2003).

[164] M. Cloitre, R. Borrega, F. Monti, and L. Leibler, "Structure and flow of polyelectrolyte microgels: from suspensions to glasses," *C. R. Phys.* **4**, 221 (2003).

[165] E. Purnomo, D. van den Ende, S. Vanapalli, and F. Mugele, "Glass transition and aging in dense suspensions of thermosensitive microgel particles," *Phys. Rev. Lett.* **101**, 238301 (2008).

[166] V. Carrier and G. Petekidis, "Nonlinear rheology of colloidal glasses of soft thermosensitive microgel particles," *J. Rheol.* **53**, 245 (2009).

[167] J. Mattsson, H. Wyss, A. Fernández-Nieves, K. Miyazaki, Z. Hu, D. Reichman, and D. Weitz, "Soft colloids make strong glasses," *Nature* **462**, 83 (2009).

[168] J.-J. Liétor-Santos, B. Sierra-Martín, and A. Fernández-Nieves, "Bulk and shear moduli of compressed microgel suspensions," *Phys. Rev. E* **84**, 060402 (2011).

[169] P. Menut, S. Seiffert, J. Sprakel, and D. Weitz, "Does size matter? Elasticity of compressed suspensions of colloidal- and granular-scale microgels," *Soft Matter* **8**, 156 (2012).

[170] P. Debenedetti and F. Stillinger, "Supercooled liquids and the glass transition," *Nature* **410**, 259 (2001).

[171] E. Weeks and D. Weitz, "Subdiffusion and the cage effect studied near the colloidal glass transition," *Chem. Phys.* **284**, 361 (2002).

[172] J.-P. Hansen and L. Verlet, "Phase transitions of the Lennard-Jones system," *Phys. Rev.* **184**, 151 (1969).

[173] E. Lange, J. Caballero, A. Puertas, and M. Fuchs, "Comparison of structure and transport properties of concentrated hard and soft sphere fluids," *J. Chem. Phys.* **130**, 174903 (2009).

[174] A. S. J. Iyer and L. Lyon, "Self-healing colloidal crystals," *Angew. Chem. Int. Edit.* **48**, 4562 (2009).

[175] J.-J. Liétor-Santos, *From soft to hard sphere behavior: The role of single particle elasticity over the phase behavior of microgel suspensions*, PhD thesis Georgia Institute of Technology 2010.

[176] C. Marques, D. Izzo, T. Charitat, and E. Mendes, "Scattering from solutions of star polymers," *Eur. Phys. J. B* **3**, 353 (1998).

[177] C. Likos, H. Löwen, M. Watzlawek, B. Abbas, O. Jucknischke, J. Allgaier, and D. Richter, "Star polymers viewed as ultrasoft colloidal particles," *Phys. Rev. Lett.* **80**, 4450 (1998).

[178] M. Watzlawek, H. Löwen, and C. Likos, "The anomalous structure factor of dense star polymer solutions," *J. Phys.: Condens. Matter* **10**, 8189 (1998).

[179] C. Likos, N. Hoffmann, H. Löwen, and A. Louis, "Exotic fluids and crystals of soft polymeric colloids," *J. Phys.: Condens. Matter* **14**, 7681 (2002).

[180] N. Hoffmann, C. Likos, and H. Löwen, "Structure and phase behavior of polyelectrolyte star solutions," *J. Chem. Phys.* **121**, 7009 (2004).

[181] P. Pusey, "Intensity fluctuation spectroscopy of charged Brownian particles: the coherent scattering function," *J. Phys. A: Math. Gen.* **11**, 119 (1978).

[182] R. Böhmer, K. Ngai, C. Angell, and D. Plazek, "Nonexponential relaxations in strong and fragile glass formers," *J. Chem. Phys.* **99**, 4201 (1993).

[183] J. Phillips, "Stretched exponential relaxation in molecular and electronic glasses," *Rep. Prog. Phys.* **59**, 1133 (1996).

[184] X. Xia and P. Wolynes, "Microscopic theory of heterogeneity and nonexponential relaxations in supercooled liquids," *Phys. Rev. Lett.* **86**, 5526 (2001).

[185] M. Potuzak, R. Welch, and J. Mauro, "Topological origin of stretched exponential relaxation in glass," *J. Chem. Phys.* **135**, 214502 (2011).

[186] K. van der Vaart, Y. Rahmani, R. Zargar, Z. Hu, D. Bonn, and P. Schall, "Rheology of concentrated soft and hard-sphere suspensions," *J. Rheol.* **57**, 1195 (2013).

[187] C. W. Macosko, *Rheology: Principles, Measurements, and Applications* (Wiley-VCH, New York, 1994).

[188] K. Hyun, S. Kim, K. Ahn, and S. Lee, "Large amplitude oscillatory shear as a way to classify the complex fluids," *J. Non-Newtonian Fluid Mech.* **107**, 51 (2002).

[189] C. Daniel, I. Hamley, M. Wilhelm, and W. Mingvanish, "Non-linear rheology of a face-centred cubic phase in a diblock copolymer gel," *Rheol. Acta* **40**, 39 (2001).

[190] C. Robertson and X. Wang, "Isoenergetic jamming transition in particle-filled systems," *Phys. Rev. Lett.* **95**, 075703 (2005).

[191] A. Liu, S. Ramaswamy, T. Mason, H. Gang, and D. Weitz, "Anomalous viscous loss in emulsions," *Phys. Rev. Lett.* **76**, 3017 (1996).

[192] W. Herschel and R. Bulkley, "Konsistenzmessungen von Gummi-Benzollösungen," *Kolloid Zeitschrift* **39**, 291 (1926).

[193] S. Meeker, R. Bonnecaze, and M. Cloitre, "Slip and flow in soft particle pastes," *Phys. Rev. Lett.* **92**, 198302 (2004).

[194] F. Krzakala and J. Kurchan, "Landscape analysis of constraint satisfaction problems," *Phys. Rev. E* **76**, 021122 (2007).

[195] G. Parisi and F. Zamponi, "Mean-field theory of hard sphere glasses and jamming," *Rev. Mod. Phys.* **82**, 789 (2010).

[196] H. Jacquin, B. Ludovic, and F. Zamponi, "Microscopic mean-field theory of the jamming transition," *Phys. Rev. Lett.* **106**, 135802 (2011).

[197] D. Vlassopoulos and M. Cloitre, "Tunable rheology of dense soft deformable colloids," *Curr. Opin. Colloid. In.* **19**, 561 (2014).

[198] A. Basu, Y. Xu, T. Still, P. Arratia, Z. Zhang, K. Nordstrom, J. Rieser, J. Gollub, D. Durian, and A. Yodh, "Rheology of soft colloids across the onset of rigidity: scaling behavior, thermal, and non-thermal responses," *Soft Matter* **10**, 3027 (2014).

[199] C. Coulais, R. Behringer, and O. Dauchot, "How the ideal jamming point illuminates the world of granular media," *Soft Matter* **10**, 1519 (2014).

[200] B. Sun, Z. Sun, W. Ouyang, and S. Xu, "Structural ordering and glass forming of soft spherical particles with harmonic repulsions," *J. Chem. Phys.* **140**, 134904 (2014).

[201] K. Desmond and E. Weeks, "Influence of particle size distribution on random close packing of spheres," *Phys. Rev. E* **90**, 022204 (2014).

[202] P. Yunker, K. Chen, M. Gratale, M. Lohr, T. Still, and A. Yodh, "Physics in ordered and disordered colloidal matter composed of poly(N-isopropylacrylamide) microgel particles," *Rep. Prog. Phys.* **77**, 056601 (2014).

[203] E. DeGiuli, E. Lerner, and M. Wyart, "Theory of the jamming transition at finite temperature," *J. Chem. Phys.* **142**, 164503 (2015).

[204] A. Ikeda and L. Berthier, "Thermal fluctuations, mechanical response, and hyperuniformity in jammed solids," *Phys. Rev. E* **92**, 012309 (2015).

[205] S. Alexander, "Amorphous solids: their structure, lattice dynamics, and elasticity," *Phys. Rep.* **296**, 65 (1998).

[206] C. Moukarzel, "Isostatic phase transition and instability in stiff granular materials," *Phys. Rev. Lett.* **81**, 1634 (1998).

[207] A. Tkachenko and T. Witten, "Stress propagation through frictionless granular material," *Phys. Rev. E* **60**, 687 (1999).

[208] M. Fuchs and M. Ballauff, "Flow curves of dense colloidal suspensions: Schematic model analysis of the shear-dependent viscosity near the colloidal glass transition," *J. Chem. Phys.* **122**, 094707 (2005).

[209] V. Kobelev and K. Schweizer, "Strain softening, yielding, and shear thinning in glassy colloidal suspensions," *Phys. Rev. E* **71**, 021401 (2005).

[210] D. Hajnal and M. Fuchs, "Flow curves of colloidal dispersions close to the glass transition," *Eur. Phys. J. E* **28**, 125 (2009).

[211] P. O'Connell and G. McKenna, "Arrhenius-type temperature dependence of the segmental relaxation below T_g," *J. Chem. Phys.* **110**, 11054 (1999).

[212] S. Simon, J. Sobieski, and D. Plazek, "Volume and enthalpy recovery of polystyrene," *Polymer* **42**, 2555 (2001).

[213] C. Thurau and M. Ediger, "Change in the temperature dependence of segmental dynamics in deeply supercooled polycarbonate," *J. Chem. Phys.* **118**, 1996 (2003).

[214] D. Cangialosi, M. Wübbenhorst, H. Schut, A. van Veen, and S. Picken, "Dynamics of polycarbonate far below the transition temperature: A positron annihilation lifetime study," *Phys. Rev. B* **69**, 134206 (2004).

[215] V. Boucher, D. Cangialosi, A. Alegría, and J. Colmenero, "Enthalpy recovery of glassy polymers: dramatic deviations from the extrapolated liquidlike behavior," *Macromolecules* **44**, 8333 (2011).

[216] D. Cangialosi, V. Boucher, A. Alegría, and J. Colmenero, "Direct evidence of two equilibration mechanisms in glassy polymers," *Phys. Rev. Lett.* **111**, 095701 (2013).

[217] H. Wagner and R. Richert, "Dielectric relaxation of the electric field in poly(vinyl acetate): a time domain study in the range $10^{-3} - 10^{6}$s," *Polymer* **38**, 255 (1997).

[218] J. Zhao and G. McKenna, "Temperature divergence of the dynamics of a poly(vinyl acetate) glass: Dielectric vs. mechanical behaviors," *J. Chem. Phys.* **136**, 154901 (2012).

[219] R. Richert, "Comment on "Temperature divergence of the dynamics of a poly(vinyl acetate) glass: Dielectric vs. mechanical behaviors" [J. Chem. Phys. 136, 154901 (2012)]," *J. Chem. Phys.* **139**, 137101 (2013).

[220] T. Hecksher, A. Nielsen, O. N.B., and J. Dyre, "Little evidence for dynamic divergences in ultraviscous molecular liquids," *Nat. Phys.* **4**, 737 (2008).

[221] G. McKenna and J. Zhao, "Accumulating evidence for non-diverging time-scales in glass-forming fluids," *J. Non-Cryst. Solids* **407**, 3 (2015).

[222] P. Segrè, S. Meeker, P. Pusey, and W. Poon, "Viscosity and structural relaxation in suspensions of hard-sphere colloids," *Phys. Rev. Lett.* **75**, 958 (1995).

[223] C. Pellet and M. Cloitre, "The glass and jamming transitions of soft polyelectrolyte microgel suspensions," *Soft Matter* **12**, 3710 (2016).

[224] P. Pusey and W. van Megen, "Dynamic light scattering by non-ergodic media," *Physica A* **157**, 705 (1989).

[225] B. Sierra-Martín, J. Frederick, Y. Laporte, G. Markou, J.-J. Liétor-Santos, and A. Fernández-Nieves, "Determination of the bulk modulus of microgel particles," *Colloid. Polym. Sci.* **289**, 721 (2011).

[226] C. Haro-Pérez, G. Ojeda-Mendoza, and L. Rojas-Ochoa, "Three dimensional cross-correlation dynamic light scattering by non-ergodic turbid media," *J. Chem. Phys.* **134**, 244902 (2011).

VITA

John Shelton Hyatt was born July 23rd, 1986 in Baton Rouge, Louisiana. He attended primary and secondary school in Houston, Texas, and in 2008 graduated *cum laude* from Knox College in Galesburg, Illinois, receiving dual Bachelor degrees in Biochemistry and Physics. He moved to Atlanta to attend Georgia Tech's Physics doctoral program the same year.